

University of Louisville

## ThinkIR: The University of Louisville's Institutional Repository

---

Electronic Theses and Dissertations

---

5-2018

### Ultrasonic nondestructive evaluation of metal additive manufacturing.

Venkata Karthik Nadimpalli  
*University of Louisville*

Follow this and additional works at: <https://ir.library.louisville.edu/etd>



Part of the [Acoustics, Dynamics, and Controls Commons](#), [Industrial Engineering Commons](#), [Manufacturing Commons](#), [Mechanics of Materials Commons](#), [Metallurgy Commons](#), and the [Structures and Materials Commons](#)

---

#### Recommended Citation

Nadimpalli, Venkata Karthik, "Ultrasonic nondestructive evaluation of metal additive manufacturing." (2018). *Electronic Theses and Dissertations*. Paper 2901.  
<https://doi.org/10.18297/etd/2901>

This Doctoral Dissertation is brought to you for free and open access by ThinkIR: The University of Louisville's Institutional Repository. It has been accepted for inclusion in Electronic Theses and Dissertations by an authorized administrator of ThinkIR: The University of Louisville's Institutional Repository. This title appears here courtesy of the author, who has retained all other copyrights. For more information, please contact [thinkir@louisville.edu](mailto:thinkir@louisville.edu).

ULTRASONIC NONDESTRUCTIVE EVALUATION OF METAL ADDITIVE  
MANUFACTURING

By

Venkata Karthik Nadimpalli

A Dissertation  
Submitted to the Faculty of the  
J. B. Speed School of Engineering of the University of Louisville  
in Partial Fulfillment of the Requirements  
for the Degree of

Doctor of Philosophy  
in Industrial Engineering

Department of Industrial Engineering  
University of Louisville  
Louisville, Kentucky

May 2018

Copyright 2018 by Venkata Karthik Nadimpalli

All rights reserved



ULTRASONIC NONDESTRUCTIVE EVALUATION OF METAL ADDITIVE  
MANUFACTURING

By

Venkata Karthik Nadimpalli

A Dissertation Approved on

April 30, 2018

by the following Dissertation Committee:

---

Dissertation Director: Dr. Li Yang

---

Dissertation Co-Director: Dr. Peter B. Nagy

---

Dr. Thomas L. Starr

---

Dr. Kevin Chou

---

Dr. Gail W. Depuy

*To My Parents*

## ACKNOWLEDGMENTS

I am grateful to my advisor Dr. Peter Nagy, for his generous guidance and support during my studies and research. He instilled in me a meticulous work ethic and his love for scientific inquiry. I express gratitude to my advisor Dr. Li Yang, for his support. I am thankful to my previous advisor Dr. Brent Stucker, for providing me with the guidance that propelled me through my PhD. I am grateful to my teacher, Dr. Durga Janakiram for inspiring me to pursue research. I would like to thank my committee members, Dr. Thomas Starr, Dr. Kevin Chou, and Dr. Gail Depuy, for their valuable inputs. I express sincere thanks to Mark Norfolk, Curtis Fox, Tim Gornet, Gary Graff, and Joseph Vickers, whose assistance and encouragement were a valuable resource. I would also like to thank Dr. Khalid Rafi, Dr. John Jangam, Dr. Jeong Na, Dr. Haijun Gong and Dr. Manogna Karthik.

I want to thank my grandparents for their blessings and my parents (Dr. Vijaya Lakshmi & Dr. Siva Kumar) for their encouragement, and inspiration. I am lucky to have the patience, love and understanding of my wife, Rupali. I express gratitude to all family members who supported me, especially my brother (Pranav), parents-in-law (Mrs. Kanta & Dr. Mohan), cousins (Deepti, Revathi), aunts & uncles (Mrs. Lakshmi, Mrs. Santha & Mr. Srinivas, Dr. Muralikrishna). I thank Rohit, Srikanth, Dilip, Sathya, Prajwal, Agrima, Anand, Ravi, Srishty, Amrit, Neel and Arun for their friendship and all memorable times.

I acknowledge the Office of Naval Research for funding my research through awards N00014-09-1-0147, N00014-10-1-0800 and N00014-004-1110689.

Venkata Karthik Nadimpalli

## ABSTRACT

# ULTRASONIC NONDESTRUCTIVE EVALUATION OF METAL ADDITIVE MANUFACTURING

Venkata Karthik Nadimpalli

April 30, 2018

Metal Additive Manufacturing (AM) is increasingly being used to make functional components. One of the barriers for AM components to become mainstream is the difficulty to certify them. AM components can have widely different properties based on process parameters. Improving an AM processes requires an understanding of process-structure-property correlations, which can be gathered in-situ and post-process through nondestructive and destructive methods. In this study, two metal AM processes were studied, the first is Ultrasonic Additive Manufacturing (UAM) and the second is Laser Powder Bed Fusion (L-PBF).

The typical problems with UAM components are inter-layer and inter-track defects. To improve the UAM process, an in-situ quality evaluation technique was desired. Several NDE techniques were tested in a lab environment before ultrasonic NDE was chosen as a practical, robust, and cost-effective NDE tool. An in-situ monitoring setup was designed and built on an UAM system. NDE results showed interesting features that were simulated through analytic and finite element wave-propagation models. AM layers with defects were characterized as an intact layer and a finite interfacial stiffness spring. The spring stiffness



coefficient is a quality parameter that was used to characterize AM layers through a model-based inversion method. In-situ and post-process NDE provided an understanding of defect generation and propagation in UAM. A novel solid-state repair mechanism based on Friction Stir Processing (FSP) was proposed and demonstrated.

The quality of L-PBF components depends on several factors including laser power, scan speed, hatch spacing, layer thickness, particle shape/size distribution and other build conditions. Developing process parameters for a new material is an expensive and complex optimization problem. Post-process ultrasonic NDE tests revealed that the model-based in-situ quality monitoring developed for UAM is also applicable to L-PBF Additive Manufacturing. A similar NDE set-up was designed and installed on an open-architecture L-PBF system. A layer-by-layer bond quality evaluation demonstrates the ability to detect good-quality bonds hidden behind poor-quality regions for Inconel 625 alloy. A cost-effective, process parameter development methodology has been proposed and demonstrated.

## TABLE OF CONTENTS

ACKNOWLEDGEMENTS .....	iv
ABSTRACT .....	v
LIST OF TABLES .....	ix
LIST OF FIGURES .....	x
CHAPTER 1 .....	1
INTRODUCTION AND LITERATURE REVIEW.....	1
1.1 Research Motivation and Problem Statement .....	1
1.2 Ultrasonic Additive Manufacturing.....	3
1.3 Selecting a Suitable NDE Method for UAM.....	11
1.4 Laser Powder Bed Fusion Additive Manufacturing.....	39
1.5 Objectives and Dissertation Format .....	46
CHAPTER 2 .....	48
DESIGNING AN IN-SITU ULTRASONIC NONDESTRUCTIVE EVALUATION SYSTEM FOR ULTRASONIC ADDITIVE MANUFACTURING .....	48
2.1 Introduction .....	48
2.2 Offline NDE of UAM Components.....	50
2.3 In-situ NDE Setup .....	53
2.4 Conclusions and Future Work .....	61
CHAPTER 3 .....	63
IN-SITU INTERFACIAL QUALITY ASSESSMENT OF ULTRASONIC ADDITIVE MANUFACTURING COMPONENTS USING ULTRASONIC NONDESTRUCTIVE EVALUATION .....	63
3.1 Introduction .....	63
3.2 Experiment.....	68
3.3 Finite Interfacial Stiffness Model.....	76

3.4	Inversion Model.....	88
3.5	Conclusion.....	100
CHAPTER 4	.....	103
MONITORING AND REPAIR OF DEFECTS IN ULTRASONIC ADDITIVE MANUFACTURING .....		103
4.1	Introduction .....	103
4.2	Monitoring Evolution of Defects in UAM .....	106
4.3	Repairing UAM Defects through Friction Stir Processing.....	122
4.4	Conclusion.....	131
CHAPTER 5	.....	134
ULTRASONIC NONDESTRUCTIVE EVALUATION AS A PROCESS PARAMETER DEVELOPMENT TOOL FOR LASER POWDER BED FUSION ADDITIVE MANUFACTURING.....		134
5.1	Introduction .....	134
5.2	Design of Experiment.....	143
5.3	In-situ Bond Quality Evolution .....	146
5.4	Conclusion.....	152
CHAPTER 6	.....	154
CONCLUSIONS AND FUTURE WORK .....		154
6.1	Conclusions .....	154
6.2	Future Work.....	159
REFERENCE	.....	161
APPENDIX- PERMISSIONS	.....	172
CURRICULUM VITA	.....	181

## LIST OF TABLES

	PAGE
Table 1.1 Experimentally measured ultrasonic velocity and elastic stiffness coefficient.	15
Table 1.2 Averaging via flipping of the linear-mode signals [61].....	20
Table 1.3 Build parameters used to manufacture Ti-6Al-4V components, Gong <i>et al.</i> [71]. Process constants are hatch spacing of 0.1 mm, layer thickness of 0.03 mm.....	43
Table 2.1 Area under load-displacement curves in kN-mm from push-pin tests .....	60
Table 4.1 FSP process parameters .....	123

## LIST OF FIGURES

	PAGE
Figure 1.1 (a) Schematic of Ultrasonic Additive Manufacturing process [1], (b) Fabrisonics R200 research machine .....	3
Figure 1.2 (a) Embedded optical fibers, (b) Al-Cu-Al laminate [2] .....	4
Figure 1.3 (a) EBSD maps seen from the rolling direction around the 30th, 16th and 2nd layers, (b) The definition of the regions divided by their microstructure [17] .....	6
Figure 1.4 Illustration of welding mechanism (a) Initial state, (b) Normal force and surface contact, (c, d) Deformation and breaking up of oxide layers, (e) Metal to metal contact with plastic flow leading to metallurgical bonding, (f) Dynamic recovery and recrystallization [17].....	7
Figure 1.5 Gross defects in the UAM process, (a) Type-1 defects or delaminations, (b) Type-2 defects between adjacent tracks [1].....	8
Figure 1.6 A schematic of acoustic microscopy measurements. The base/build image is derived by gating the interface signal while the stack image represents the transmitted signal reflected from the top of the UAM structure.....	16
Figure 1.7 Ultrasonic signatures of components built using different vibration amplitudes with acoustic microscopy C-scans of the two gated signals at the bottom.....	16

Figure 1.8 (a) EMAT operation, (b) Lorentz Force and Magnetostriction, (c) Longitudinal and Angle beam EMATs, (d) Shear radial and Shear horizontal EMATs [51,52].....	18
Figure 1.9 Shear velocity variation with build amplitude in UAM components.....	19
Figure 1.10 The two mixing signals with frequencies 2.8 MHz each .....	21
Figure 1.11 Nonlinear signal from a bad region of a UAM component.....	21
Figure 1.12 Nonlinear signal measured on four different samples at approximately one location close to the center of each sample.....	22
Figure 1.13 (a) Transmission image, (b) Reflection (base/build interface) image. The nonlinear signal is highest at the cross marks.....	23
Figure 1.14 (a) A single element ultrasonic transducer generating a traveling wave, and (b) the same transducer receiving the waves scattered from a spherical reflector [54].....	24
Figure 1.15 (a) An ultrasonic phased array, where the driving electrical pulses for each element arrive in unison, (b) An ultrasonic phased array where a set of delays are used to steer the sound beam of the array and, (c) The case where a set of delays produce a focusing of the sound beam [54] .....	26
Figure 1.16 (a) Aluminum-copper composite manufactured by UAM (b) Phased array imaging using beam forming to focus at various depths inside the UAM sample .....	27
Figure 1.17 In-situ signal using the dual element delay line transducer after 80 layers...	29
Figure 1.18 Average signal power during continuous monitoring during the UAM build .....	31

Figure 1.19 Average signal power variation due to force modulation during a UAM build .....	31
Figure 1.20 Schematic diagram of a Potential Drop measurement [67].....	34
Figure 1.21 Current distribution in sound and cracked specimens using (a) DCPD and (b) ACPD [65] .....	34
Figure 1.22 Block diagram of an ACPD experiment [66] .....	35
Figure 1.23 ACPD resistance across a factorial design of UAM builds.....	37
Figure 1.24 Average ACPD resistance variation from build start to build Finish across a factorial design of UAM samples .....	37
Figure 1.25 Schematic of L-PBF process (From EOS GMBH) .....	40
Figure 1.26 Modulus of AM components calculated by NDE in comparison to, a) The Archimedes' porosity (RD), b) the Young's modulus obtained from tensile tests.....	45
Figure 2.1 a) Schematic of the Ultrasonic Additive Manufacturing process [95] .....	50
Figure 2.2 . a) A-scan captured at the center of the UAM stack. b) Acoustic microscopy C-scans gated at the base/build interface and top of the UAM stack .....	51
Figure 2.3 Reflection and transmission images captured on UAM components of varying build quality .....	53
Figure 2.4 a) In-situ monitoring from above. b) In-situ monitoring from below .....	55
Figure 2.5 Schematic of experiment to test the effect of in-situ NDE monitoring system	56
Figure 2.6 C-scan images of components built with various setup configurations .....	57

Figure 2.7 Push-pin test results for four configurations: a) reference, b) vibration direction (Y- supports), c) bonding direction (X- supports), and d) fully enclosed.....	59
Figure 2.8 a) A-scans collected after bonding number of layers .....	61
Figure 3.1 In-situ monitoring of the UAM process with access from below .....	69
Figure 3.2 Average group velocity measured after bonding each layer .....	71
Figure 3.3 a) Variation of ultrasonic group velocity with build amplitude after 45 layers, b) mechanical work performed on pushing out 15 UAM layers and its variation with build amplitude.....	72
Figure 3.4 a) Average layer thickness, b) ultrasonic group velocity with varying UAM vibration amplitudes.....	73
Figure 3.5 Variation of ultrasonic parameters with UAM vibration amplitude: a) frequency amplitude spectrum, b) attenuation coefficient, and c) phase velocity.....	75
Figure 3.6 a) Schematic of layered UAM structure with interfacial springs, b) the longitudinal elastic modulus of a homogeneous structure with imperfect interfacial springs with coefficient $\eta$ (the IT model represents $N = 50$ layers) .....	77
Figure 3.7 COMSOL FE model of a UAM component for modeling of ultrasonic NDE	82
Figure 3.8 Simulated velocities for various $\eta_1, \eta$ values .....	83
Figure 3.9 Symmetric unit cell for Floquet wave homogenization .....	86
Figure 3.10 Comparison between FE model and Floquet wave homogenization model for a constant stack thickness and variable layer thickness at $\eta = 10$ . (a) presented in the same	



time scale (b), (c) and (d) signals shifted to compare dispersion with respect to the transmitted signal ..... 88

Figure 3.11 Schematic of inversion model to calculate  $\eta_1, \eta$  ..... 93

Figure 3.12 Sensitivity of the inversion model. The 5% line indicates a level of sensitivity parameter ( $S$ ) which gives greater than 95% confidence on the inversion. For  $S$  above the dotted line, the inversion methodology can be considered sensitive and robust ..... 95

Figure 3.13 Inversion of  $\eta, \eta_1$  after bonding 80 layers (a) real part, (b) imaginary part.. 97

Figure 3.14 Floquet wave velocity calculated from inversion as compared to experimentally measured phase velocities. Markers represent Floquet velocities and solid lines represent experimental velocities ..... 98

Figure 3.15 In-situ layer-by-layer inversion of bond quality..... 99

Figure 4.1 In-situ monitoring ultrasonic NDE setup with fully embedded sensor a) front view, b) side view ..... 107

Figure 4.2 In-situ monitoring after bonding each UAM layer for two components of varying quality. The reverberation from the oil buffer was cut out from the signals, so that the features of interest can be better represented ..... 109

Figure 4.3 Schematic of UAM interfaces as finite stiffness springs [117]..... 110

Figure 4.4 Interfacial stiffness values of components with varying quality a) base/build interface, b) average of UAM stack ..... 111

Figure 4.5 Acoustic microscopy gated to generate images at the base build interface (reflection image) and the UAM stack (transmission image)..... 113

Figure 4.6 Acoustic microscopy of UAM components at a) base/build interface (reflection image) and b) The top of UAM stack (transmission image). In the reflection image, black indicates a good bond while in the transmission image white indicates a good bond.... 114

Figure 4.7 (a) Low-magnification optical micrograph of a 11.5 mm height UAM sample. (b) Schematic of a compliant UAM stack. In the first 7.5 mm from the bottom, the sample showed good layer bonding (c). In the top 4 mm, several Type-1b defects (marked by arrows) were seen at the layer interfaces (d) ..... 117

Figure 4.8 a) Change in average weld power with layer height for varying vibration amplitudes b) Normalized power..... 118

Figure 4.9 Change in UAM stack modulus with layer height and vibration amplitude calculated by a model-based inversion of in-situ monitoring NDE signals..... 120

Figure 4.10 Push-pin test results for various vibration amplitudes ..... 121

Figure 4.11 Schematic of FSP tool and a typical FSPed sample (top view). Arrows show the directions of tool rotation and travel. AS and RS denote the advancing and retreating sides of the processed region ..... 123

Figure 4.12 (a) Optical micrograph of a UAM build. Encircled region marks a crack at the base/build interface. The crack is shown at a higher magnification in (b) ..... 124

Figure 4.13 Schematic illustration of the use of FSP for healing base/build interface delamination (Type-1a defects) ..... 125

Figure 4.14 Optical micrographs a UAM sample FSPed for repair of a base/build interface (Type-1a) defect. The crack is completely healed by FSP ..... 126

Figure 4.15 Acoustic microscopy images: (a) as-built, (b) after FSP. The color scale of the two images is different with a higher value representing a larger reflection and thus a delamination.....	127
Figure 4.16 Inter-track defects typically found in UAM components.....	128
Figure 4.17 Schematic illustration of the use of FSP for repair of Type-2 defects in UAM parts.....	129
Figure 4.18 Optical micrographs of a UAM sample FSPed for repair of a Type-2 defect. The defect is completely healed by FSP.....	130
Figure 5.1 a) AM interfaces are modeled as spring stiffnesses b) Change in modulus with interfacial stiffness coefficient ( $\eta$ ) which is a dimensionless quality parameter .....	137
Figure 5.2 a) In-situ monitoring of IN-718 with varying laser power taken from Reider <i>et al.</i> [90, 91], b) Simulation of ultrasonic wave propagation through AM component shows the experimentally observed signal features.....	139
Figure 5.3 a) Simulation of ultrasonic wave propagation through an AM structure, b) Comparison of phase velocity calculated from simulation on left and from experiment on the right published in Reider <i>et al.</i> [91].....	141
Figure 5.4 a) Ultrasonic response of an IN 625 AM component (5 mm) attached to an IN 625 base (10 mm). b) Acoustic microscopy of a coupon that has been removed from the base .....	144
Figure 5.5 Optical microscopy images from Dilip <i>et al.</i> [72] and corresponding acoustic microscopy images from a focused transducer. The coupons were approximately 5 mm x 5 mm x 5 mm cubes cut out for performing optical microscopy.....	145

Figure 5.6 Schematic of Inconel 625 L-PBF fusion component with varying quality on the right and an optical macrograph on the left. The red squares indicate regions used for microscopy..... 147

Figure 5.7 Optical micrographs of etched IN 625 L-PBF components at, a) base/build interface, b) within first 60 layers, c) between 60-70 layers, d) between 80-100 layers 148

Figure 5.8 In-situ ultrasonic NDE signals after building several layers of L-PBF component ..... 149

Figure 5.9 Change in average interfacial quality parameter ( $\eta_{avg}$ ) with layer build-up.. 150

Figure 5.10 Change in layer-by-layer interfacial quality parameter with layer build-up 150

# CHAPTER 1

## INTRODUCTION AND LITERATURE REVIEW

### 1.1 Research Motivation and Problem Statement

Over the past two decades, metals have been increasingly adopted by Additive Manufacturing (AM) which is a solid freeform fabrication technique. Layer-by-layer manufacturing was originally used as a rapid prototyping method. The improvement in foil and powder-based metal AM systems has led to the rapid rise of functional components. One of the barriers for metal AM components to become mainstream for structural applications is the difficulty in certifying them. A manufacturing process chain with AM typically involves, removing support structures, post-process heat treatment, hot isostatic pressing (HIPing) and machining to dimensional tolerance to eliminate typical defects and improve the microstructural characteristics. Defects in AM components are inherently geometry dependent and hence functional AM components need to be certified on a case-by-case basis. Reducing AM defects post-process is expensive and time consuming. Compared to traditional manufacturing methods, Additive Manufacturing provides a unique opportunity for in-process monitoring that can be used for certification layer-by-layer. In-situ and post-process Nondestructive Evaluation (NDE) are useful tools for developing process-structure-property correlations.

Ultrasonic Additive Manufacturing (UAM) is a solid-state joining manufacturing process that is commonly used in conjunction with a CNC mill to make functional metal

components. It involves the ultrasonic welding of thin foils on a base substrate. The defects in UAM are typically inter-layer and inter-track delaminations. It is important to understand the mechanism of generation of defects so that they can be mitigated. The quality of UAM components depends on several process parameters including normal force, vibration amplitude, speed of bonding along with geometrical and environmental factors.

Laser Powder Bed Fusion (L-PBF) is a prominent metal additive manufacturing technology for making functional components in various materials. The quality of L-PBF components depends on several factors including laser power, scan speed, hatch spacing, layer thickness, particle shape/size distribution and other build conditions. Developing process parameters for a new material is an expensive, time consuming and complex optimization problem which typically involves the manufacture of several coupons and test bars to characterize the relationships between the build conditions and L-PBF part quality.

In-situ nondestructive evaluation (NDE) techniques currently used in metal AM processes monitor the just bonded layer. NDE techniques which go through the entire AM component are not ideal to measure complex shapes but can provide valuable process-structure-property correlations that can help improve existing AM processes. Vibration-based linear and nonlinear ultrasonic NDE techniques were considered for this purpose. The ideal way to design a suitable NDE sensor setup is to test the response in a laboratory setting. Various NDE techniques that show potential can be shortlisted for further assessment of their suitability for online monitoring. To develop an in-situ NDE system for an industrial application, it is important to consider simplicity, robustness, and repeatability. Existing literature on in-situ monitoring of UAM and L-PBF systems was reviewed. Various NDE methods were then tested on UAM components.

## 1.2 Ultrasonic Additive Manufacturing

Ultrasonic Additive Manufacturing (UAM) is a layer-by-layer metal based solid-state manufacturing process which is commonly used in conjunction with a CNC mill and offers advantages in material properties as compared to traditional metal joining and forming technologies [1-3]. It uses normal force coupled with low frequency mechanical ultrasonic vibrations to create a solid-state weld between a thin foil and an existing substrate. Ultrasonic welding is an established industrial bonding process for plastics and soft metals. UAM is essentially layer-by-layer ultrasonic welding combined with CNC machining after each layer, hence providing freeform fabrication capability. Given the right bonding parameters, complete solid-state metallurgically bonded welds can be fabricated.

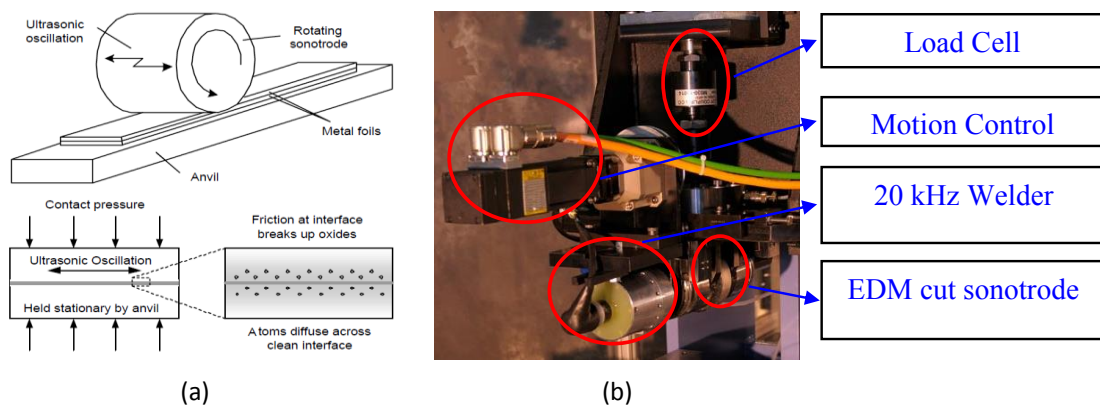


Figure 1.1 (a) Schematic of Ultrasonic Additive Manufacturing process [1],  
(b) Fabrisonics R200 research machine

For several years, the material systems that could easily be bonded using the UAM process were limited to softer Aluminum alloys (Al 3003) due to high power requirement for other engineering materials. The Fabrisonic UAM systems overcome this hurdle by using a high-power transducer and load cell which makes it feasible to build components from Copper, Nickel and Iron based alloy systems. Fig. 1.1a shows a schematic of the

UAM process and Fig. 1.1b shows a manual research machine (Fabrisonic R200). A constant force is applied while the ultrasonic horn vibrates laterally as it moves forward inducing plastic deformation within a sheet material causing it to bond onto a base substrate. The ultrasonic vibration breaks up the oxide layers on the top of the foil and exposes nascent metal-to-metal contact following which the deformation causes plastic flow and atomic diffusion leading to sub-micron size grain refinement and ultimately bond formation.

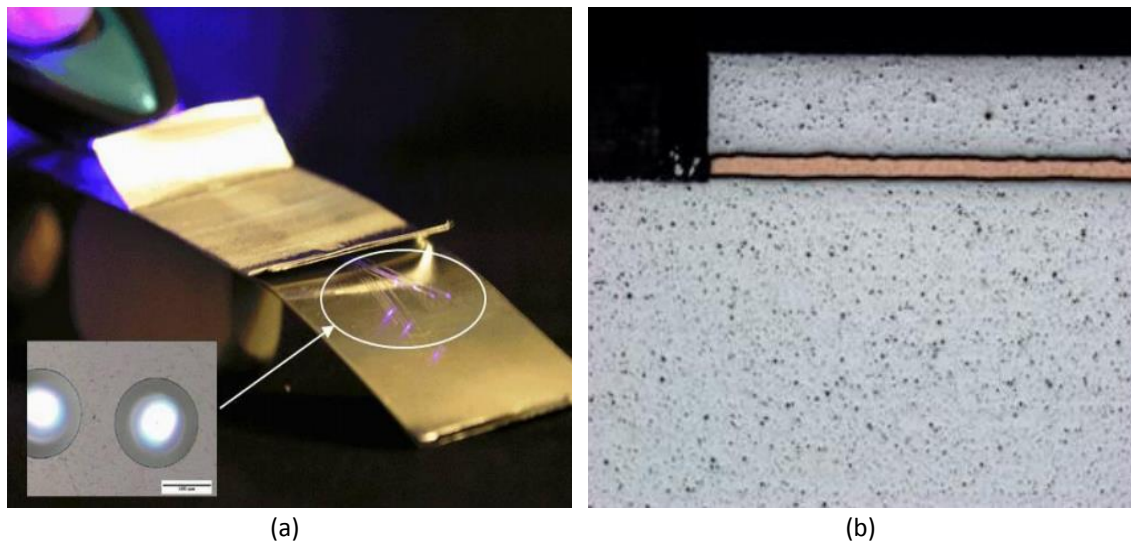


Figure 1.2 (a) Embedded optical fibers, (b) Al-Cu-Al laminate [2]

The additive / subtractive nature and the room temperature processing capability of the process gives rise to unique capabilities such as completely enclosed cooling channels, smart parts with embedded sensors (Fig. 1.2) and composite materials that cannot be produced traditionally. Alloy systems that cannot be easily fusion welded together can be joined making multi material components that do not suffer from common weld defects like embrittlement and solidification cracking.



The quality of each bond and thus the level of imperfection of each interface is critical towards estimating the quality of a UAM build. UAM components are anisotropic, by nature of being layered-structures with defects. The stiffness of each interface plays a major role in component strength. Most UAM components are meant to be used for functional applications under service loads and need to be certified as defect free before they can be used. Current online monitoring efforts all involve optical, laser based and temperature measurements which do not go through the entire component. In order to build good quality components, it is important to have online monitoring tools which can evaluate the structural quality of UAM layers.

UAM involves high speed relative motion between foils to be joined. Several researchers have studied the mechanism of bonding in ultrasonic metal welding [3-35]. The bonding process is a function of the input parameters, force applied, velocity of bonding vibration frequency and vibration amplitude. It is also dependent on surface roughness [21], temperature [21,22], base plate characteristics, part geometry and build height [11] among other factors. The bonding process can be separated into, (i) volumetric bonding and (ii) surface bonding effects. Volumetric bonding effects include elastic and plastic deformation enhanced through reduced yield stress due to acoustic and thermal softening. Surface bonding effects include interfacial friction and shearing which break up the oxide layers and bring more nascent metal to metal contact. Bond formation by ultrasonic welding requires two conditions to be fulfilled, (i) the generation of clean surfaces with no barrier layers at the atomic scale and (ii) a direct contact between these clean surfaces. Ram *et al.* [1] suggested that the surface-oxide layers are broken up by the vibrations and are displaced within the vicinity of the interface region. Electron Backscatter Diffraction (EBSD) studies

by Mariani and Ghassemieh [23] and Shimizu *et al.* [17] have shown that between any two foils the microstructure can be divided into upper bulk region, fine grained interface region and lower bulk region as shown in Fig. 1.3, It can be seen that the fine-grained interface region has a size less than 20  $\mu\text{m}$  and the microstructure of the bulk foil remains similar to that of rolled aluminum. Another difference is the interface microstructure which is equiaxed owing to the recrystallization during welding.

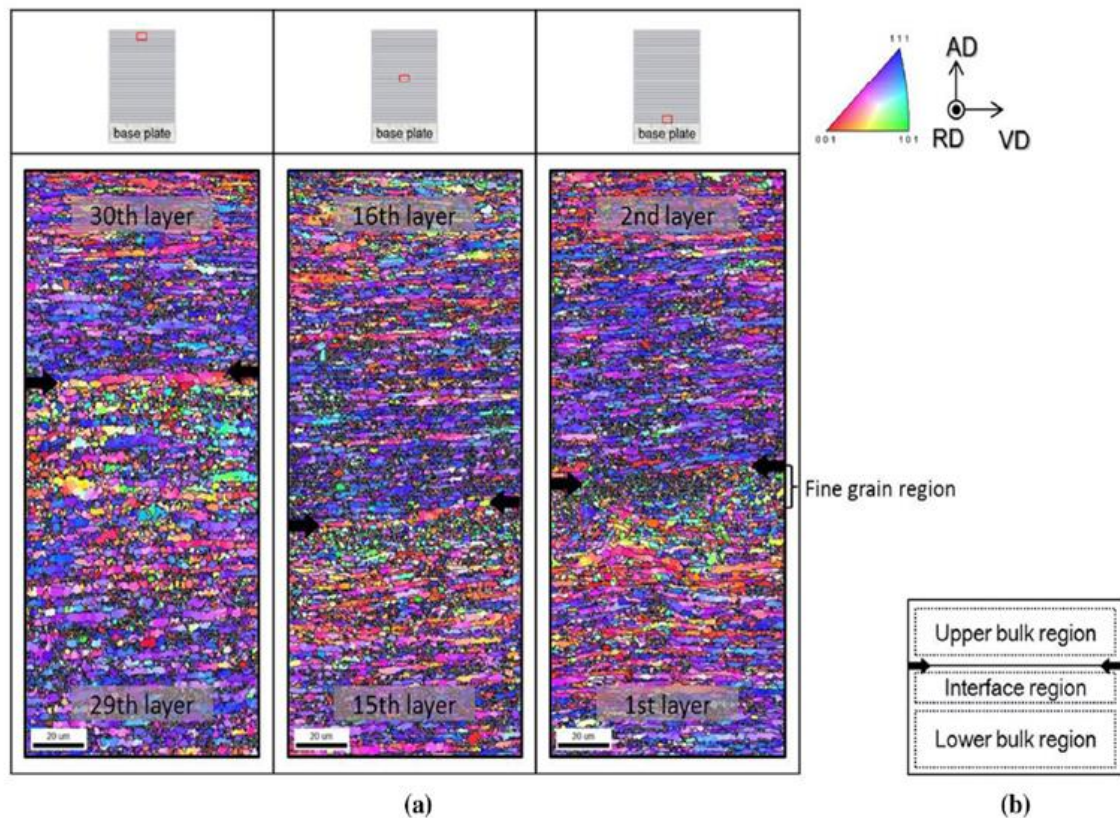


Figure 1.3 (a) EBSD maps seen from the rolling direction around the 30th, 16th and 2nd layers, (b) The definition of the regions divided by their microstructure [17]

TEM studies with an elemental EDX by Shimizu *et al.* [17] show that in many cases a sub-micron (around 0.1  $\mu\text{m}$ ) oxide layer can exist at the interface. Several modeling efforts [6, 13, 24, 25] have shown that the high strain rate deformation in UAM causes a localized rise in temperature up to 0.5  $T_m$  (melting temperature). Such a sharp rise in

temperature in a small interval of time due to adiabatic heating can decrease the flow stress of the material appreciably for further deformation. On the other hand, the flow stress can also increase with strain rate. The two competing processes are (i) temperature effect and (ii) strain effect. Eventually the effect of increased temperature prevails resulting in softening through dynamic recovery and recrystallization (DRX). Fig. 1.4 shows a schematic of the UAM bonding process.

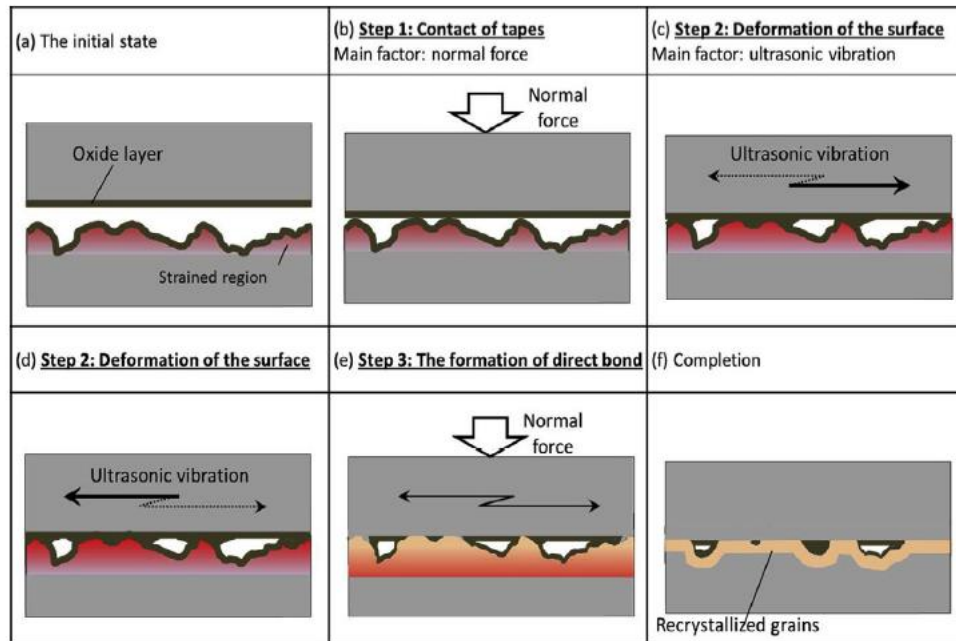


Figure 1.4 Illustration of welding mechanism (a) Initial state, (b) Normal force and surface contact, (c, d) Deformation and breaking up of oxide layers, (e) Metal to metal contact with plastic flow leading to metallurgical bonding, (f) Dynamic recovery and recrystallization [17]

The most common defects in UAM components are shown in Fig. 1.5. They are typically classified as Type-1 defects or delaminations between layers one on top of the other and Type-2 defects which form between adjacent tracks. Both Type-1 and Type-2 defects are harmful to the strength of components. Type-1 defects that can be seen via optical microscopy are gross delaminations and indicate process parameters which are far

from optimal that would not be used in a typical industrial setting. Process parameter optimization within UAM has always been performed experimentally by varying the input parameters until a satisfactory bond quality was achieved according to the metric of Linear Weld Density (% of area that appears to be fully bonded via optical microscopy). Some researchers [16] have found that %LWD is not a good measure of the bond strength since it does not take into account kissing bonds or tightly shut regions. A better qualitative mechanism was suggested [26] based on a pull out tensile test followed by measurement of the fractured surface to analyze the % Bonded region. It was argued [26] that there is a definite presence of tightly closed surfaces in UAM that cannot be observed with an optical microscope, hence only after tensile testing will these kissing bonds be visible.

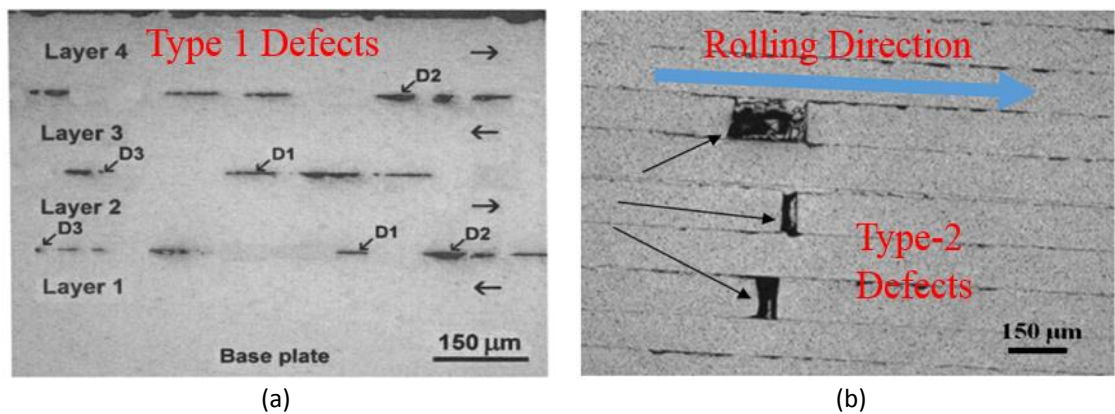


Figure 1.5 Gross defects in the UAM process, (a) Type-1 defects or delaminations, (b) Type-2 defects between adjacent tracks [1]

Bond strength measurement was first reported using the peel test after bonding new layers [18]. Other mechanical tests involved using lap shear, push pin and tensile tests [27]. It is of primary interest to be able to identify those imperfect interfaces which are often invisible even in a magnified optical microscope. But these imperfect interfaces lead to a gross reduction in mechanical properties and, without the right NDE techniques to characterize them, render UAM components to be unreliable for structural applications.

Existing in-situ monitoring literature is primarily based on temperature measurement. An IR camera was used [9] to observe the temperature of the just bonded foil during welding. The weld energy was calculated as a function of the rise in temperature and was correlated to the peel strength of the welds. Another method to monitor temperature is to embed a K-type thermocouple between two UAM layers and bond on top of the same [8]. This approach confirms that the internal temperature of the UAM builds goes only up to 250 °C in Al 6061. It also shows that the rise in temperature stronger materials is higher. The results prove that UAM is a truly solid-state bonding process and that the energy drawn towards heating is contributing to the plastic flow and hence is related to the mechanical strength [8].

A truly online monitoring approach has been demonstrated [28] with a photonic Doppler velocimeter measuring the phase and velocity of the sonotrode, foil and base. The results showed some promise in characterizing the contrast between a good weld and a poor one but monitors only the just bonded foil. Online in-situ monitoring of layer-by-layer manufacturing processes offers a unique advantage which is, to be able to make changes to the build parameters in real time to achieve closed loop process control. Most fusion based AM processes form defects in the top few layers from the solidification zone and hence monitoring the top surface is critical, leading to the use of optical techniques such as infrared imaging (IR). But in the case of UAM parts, the layer might be fully bonded initially but can form a delamination due to repeated cyclic loading several layers after it has been bonded. Hence, it is crucial to have an NDE sensor that goes through the entire component. Due to the lower temperatures in UAM, ultrasonic NDE is an attractive choice.

Interaction of ultrasound with an imperfect interface is a classical problem. It is well established that ultrasonic waves are sensitive to imperfect interfaces even if the imperfections are much smaller than the wavelength. The reflection of ultrasound from partially contacting and sliding surfaces, was studied by Kendall and Tabor (1971) [36] using a spring model. Haines and Langston (1980) [37] used a similar spring model to express the reflection and transmission coefficients of an ultrasonic wave as a function of the interfacial stiffness. Baik and Thompson (1984) [38] described how the interaction of ultrasonic waves with an imperfect interface could be modeled as a spring-mass system when the wavelength of ultrasound was large in comparison to the thickness of the interface.

The spring stiffness referred to as the interfacial stiffness is the ratio of stress by interface crack opening displacement at an imperfect interface. A finite interfacial stiffness indicates an imperfect interface with a frequency dependent response. Nagy and Adler (1988) [39] showed how imperfect interfaces in similar and dissimilar inertia and friction welds could be characterized by ultrasound. Nagy (1992) [40] also introduced a method to differentiate between different kinds of imperfect interfaces like slip bonds, kissing bonds and partial bonds. Several researchers have shown ultrasonic techniques to be effective in classifying adhesive bonds [41-43] and diffusion bonds [44-47]. UAM components consist of a layered structure with several imperfect interfaces and each interface is like a diffusion bonded/ friction welded interface. Hence, ultrasonic/acoustic methods are naturally the first choice as a potential NDE technique. In the following section various NDE methods are discussed which might be applicable to UAM components. Experiments are then conducted in a laboratory setting to evaluate the best in-situ monitoring NDE setup for industrial application.

### 1.3 Selecting a Suitable NDE Method for UAM

Several types of ultrasonic waves can be generated such as longitudinal, shear, surface, and Lamb waves. Out of these, surface and lamb waves are not practical to produce within the UAM setup. The simplest way to produce longitudinal waves is via contact transducers, while the best way to produce shear waves would be to use Electro Magnetic Acoustic Transducers (EMATs). Longitudinal normal incidence contact transducers are the norm in ultrasonic NDE, with robust piezo transducers that are commercially available. Shear normal incidence contact transducers are good for laboratory use but they require special couplants and are unreliable for industrial applications. Feedback through a piezoelectric transducer always involves waves travelling through a contact medium before reaching the receiver. Every time waves pass through the component they also encounter the contact medium twice. Metallographic preparation, flat surfaces and a thin coupling medium are often required for accurate velocity and attenuation measurements when using contact transducers. EMATs eliminate the need of a coupling medium owing to their noncontact ultrasonic generation mechanism

EMATs are devices made up of coils fed by a large dynamic current (a pulse or a tone-burst are commonly used) and a magnet or electromagnet providing a static magnetic field [48-52]. When the EMAT is close to a metallic sample, an eddy current of area density  $J_e$  is induced in it. The interaction of current density with the bias magnetic flux density  $B$  results in a net body force on the sample known as the Lorentz force. In ferromagnetic materials, in addition to the Lorentz force we also have magnetostrictive transduction mechanism. The efficiency of transduction through a material decreases quickly with stand-off distance thus limiting the non-contact distance to a few mm, which is sufficient

for making non-contact measurements. EMATs have good repeatability since there is no external couplant. Common modes for non-ferrous materials include shear waves that can be radially polarized, plane polarized, or are angular in nature [48], thus making EMATs an ideal candidate for studying in-situ the interaction of shear ultrasonic waves with UAM components.

Ultrasonic array probes consist of many individually wired ultrasonic elements within a single transducer package. The elements can be fired individually or in groups with different phase shifts which allows an array probe to steer and focus the ultrasonic beam [53-55]. In addition, phased array probes can produce images of the internal structure of a component, which enable components with complex geometries to be inspected with more accuracy, thus making phased array probes attractive to image the interfaces within an UAM build.

Conventional active acoustic methods rely on the principles of linear acoustics. These effects are reflection, scattering, transmission and absorption of probe acoustic energy at a certain bandwidth of frequency. The presence of a defect leads to a phase and/or amplitude variation of the received signals while the frequencies are the same as those of the emitted probe signals. The principle difference between linear and nonlinear acoustic NDE techniques is that, the nonlinear technique correlates the presence and characteristics of a defect (or the inherent material) with acoustical signals whose frequencies differ from the frequencies of the emitted probe signal. The signals with differing frequencies are an outcome of a nonlinear transformation of the probe acoustic energy. Several methods are historically used for Nonlinear NDE [56-61] for instance, (i) Modulation and (ii) Second harmonic generation. Second harmonic generation involves the presence of a transmitter



of frequency  $f$  and a receiver of frequency  $2f$ . Vibro-modulation involves the modulation of a high frequency acoustic signal with a low frequency component that separates itself from the primary frequency. There is an inherent modulation within the UAM process with a 20 kHz vibration which makes it attractive to consider the modulation of a higher frequency ultrasonic signal that is already generated using a longitudinal contact or a shear EMAT. Modulation techniques are sensitive to geometric nonlinearities that open and close upon the application of load. Due to the nature of the UAM process, Vibro-modulation is an interesting choice for a nonlinear acoustic NDE method.

Material and interface degradation is usually accompanied by a significant increase in ultrasonic nonlinearity, which can be substantially higher than the intrinsic nonlinearity of the intact material. Despite the advantage over conventional linear methods, nonlinear NDE methods have failed to find wider application in quantitative materials characterization because they are very difficult to adapt to field inspection. The main reason is that the sensitive nonlinear harmonics generation technique is also sensitive to spurious nonlinearities that inherently occur in the driving electronics and in the coupling medium between the transducers and the component to be inspected. These spurious nonlinearities could be comparable, or even stronger, than the sum of the intrinsic lattice nonlinearity and the excess nonlinearity caused by material imperfections. These problems can be very elegantly avoided by using ultrasonic wave mixing [62-64]. Wave mixing coupled with appropriate flipping and averaging of the signals can lead to suppression of the linear ultrasonic signals as well as the nonlinearities that arise from sources other than the imperfections that are of interest. Without changing the transducer and by investing in electronics it is possible to perform both a nonlinear as well as a linear measurement within

the online monitoring setup on a UAM platform. Hence it is worth exploring the possibility of using nonlinear NDE techniques.

All the techniques mentioned until now are acoustic and all of them expect to have access from below the base plate of the UAM build and hence go through the base followed by the base/build interface and then the rest of the UAM stack. When the base/build interface is delaminated, it essentially blinds us to the properties of the stack. It is hence important to also explore NDE techniques which measure the quality of the just bonded foils. Techniques based on potential drop are well established as a tool for NDE of material properties, monitoring the growth of cracks and characterization of defects [65-67]. Alternating Current Potential Drop (ACPD) is one such technique which can be automated to take a measurement after every 5-10 layers of build to estimate the quality of the just bonded foils. In this section, several NDE methods will be explored on UAM components with the objective of designing an in-situ monitoring NDE setup.

### 1.3.1 Linear Ultrasonic NDE: Acoustic Microscopy

Post process immersion C-scan analysis was carried out to study the interface defects in UAM components. A 5 MHz immersion longitudinal transducer was used in a SONIX acoustic microscopy system to scan the surface of the component from the side of the base plate as shown in Fig. 1.6. To clearly distinguish the region of interest, a dotted black line is drawn around the UAM sample. Five such acoustic microscopy images are presented in Fig. 1.7 for the base/build interface and for the stack. The length of these UAM tracks was 101.6 mm and the widths were 25.4 mm. The base/build image had signs of delamination starting from the beginning of the bonding direction. It was observed that the base/build image has strong reflections at the edges where delaminations begin and start to

creep into the sample. The stack image shows a distinctly low quality during the first 25 mm of the track. The dotted circles indicate regions where a 5 MHz longitudinal dual element delay line transducer was used to collect representative waveforms that were then used to calculate ultrasonic velocity. The measured ultrasonic velocity and corresponding elastic stiffness coefficient  $C_{11}$  are shown in Table 1.1. These results indicate that ultrasonic NDE is sensitive to the quality of UAM components. The low-temperature processing and the wide availability of ultrasonic NDE also make it an attractive candidate for in-situ monitoring.

Table 1.1 Experimentally measured ultrasonic velocity and elastic stiffness coefficient.

Build amplitude [ $\mu\text{m}$ ]	Sound velocity [ $\text{mm}/\mu\text{s}$ ]	$C_{11}$ [GPa]
28	5.64	86
29	5.78	90
30	6.04	99
31	6.27	106
32	6.19	103
Intact (Al 6061)	6.35	109

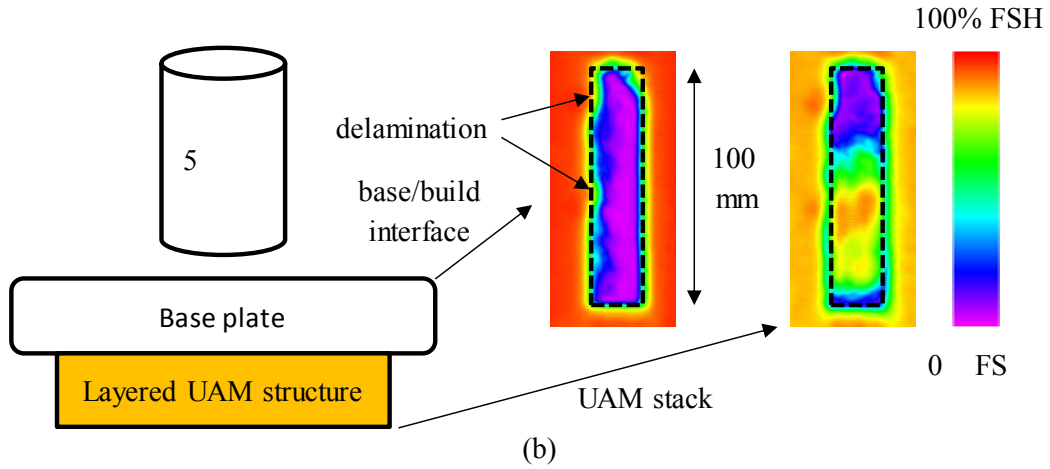


Figure 1.6 A schematic of acoustic microscopy measurements. The base/build image is derived by gating the interface signal while the stack image represents the transmitted

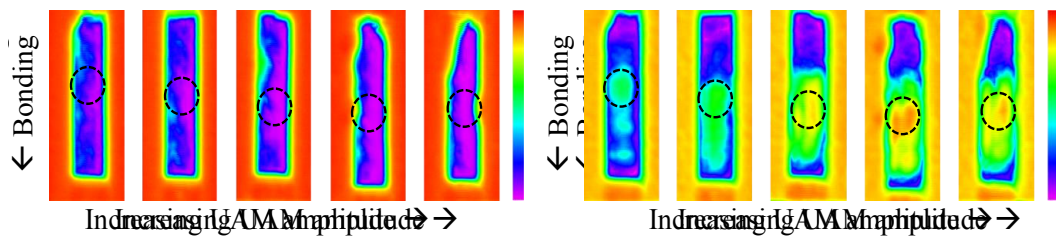
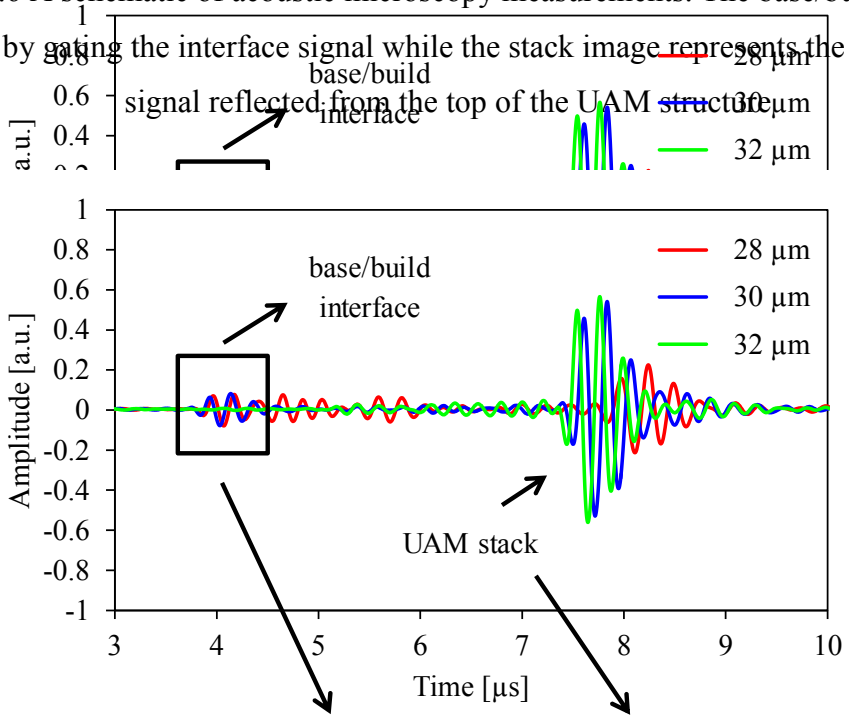


Figure 1.7 Ultrasonic signatures of components built using different vibration amplitudes with acoustic microscopy C-scans of the two gated signals at the bottom

### 1.3.2 Electromagnetic acoustic transducers (EMATs)

Non-contact ultrasonic techniques are attractive for applications where a mechanical coupling or contact is difficult. Two prominent non-contact ultrasonic techniques are laser-based and EMATs. Electromagnetic Acoustic Transducers (EMATs) can generate and detect ultrasonic waves due to contactless electromagnetic coupling with the test object, rather than with mechanical coupling, as in standard piezoelectric probes [48-51]. This feature makes EMATs attractive alternative to piezoelectric transducers in applications where contactless inspections are required. Moreover, EMATs can excite a wide range of wave-modes and can be employed as a standard for ultrasonic calibration. However, EMATs have relatively low signal-to-noise ratio compared to standard transducers. EMATs also offer higher temperature testing capability which is desirable in an industrial environment. UAM processing occurs at up to 200 °C, at these temperatures shear energy does not travel through low density couplants, hence it is difficult to generate them with conventional piezoelectric transducers and is impractical in industrial settings. Electromagnetic acoustic transducers (EMATs), on the other hand, are an effective alternative to generate SH waves for ultrasonic testing. The primary mechanism for sound generation using EMATs is the Lorentz force in non-magnetic materials. In magnetic materials it is added to the magnetostriction [51]. With different combinations of magnet and coil geometry, different varieties of ultrasonic waves can be generated, including longitudinal waves, shear vertical and horizontal waves. EMATs can also be used to generate normal beam, oblique and different types of guided wave testing. Fig. 1.8 shows the typical process of generation of a normal beam with an EMAT along with the magnet and coil orientations for exciting different kinds of ultrasonic waves.

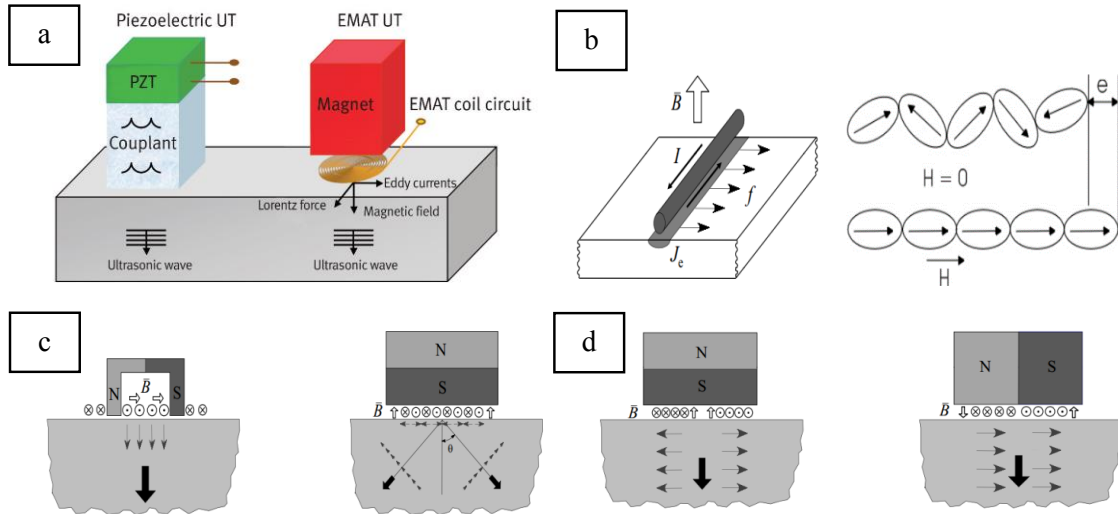


Figure 1.8 (a) EMAT operation, (b) Lorentz Force and Magnetostriction, (c) Longitudinal and Angle beam EMATs, (d) Shear radial and Shear horizontal EMATs [51,52]

An Innerspec Powerbox H portable pulser receiver system with 8 kW of peak power and 1200 V peak to peak tone burst capabilities was used with a radially polarized shear EMAT driven with a 5-cycle tone burst at 2 MHz to inspect UAM components from the top. Measurement from the top is difficult with regular piezo transducers and this test serves to prove the non-contact capability of EMAT even on rough surfaces. 5 measurements were performed at different locations on each sample and all the waveforms were averaged. The ultrasonic shear velocity within 6 UAM samples built with different amplitudes, each with 45 layers (6 mm thickness) was measured. To account for the velocity only through the build layers the average shear velocity in the Aluminum base was measured and accounted for. Fig. 1.9 shows that the shear velocity is sensitive to build parameter variations as expected.

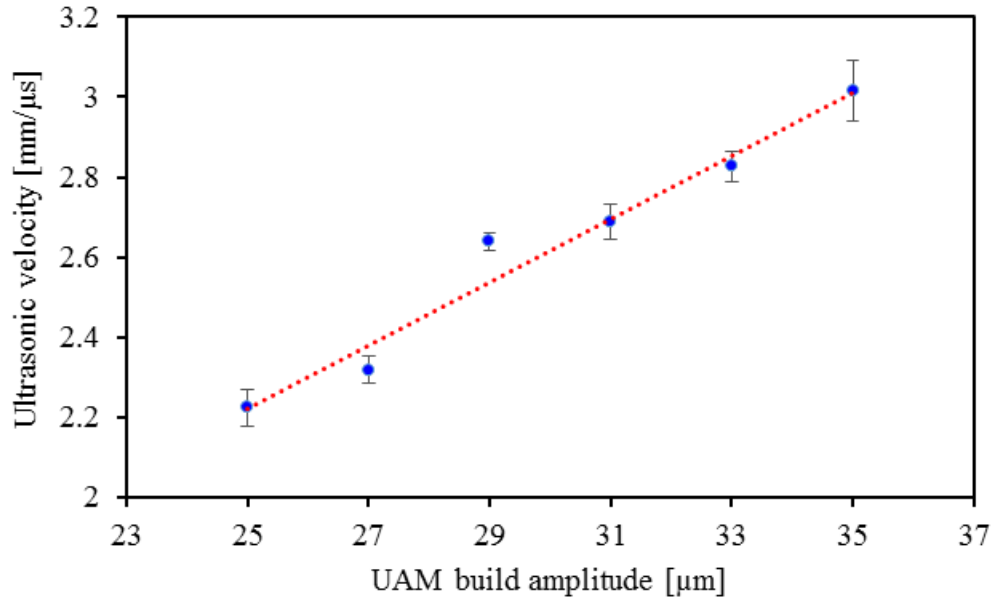


Figure 1.9 Shear velocity variation with build amplitude in UAM components

### 1.3.3 Nonlinear ultrasonic wave mixing

A large body of literature exists on the ability of nonlinear acoustic methods to identify material damage much before it can be detected via linear methods [56-64]. Nonlinear methods are sensitive to microstructural change, dislocation density change, and amount of fatigue damage incurred. When linear techniques can easily detect the damage in a material, it is often late to take preventive/corrective measures. The sensitivity of nonlinear techniques to small changes also hinders the ability to take measurements due to the lack of selectivity. Nonlinear measurements pick up not only contact acoustic nonlinearity (CAN) but also the inherent nonlinearity of the material, that of the coupling medium, that of the transducer and the electronics, which is one of the primary reasons why nonlinear techniques have not become popular for a variety of applications. Wave mixing along with averaging by flipping can solve the issue of suppressing the spurious nonlinearities. Nonlinear mixing takes input signals of frequency  $f_1$  and  $f_2$  and measures

only the output of frequency  $(f_1+f_2)$ . Wave mixing alone would often have several combinations of mode converted waves which brings us to averaging by flipping. An electronically driven pulsing mechanism coupled with intelligent averaging is required to eliminate the nonlinearities that are not of interest. Let  $g_1$  and  $g_2$  be the two input waves that are to be mixed with frequencies  $f_1$  and  $f_2$  respectively. Four transmit receive pairs of waveforms are collected in each cycle, as shown in Table 1.2.

Table 1.2 Averaging via flipping of the linear-mode signals [61]

Wave1	Wave2	Nonlinear Signal (with 2 <sup>nd</sup> Harmonics)	Averaging
$+g_1$	$+g_2$	$+g_1 + g_2 + g_1^2 + g_2^2 + g_1g_2$	+
$-g_1$	$+g_2$	$-g_1 + g_2 + g_1^2 + g_2^2 - g_1g_2$	-
$-g_1$	$-g_2$	$-g_1 - g_2 + g_1^2 + g_2^2 + g_1g_2$	+
$+g_1$	$-g_2$	$+g_1 - g_2 + g_1^2 + g_2^2 - g_1g_2$	-

The resultant of flipping every alternate signal and adding the nonlinear signals is effectively  $4g_1g_2$ , i.e. not only the linear signals, but also the spurious nonlinear signals are eliminated except for the mixing signal. A dual element longitudinal 5 MHz ultrasonic transducer was connected to a two-channel arbitrary function generator which generates the two mixing signals  $g_1$  and  $g_2$  each at 2.8 MHz frequency. The nonlinear mixed signal was obtained by flipping and averaging, the frequency of which would be around 5.6 MHz. The correct signal in the time domain was gated and windowed as shown in Fig. 1.10, Fig.



1.11 and the magnitude of the 6 MHz frequency was chosen as the strength of the nonlinear signal.

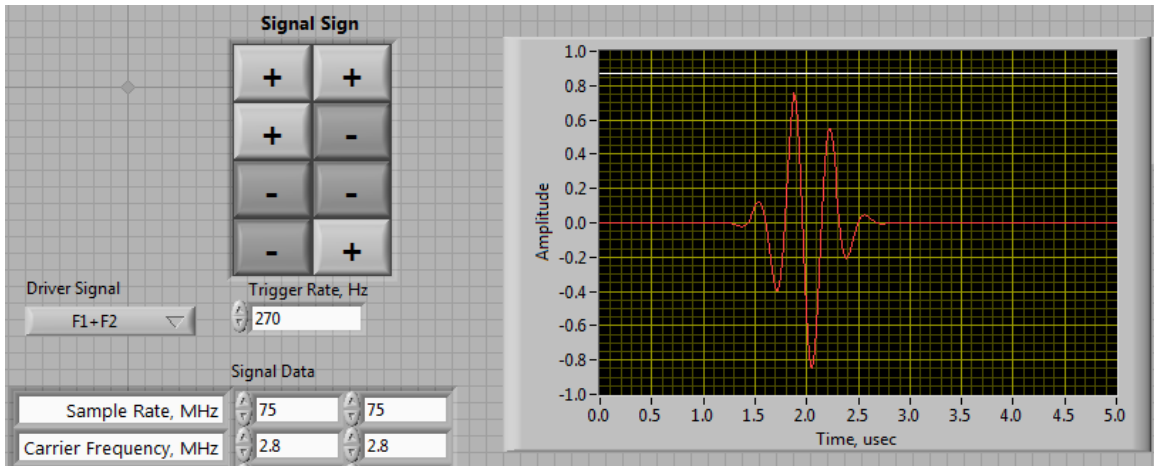


Figure 1.10 The two mixing signals with frequencies 2.8 MHz each

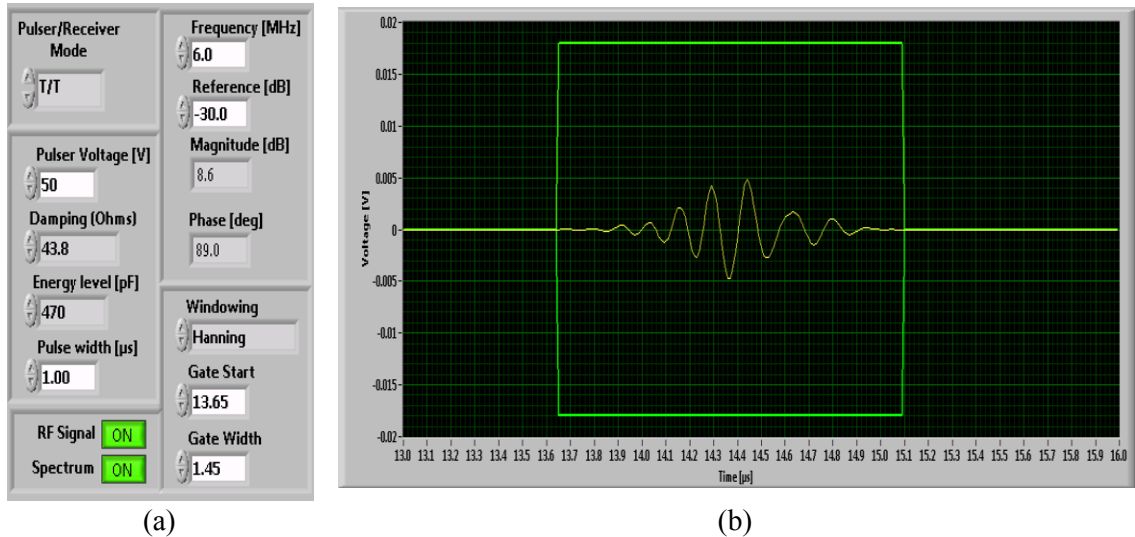


Figure 1.11 Nonlinear signal from a bad region of a UAM component

Similar signals were collected on different components of varying quality, and 10 readings were taken at each location. It was observed that there was significant variability of the signal within different regions of each component. A wrought Al 6061 block of similar thickness was used as an intact specimen for reference comparison. The four kinds of regions were clearly distinguishable between each other (Fig. 1.12). The low build

amplitude sample (25  $\mu\text{m}$ ) had the highest nonlinearity while the higher build amplitude (33  $\mu\text{m}$ ) had a comparatively lower nonlinear response. The response of the intact specimen was significantly lower than any of the UAM samples. Acoustic microscopy was performed on the low build amplitude signal which showed the highest nonlinear signal and the approximate region where this occurred is shown in the reflection and transmission images in Fig. 1.13a, 1.13b respectively.

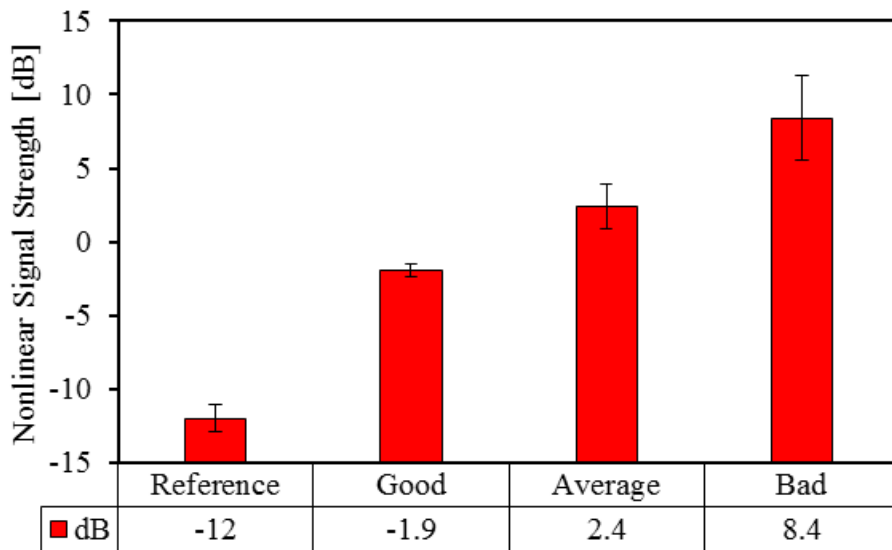


Figure 1.12 Nonlinear signal measured on four different samples at approximately one location close to the center of each sample

It was demonstrated in literature that linear inspection based on attenuation/velocity, is not sensitive enough for initial damage accumulation over the first 25-50% of fatigue life, while nonlinear inspection shows a monotonically rising damage level due to increasing dislocation density. However, the nonlinearity quickly saturates as dislocations become pinned, therefore no significant further increase occurs during the remaining fatigue life of the component. At a later stage, the linear attenuation of the material starts to increase due to the formation of multiple-site microcracks and the measured “effective

nonlinearity declines from its saturated level because of the increasing attenuation especially at higher frequencies.

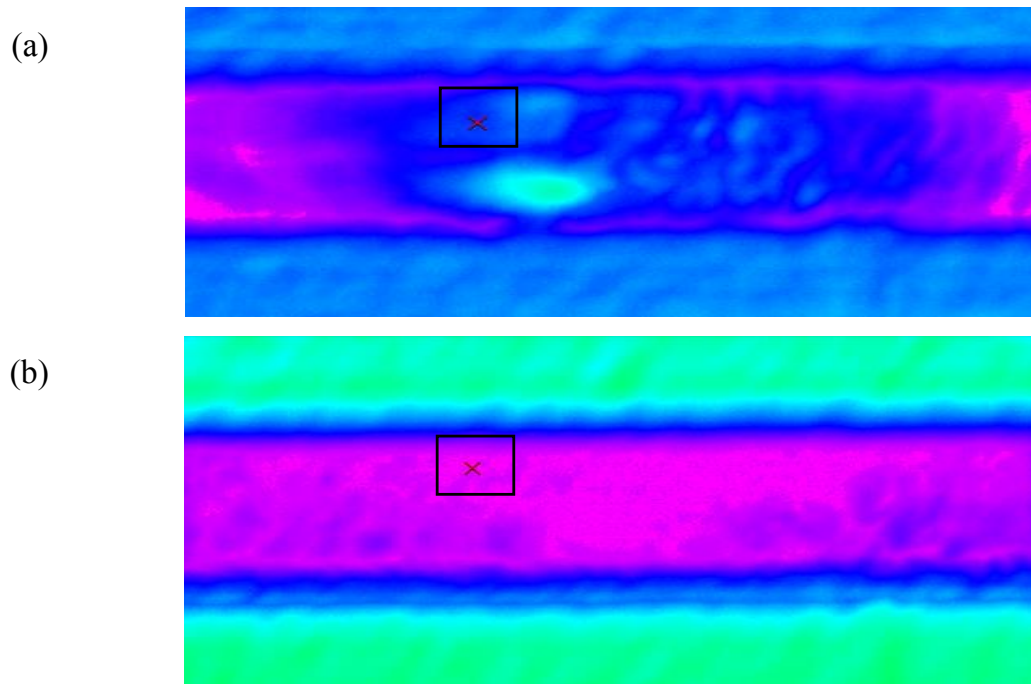


Figure 1.13 (a) Transmission image, (b) Reflection (base/build interface) image. The nonlinear signal is highest at the cross marks

The advantage of the nonlinear wave-mixing is that the same dual element transducer that can be used for linear ultrasonic measurements can also measure the material nonlinearity. With respect to in-situ monitoring in UAM, simply increasing the complexity of the electronics involved, a system capable of linear as well as nonlinear measurements can be setup. While the initial investment is high, the rewards might potentially outweigh the cost of adding a nonlinear wave mixing option to a linear ultrasonic setup.

### 1.3.4 Phased array

Ultrasonic measurements are indirect, meaning that the measured outputs, which are usually in the form of electrical voltage versus time signals, are the result of complex transformations of the acoustic energy that is generated and received, making it difficult to connect the characteristics of the measured signals directly with the properties of the object being examined.

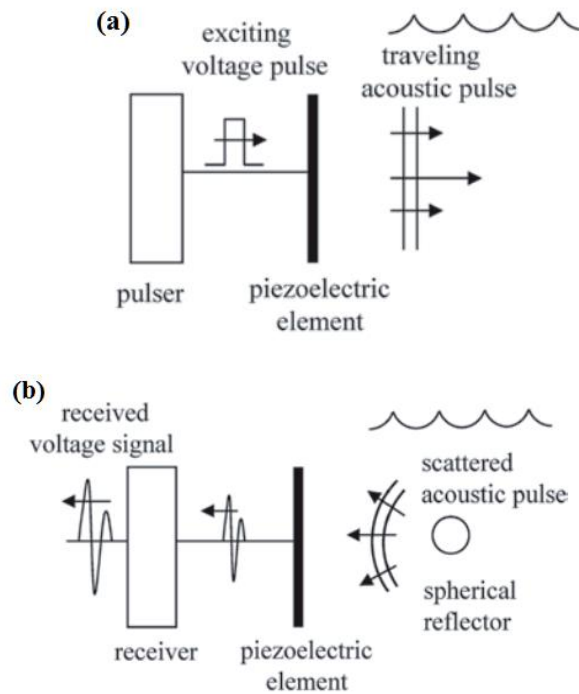


Figure 1.14 (a) A single element ultrasonic transducer generating a traveling wave, and (b) the same transducer receiving the waves scattered from a spherical reflector [54]

To illustrate the difficulty, consider the simple ultrasonic system outlined in Fig. 1.14, where a single element ultrasonic transducer is placed in a fluid. If the transducer is excited by an electrical pulse, as shown in Fig. 1.14a, a traveling pulse of sound will be generated in the water in the form of an acoustic wave. If this wave strikes an object such as a spherical reflector, as shown in Fig. 1.14b, then waves will be scattered from the sphere

in all directions and some of that scattered acoustic energy will return to the transducer. Knowing the wave speed of the fluid and the time of arrival of this pulse, the distance to the sphere can be estimated, but other quantitative information such as the size or its mechanical properties. are not obvious from the measured signal. Mechanically moving a single element transducer results in a collection of measured signals that can be used to help better determine quantitative information about defects and delaminations within a component. With sufficient information obtained from such mechanical motion of the transducer, an ultrasonic image can be formed as demonstrated in Sec. 1.3.1. However, mechanical scanning is slow and expensive to perform with a single element transducer setup. Also, it is practically infeasible to have a scanning system which collects data via rastering after each UAM build.

A more effective approach to conduct inspections and form images is to use an ultrasonic phased array, where the sound beam can be manipulated electronically. It is possible with the help of the right algorithms to develop a correlation between the nature of the scatterers and the ultrasonic signals and thus perform imaging. Ultrasonic array probes consist of many individually wired ultrasonic elements within a single transducer package. In a phased array setup (Fig. 1.15), the ultrasonic transducer is composed of an array of small piezoelectric elements, where each element can be separately driven, and the response of each element independently received. If each of the elements is driven in an identical fashion so that the driving electrical pulses travel in unison, then each element of the array acts as a point source and radiates a spherical wave. These spherical waves combine to form a traveling wave pulse as shown in Fig. 1.15a.

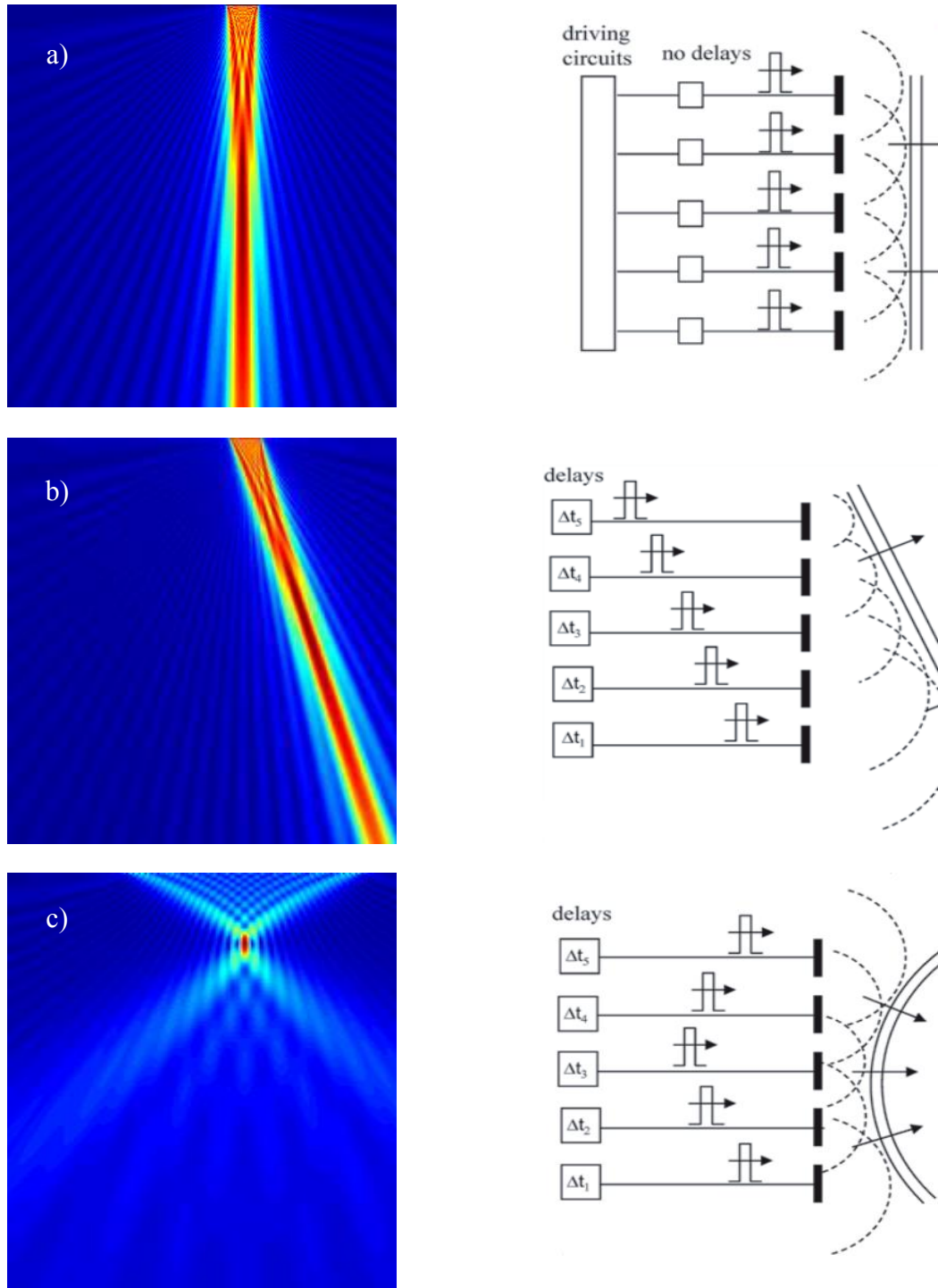
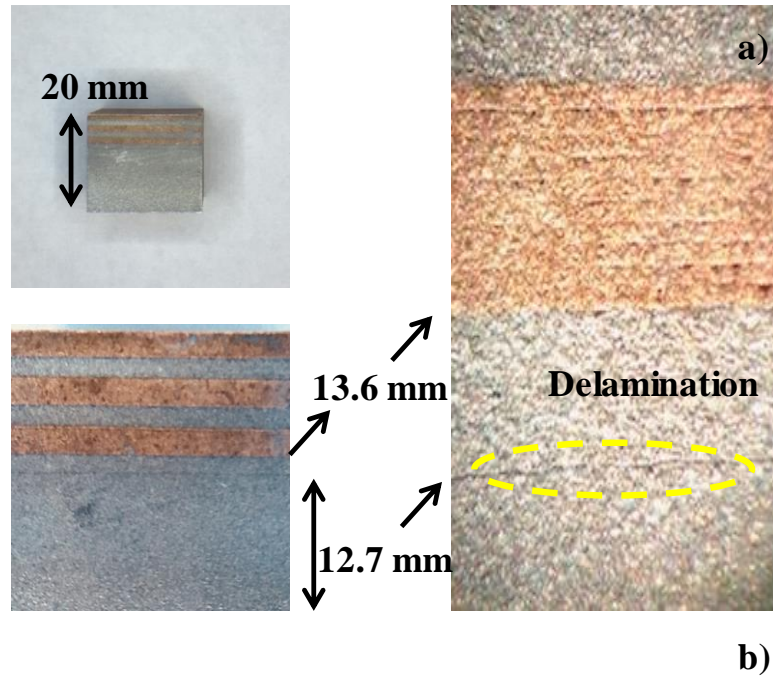


Figure 1.15 (a) An ultrasonic phased array, where the driving electrical pulses for each element arrive in unison, (b) An ultrasonic phased array where a set of delays are used to steer the sound beam of the array and, (c) The case where a set of delays produce a focusing of the sound beam [54]



Mode- A

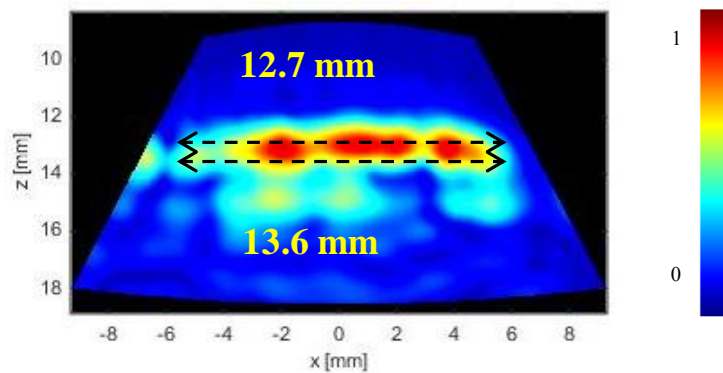


Figure 1.16 (a) Aluminum-copper composite manufactured by UAM (b) Phased array imaging using beam forming to focus at various depths inside the UAM sample

Except in a region close to the array the sound beam of the array is like the beam generated by a single element transducer of the same size as that of the entire array. However, by varying the relative time delays,  $\Delta t_i$ , of the driving pulses (where the ensemble of delays is called a delay law), the ultrasonic phased array can electronically steer the sound beam generated in different directions, as shown in Fig. 1.15b. With an appropriate non-linear delay law, the same array can also generate a focused sound beam as shown in

Fig. 1.15c. A more complex combination of these delay laws can simultaneously perform both beam steering and focusing. Relative time delays for each element can also be used for modifying the characteristics of the signals received by an array.

To test the phased array system, an aluminum-copper composite was manufactured by UAM with Al 6061 H18 foils and pure copper foils. The aluminum and copper foils were 150  $\mu\text{m}$  in thickness. 6 layers of aluminum and 10 layers of copper were laid in bands to form the composite. The substrate was also aluminum and can be considered a part of the composite sample. Multi-material composites are used in structural applications especially when impact strength and weight reduction are of significance. Fig. 1.16a shows the Al-Cu composite structure with a large delamination at the substrate aluminum interface (12.7 mm depth). The preceding 6 layers are well bonded to each other followed by the 10 layers of copper which have porosity from sections of poorly welded zones. The first aluminum-copper interface appears to have reasonable bonding with no clear delamination. An image formed by a one dimensional (1D) linear 32-element phased array transducer is shown in Fig. 1.16b. Not only is the delamination at 12.7 mm evident, but also reflections from within the composite were imaged.

1D-linear arrays can only provide focusing and beam steering in a single plane [55]. However, 2D arrays, with elements arranged in a 2D plane, can manipulate an ultrasonic beam in every direction in the volume beneath the array, improving inspection coverage and sensitivity. It is hence important to include phased array ultrasonics in the list of potential in-situ NDE techniques.



### 1.3.5 Nonlinear Vibro-Modulation

Acoustic nonlinear phenomena applied to nondestructive evaluation is a well-researched topic [56-64]. The remarkable strength of many nonlinear effects introduced by defects makes their use for damage detection very attractive. Two main nonlinear effects have been studied extensively for NDE applications: (i) measuring the wave speed dependence on the wave amplitude; (ii) monitoring the generation of harmonics. In both cases the evolution of the nonlinear effect can be studied over time for e.g., for fatigue monitoring. Contact acoustic nonlinearities (CAN's) are typically solid-to-solid interfaces with imperfect adhesion, such as cracks, disbonds, etc. Vibro-acoustic modulation is based on this kind of nonlinearity. If an undamaged specimen is subjected to both a low frequency vibration and an ultrasound probing signal, the resultant field is simply the superposition of the fields obtained by applying the two excitations separately.

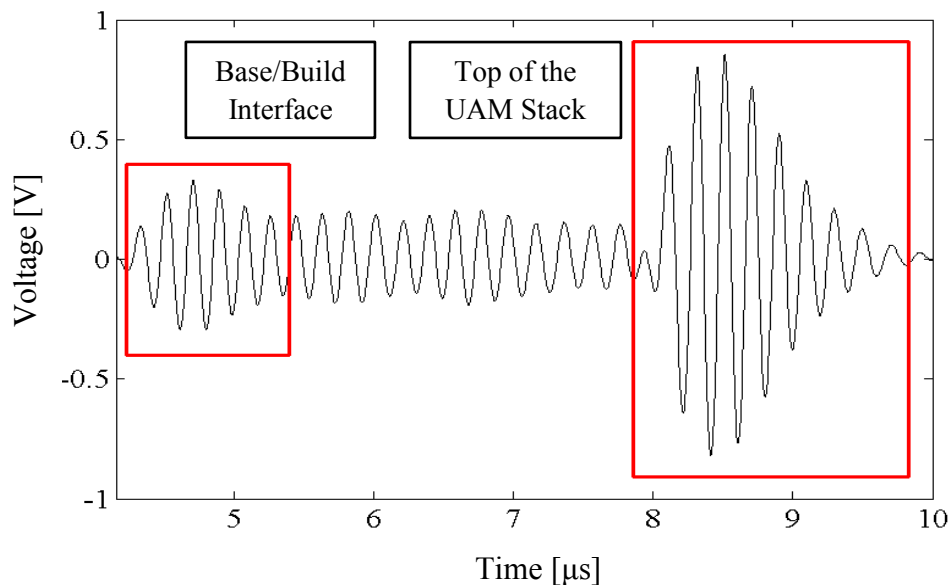


Figure 1.17 In-situ signal using the dual element delay line transducer after 80 layers

However, if the system is damaged for e.g., by a crack or some debonding, the two vibrations interact so that the ultrasound wave is modulated in amplitude and/or phase [56] by the low frequency oscillation. Therefore, the occurrence of amplitude modulation in such a setup can be taken as an indication of the presence of damage in the specimen and could be used as the basis of a nondestructive technique for damage detection. In practice, the phenomenon is usually studied in the frequency domain where the modulating effect is manifested by the presence of sidebands around the main peak at the ultrasonic frequency.

In UAM components it is theorized that a high frequency carrier ultrasonic signal can be modulated by the inherent structural vibrations caused by the low 20 kHz frequency of the bonding process. The modulation can reveal the extent of damage within the whole component and specifically the base/build interface. The novelty lies in the fact that the inherent structural vibrations of the UAM process are utilized for this analysis making it an ideal addition to an in-situ monitoring setup. If the carrier ultrasonic signal is applied from below, it would face two kinds of modulations. The first being the gradual increase of the applied force (5000 N) until the welding head is right on top of the location of the transducer and then a further gradual decrease. Such a modulation occurs once every layer. The second kind of modulation is in the 20 kHz vibration of the welding head and its effect on the carrier signal usually in the MHz range. To verify the effect of modulation during the welding process an experiment was designed to continuously monitor the ultrasonic signals throughout the UAM build process. The UAM base plate was raised by supports to incorporate the ultrasonic transducer below for in-situ experiments. A continuous data capture was performed at a repetition frequency of 4 kHz by monitoring from below the base. A delay line dual element 5 MHz transducer is utilized. The 4 kHz sampling rate is

insufficient to study the second type of modulation that occurs at 20 kHz. The data from the continuous monitoring was written directly onto a solid-state hard drive.

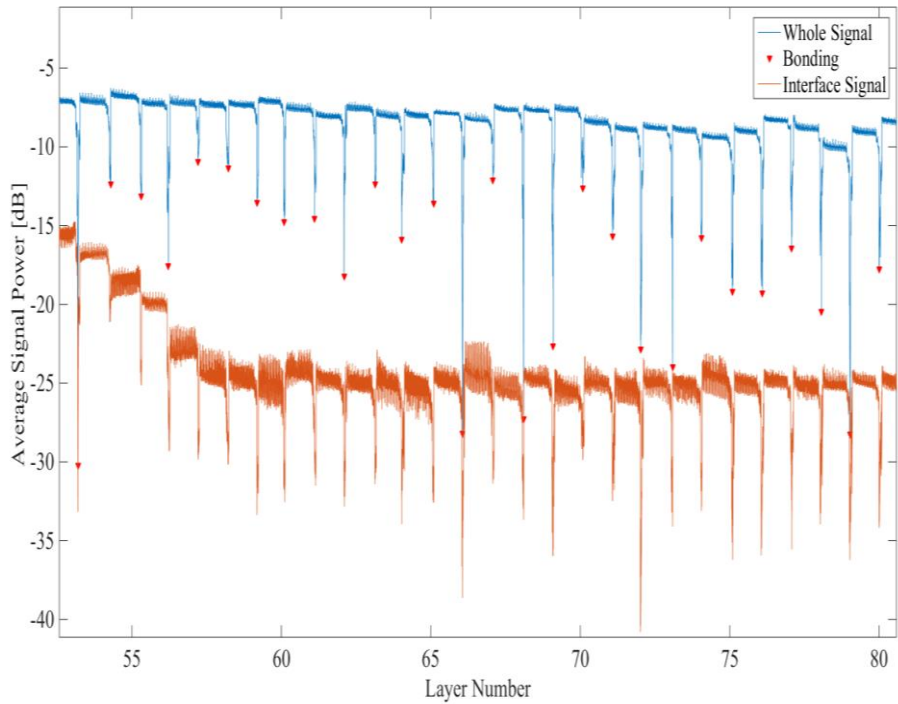


Figure 1.18 Average signal power during continuous monitoring during the UAM build

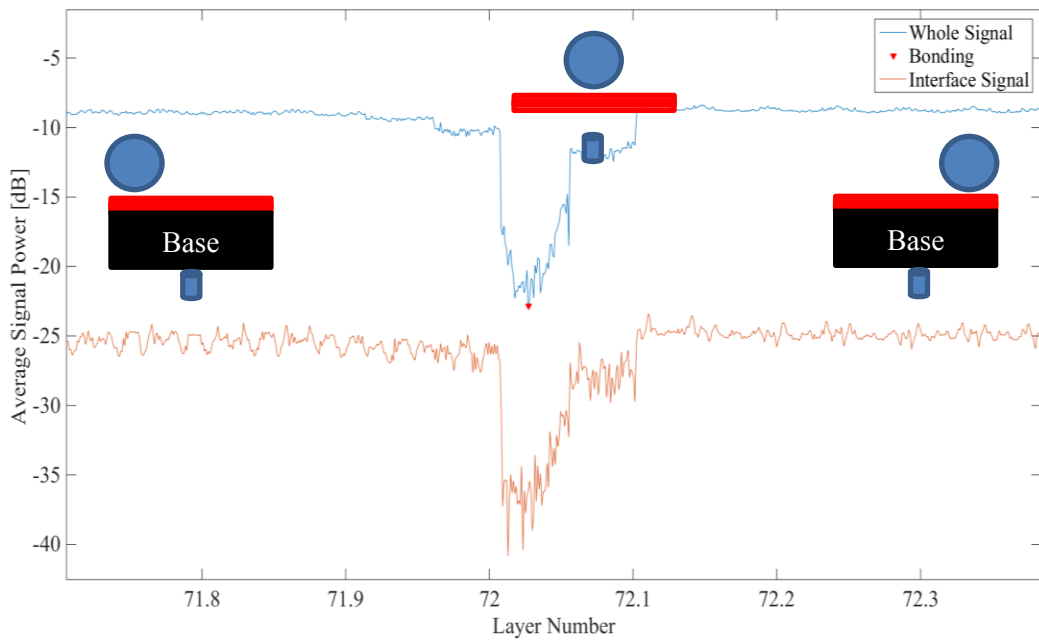


Figure 1.19 Average signal power variation due to force modulation during a UAM build

The repetition frequency was limited by the rate of data transfer but even so, 4000 Hz is a significantly high time resolution for analyzing what happens during a 1.5 second weld process for a single layer. 80 such layers were built to make a single component and 5 different build amplitudes were selected to build a set of components. Five such replicates were built to make 25 components of 80 layers each, with continuous monitoring throughout the build process. In Fig. 1.17 we see the signal after 80 layers from a sample.

The large amount of data that was collected during the bonding process was averaged 40 times so that the effective repetition frequency is 100 Hz, i.e. every second 100 A-Scans are collected. Preliminary results for the modulation due to the applied force are presented. Fig. 1.18 shows the average power of each averaged waveform from layer 55 onwards. Between any two layers there are 1000 waveforms whose average power is represented as a single point. It is seen that the root mean square (RMS) power of the signal significantly drops when a new layer is added. Those peaks are identified by red markers and are utilized for data analysis around the bonding zones. The signal from the base/build interface is windowed and its power is also plotted. When the weld head is right in the center of the bonding zone it is expected that the average power of the signal significantly drops due to the force applied as seen in Fig. 1.19.

There is a high degree of correlation between the drop in the total signal power as compared to that of the interface signal power. Not only is there a correlation, the value of the drop in the interface signal is almost the same as the value of the drop in the interface signal. This essentially means that what we are observing is an effect of the coupling medium as that is the only common variable that relates to both the interface as well as the total signal. It is elementary to re-design the system where the coupling medium has a

reservoir and hence is not going to affect the signals. In such a case, the modulation of the force would indicate the imperfections at the base/build interface. While the damage to the base/build interface can currently be observed, the interface signals from within the UAM build are often small and it is difficult to estimate the extent of damage via linear methods. Nonlinear techniques such as modulation have the potential to estimate such damage as the layers are being built.

### 1.3.6 Alternating Current Potential Drop

In the field of Non-Destructive Testing, Potential Drop (PD) techniques have been used for decades (65-67), especially in the petrochemical and power generation industries, for monitoring crack growth and wall thickness variations due to corrosion and/or erosion in pipes, pressure vessels and other structures. Inspection is carried out by injecting currents in the specimen to be tested and measuring the arising electrical potential difference between two or more electrodes placed on its surface. The presence of a defect generally increases the resistance and hence the measured voltage drop; inversion of these data can give information on the size and shape of the defect. There are two types of potential drop techniques, Direct Current (DCPD) and Alternating Current (ACPD). Potential drop techniques use a four-point measurement system as shown in Fig. 1.20. Two of the electrodes are used for current injection and the other two for measurement of resistance. The penetration depth is limited by the electromagnetic skin depth when  $\delta$  is smaller than half the distance between injection electrodes. It is dependent on the inspection frequency, magnetic permeability, and electrical conductivity of the material according to  $\delta=1/\sqrt{\pi f \mu \sigma}$ .

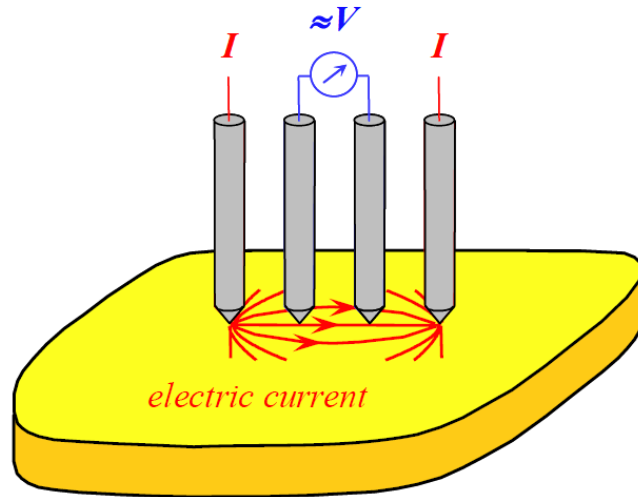


Figure 1.20 Schematic diagram of a Potential Drop measurement [67]

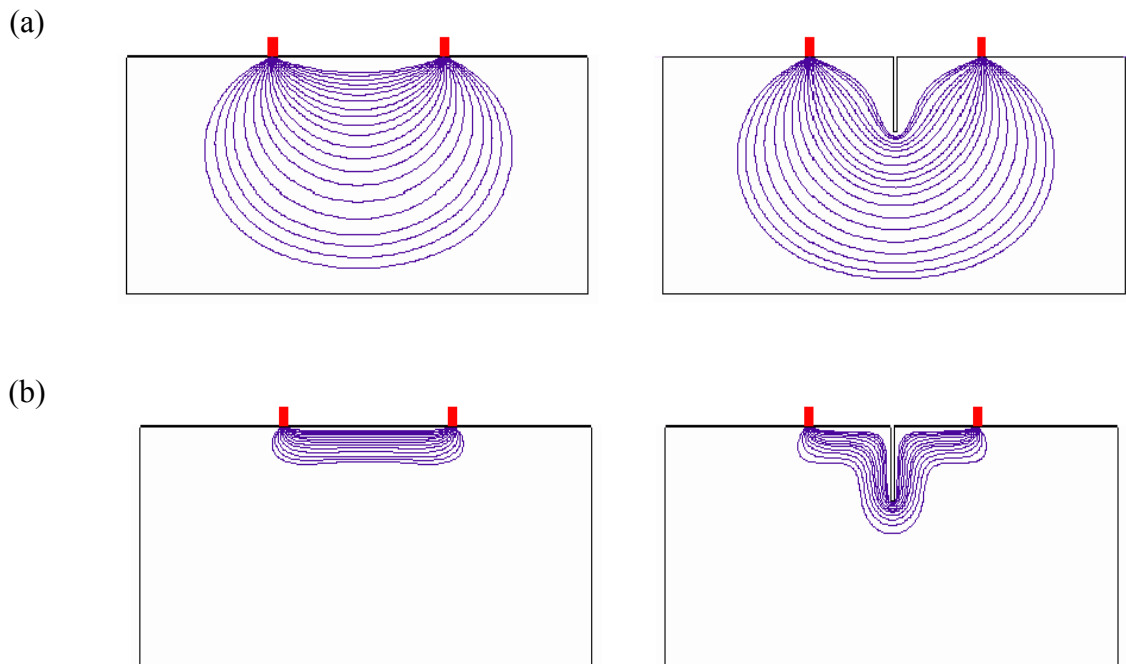


Figure 1.21 Current distribution in sound and cracked specimens using (a) DCPD and (b) ACPD [65]

At very low frequencies, the current distribution asymptotically approaches the static distribution of the direct current potential drop (DCPD) method with a geometrical

penetration depth roughly equal to half the distance between the injection electrodes. The main advantage of ACPD mode of operation over DCPD is that the same injection current produces much larger potential differences [66]. Using this technique, the measured resistance increases when the probe overlaps a defect because the injected current is forced to travel around and underneath the defect, such as a surface breaking crack, which leads to increasing potential drop between the sensing electrodes [66]. Fig. 1.21 shows the current distribution in intact and cracked specimens using DCPD and ACPD inspection techniques.

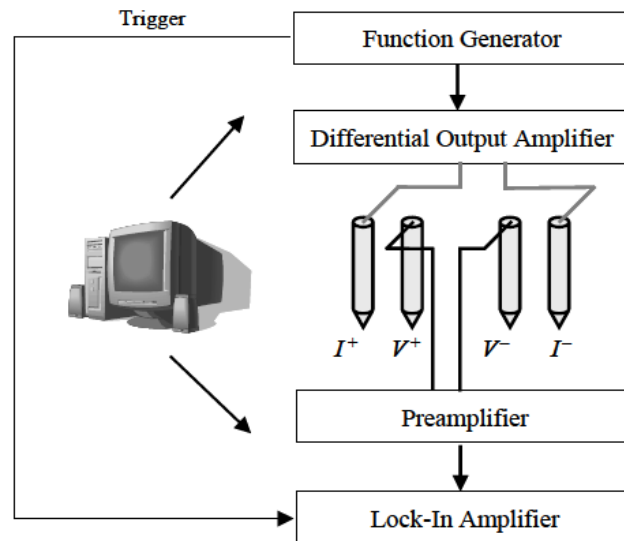


Figure 1.22 Block diagram of an ACPD experiment [66]

In the DCPD scenario the injected current spreads out through the whole cross section of the specimen limited only by the electrode separation whereas in the ACPD case the penetration depth is readily controlled by the inspection frequency through the electromagnetic skin depth. This makes ACPD attractive for testing UAM components. In a layered metallic structure the electric current flow would be tortuous if there are

imperfections at the interface of each layer. This means that the current takes a much longer path due to the presence of several imperfect interfaces which would result in a higher resistance measured.

A typical block diagram of an ACPD experimental setup is shown in Fig. 1.22. The signal coming from a function generator passes through a differential output amplifier, whose purpose is to ensure that the currents injected into the material through the first pair of electrodes of the probe are of equal amplitude and opposite sign. The voltage measured at the second pair of probe electrodes is fed through a pre-amplifier and then read with a lock-in amplifier. The measurements can be automated by using a computer to operate all the instrumentation through a routine written in LabVIEW. A similar setup was used to collect data on a factorial set of UAM components ranging from build amplitudes 25  $\mu\text{m}$  to 35  $\mu\text{m}$ . It has been observed via acoustic microscopy that build quality variations exist within a sample from bond start to bond finish. Typically, there are more delaminations at the bond start region. Fig. 1.23 shows the average resistance measured within set of 18 UAM samples with 20 measurements per sample taken at the center of the build. It is observed that samples built with 25 and 27  $\mu\text{m}$ , are of lower quality than the rest of the samples which are of lower quality than the baseline measurement on a solid Al block. The measurement only works because at the low inspection frequency (16 Hz) the skin depth ( $\delta \sim 30 \text{ mm}$ ) is larger than twice the electrode separation ( $s = 10 \text{ mm}$ ). This introduces a normal component to the ACPD measurement thus allowing the current to travel through the UAM layers and thus be sensitive to imperfections.



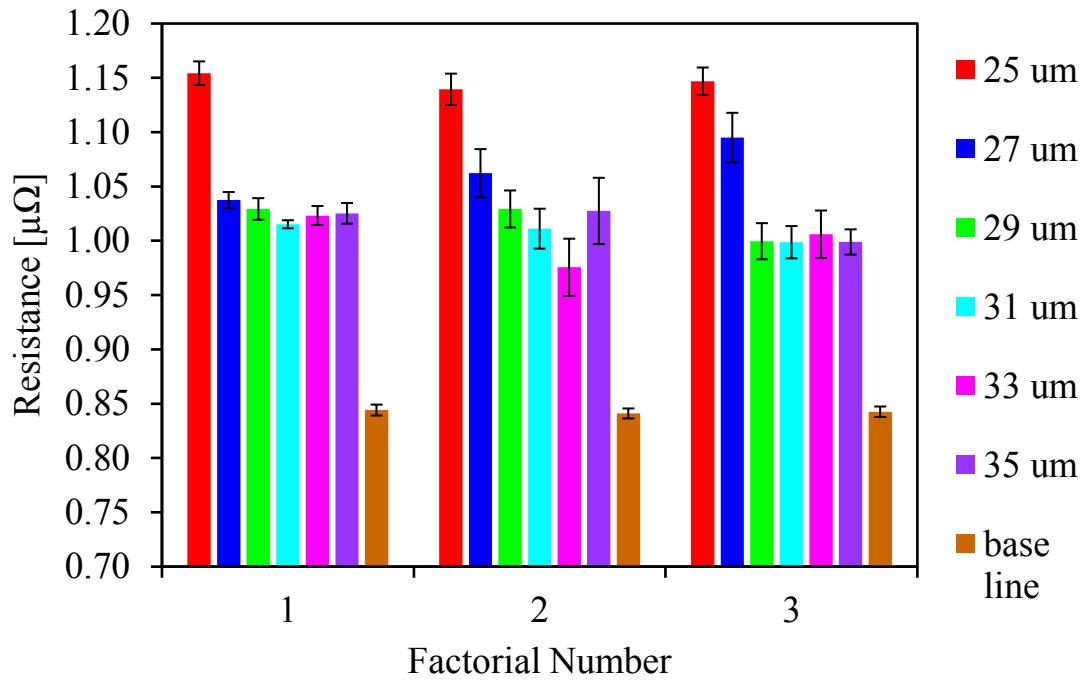


Figure 1.23 ACPD resistance across a factorial design of UAM builds

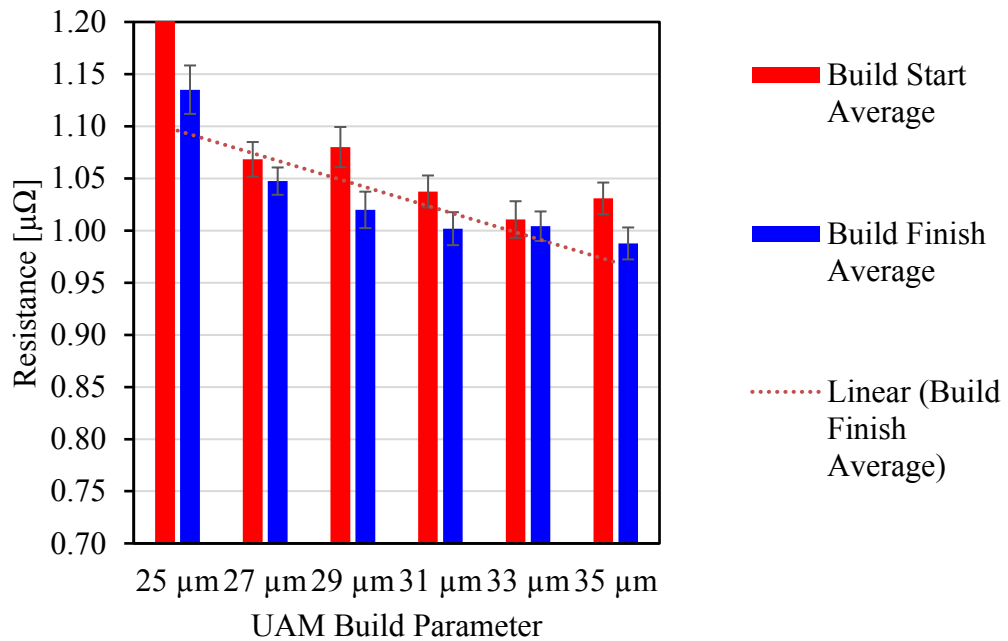


Figure 1.24 Average ACPD resistance variation from build start to build Finish across a factorial design of UAM samples

It was experimentally shown that depending on the build parameters, anywhere from 5- 60% of the whole bonded region could be tightly shut kissing bonds [26]. A tensile test in the Z-direction and further microscopy to observe the fracture surface confirm the existence of tightly shut interface defects. Hence, the electric current would take a very tortuous path at each interface where it encounters delamination and kissing bonds. Fig. 1.24 shows the comparison of the bond quality variations between the bond start and bond finish. The value at the bond start of 25  $\mu\text{m}$  sample was much higher than the rest of the values (500 % higher), hence the top of that bar is not represented. The average trends show that ACPD technique is sensitive to build parameter variations, but it might be much more sensitive to localized geometrical, material variations at the point of contact. ACPD is worth exploring in the context of UAM since it is a potentially automatable technique for nondestructively measuring the quality of just bonded UAM layers.

### 1.3.7 Review and selection of NDE method

Several NDE techniques were studied in a laboratory setting for their sensitivity, robustness, cost, and ease of implementation in an industrial setting. Most of the techniques tested were based on ultrasonic measurement due to its sensitivity to the defects in UAM, Linear single element ultrasonic NDE is a well understood, widely available, cost-effective technique. Linear phased array ultrasonic testing is a more expensive but provides the advantage of imaging the defects and components. Due to the sensitivity of ultrasound to defects in UAM, either a high frequency measurement is required to resolve the defect, which limits the propagation distance and thus volume inspectable, or model-based approach is necessary to interpret the results. EMATs are effective at generating shear

waves which are difficult to achieve in traditional PZT transducers. Nonlinear ultrasonic techniques like vibro-modulation and wave-mixing are promising in a laboratory setting but not feasible in an industrial environment. ACPD measurement is also promising for detecting defects from above but it requires stopping the manufacturing process after every few layers to take a measurement. In-situ NDE measurements are best performed continuously without interrupting the manufacturing process and without altering component quality. Introduction of an NDE sensor below the base plate can also alter the quality of the UAM components due to the change in vibration characteristics, hence having a smaller sensor is better. From the results presented in this section, linear ultrasonic methods such as PZT, EMAT and phased array are the best options for monitoring in-situ from below the base plate. Considering the cost and ease of industrial implementation, PZT ultrasonic NDE sensors were chosen as the NDE method for in-situ monitoring of UAM components.

#### 1.4 Laser Powder Bed Fusion Additive Manufacturing

Laser Powder Bed Fusion (L-PBF) is a prominent additive manufacturing (AM) process that produces parts directly from a 3D CAD model [68]. During the L-PBF process, the CAD model is sliced into layers and a focused laser beam is used to melt metallic powder into a solid part according to the contour information of the slice layers. Inside the build chamber, there is a material dispensing platform and a build platform along with the recoater blade used to lay a thin layer of powder as shown in Fig. 1.25.

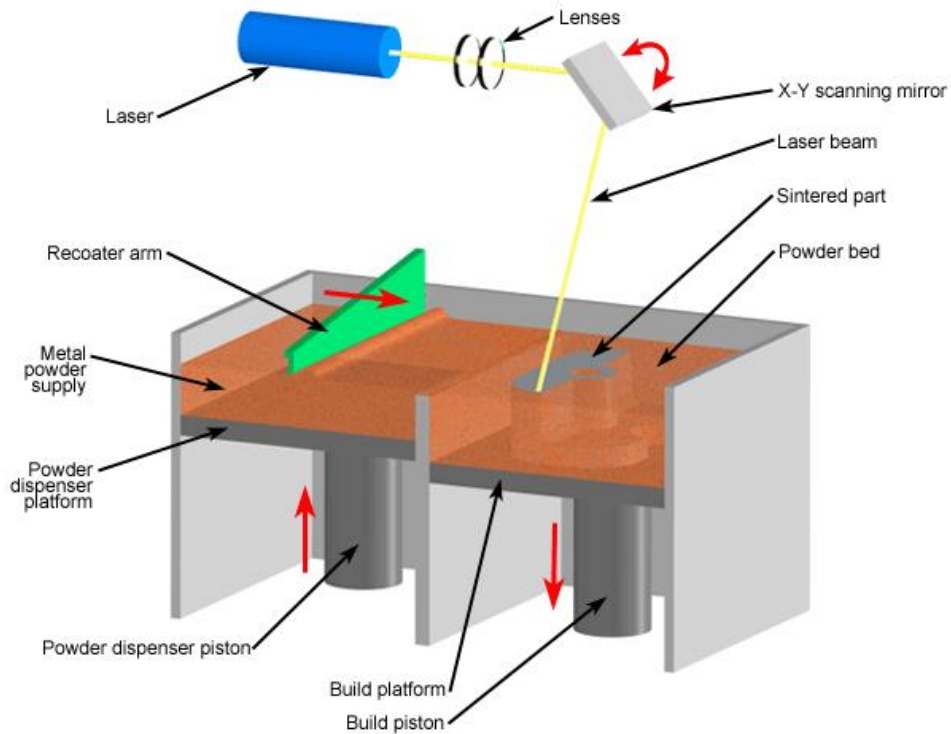


Figure 1.25 Schematic of L-PBF process (From EOS GMBH)

Metal AM components are designed to be used for functional applications in various materials including stainless steel, cobalt chromium, titanium, and Inconel super alloys. The L-PBF process chain involves a wide range of processing parameters and build conditions for making the AM component. Post-process annealing, heat treatment, HIPing and milling are often required to achieve necessary dimensional tolerance and structural performance. While the post-process treatments are a good way to deal with existing problems with L-PBF components, the best solution is to have a better-quality product coming out of the L-PBF system.

The properties of AM parts are dramatically influenced by build conditions referring to process parameters, scanning strategy and raw material characteristics. Several investigations have been conducted that are focused on optimizing these build conditions

to improve the mechanical properties [69-77]. For a given set of build conditions, a useful parameter energy density is defined as

$$E_d = \frac{P}{vht}, \quad (1.1)$$

where,  $E_d$  is the energy density,  $P$  is the laser power,  $v$  is the scan speed,  $h$  is the hatch spacing, and  $t$  is the layer thickness. Several works have reported that for a given laser power ( $P$ ), there is an optimal range of energy density in which fully dense parts can be fabricated [71]. Lower energy input causes defects due to incomplete melting, while higher energy causes keyhole porosity and residual stress build up. The optimal energy density band also varies based on the laser power. At higher power ( $> 200$  W), the band is wider [75] and therefore we observe a surge in commercial availability of L-PBF systems offering higher laser power. Developing optimal process parameters for a new material is an expensive undertaking involving the manufacture of several coupons, and mechanical test bars. Typically, coupons are built with a wide range of build conditions to study the density through Archimedes' porosity and optical microscopy. An energy density band is identified within which components are close to fully dense ( $>99\%$ ). The process is further repeated by zoning into the optimal energy band until the coupons have close to 100% density. At this stage, tensile and fatigue bars can be manufactured to further optimize the mechanical strength of the L-PBF components.

This methodology for developing process parameters is expensive as it requires several days of machine time followed by metallurgical and mechanical sample preparation and testing. Furthermore, variability in scan strategy, powder characteristics, build geometry and environmental factors can all lead to varying structural performance. For instance, scan strategy and geometry can affect the residual stress, microstructure and thus

mechanical properties [78,79], the choice of laser power and environmental factors can affect the denudation and spatter of powder particles [80]. As the number of build conditions increase, the number of components required to arrive at optimal process parameters also increases. Even though several process conditions are kept constant and the number of variable build conditions is reduced, different process parameters need to be developed for different geometries. Several studies have thus focused on using simulation to suggest process parameters changes [81-83].

In-situ nondestructive evaluation can potentially be used for process parameter development. It might be cost-effective to try several build conditions and geometries in a single coupon by using nondestructive evaluation. Several in-situ monitoring approaches have been published in literature with varying degrees of success [84]. For instance, melt pool monitoring and spatter signature [85], X-ray imaging [86], in-situ metrology [87], distortion and temperature measurement [88], eddy current [89], and ultrasonic NDE [90-92] have been successfully demonstrated as potential in-situ monitoring tools. Of the various methods, ultrasonic NDE is a cost-effective method for developing process parameters for components with regular geometries ranging from cube shaped coupons to thin walls.

Depending upon energy density, typical L-PBF process parameters can be subdivided into three zones according to Gong *et al.* [70]. Zone I parameters give rise to fully dense components. Zone II consists of ‘over-melting parameters’ while Zone III consists of ‘under-melting parameters’. Zone II and Zone III parameters generate defects, due to excessive or insufficient energy input, respectively.

Table 1.3 Build parameters used to manufacture Ti-6Al-4V components, Gong *et al.* [71].  
 Process constants are hatch spacing of 0.1 mm, layer thickness of 0.03 mm

Component set	Power [W]	Scan speed [mm/s]	$R_D$ [%]	$E$ [GPa]
Set-1 Optimum (Zone I)	80	480	0.2	N/A
	80	600	0.1	N/A
	80	720	0.2	N/A
Set-1 Over-melting (Zone II)	80	240	0.6	N/A
	80	360	0.3	N/A
Set-1 under-melting (Zone III)	80	840	0.9	N/A
	80	960	2.4	N/A
	80	1080	3.9	N/A
	80	1200	6.0	N/A
Set-2 Zone I	120	960	~ 0.1	109 (2.1)
Set-2 Zone II	120	400	~ 0.5	111 (1.4)
	120	540	~ 1.0	109 (3.7)
Set-2 Zone III	120	1260	~ 1.0	95 (3.0)
	120	1500	~ 5.0	84 (3.0)

Gong *et al.* [70] built two sets of components. Set-1 consists of only coupons built at 80 W laser power and varying scan speed. Set-2 had both coupons and tensile bars in the same L-PBF build. The Young's modulus value that has been calculated by destructive tensile tests was presented in Gong *et al.* [71]. An EOS M270 L-PBF system was utilized for building 10 mm cube-shaped coupons using Grade 23 Raymor Ti-6Al-4V powder.

Scanning speed and laser power were varied, with constant hatch spacing (0.1mm) and layer thickness (0.03mm). Each specimen density was measured using the Archimedes' method and then compared with the normal density of the Ti-6Al-4V material to estimate porosity ( $R_D$ ). The scan speed, laser power, corresponding Archimedes' porosity and Young's modulus of the two sets of components are shown in Table 1.3.

It is well known that ultrasonic parameters can be correlated to porosity. Slotwinski and Garboczi showed that AM component porosity can be estimated through ultrasonic NDE [101]. Wave velocity can be used to estimate the elastic stiffness coefficient according to the equation

$$C_{11} = \rho c^2, \quad (1.2)$$

where  $C_{11}$  is the stiffness coefficient along the direction of wave propagation,  $\rho$  is the material density and  $c$  is the longitudinal wave velocity. The wave velocity is calculated through a Fourier domain cross-correlation between the input and output ultrasonic signals. In pulse-echo mode, the phase delay of an ultrasonic signal is calculated as it travels twice through the AM component. The thickness of the AM component is measured using digital calipers, and the wave velocity and the stiffness coefficient are calculated. From the stiffness coefficient, we can estimate the Young's modulus ( $E$ ) if we know the Poisson's ratio ( $\nu$ ) according to the formula,

$$E = C_{11} \frac{(1+\nu)(1-2\nu)}{1-\nu}. \quad (1.3)$$

L-PBF components can be anisotropic and thus have directionally-dependent Poisson's ratio based on process parameters. For the sake of comparing the NDE results with destructive tests, we assume isotropic material with a constant Poisson's ratio ( $\nu = 0.33$ ) regardless of the direction. We can then estimate the Young's modulus from NDE



henceforth referred to as the NDE modulus and its relation to porosity using the coupons made with parameters presented in Table 1.3. Fig. 1.26a shows that as the porosity decreases, the NDE modulus increases as expected. In Fig. 1.26b, the relationship between the NDE modulus and the Young's modulus from destructive tensile tests is presented.

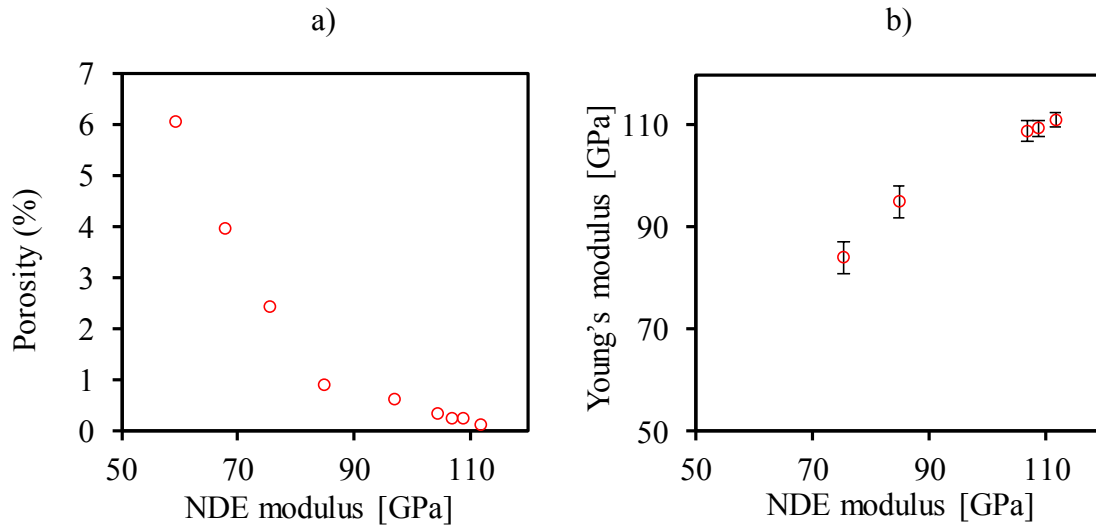


Figure 1.26 Modulus of AM components calculated by NDE in comparison to, a) The Archimedes' porosity (RD), b) the Young's modulus obtained from tensile tests

The tensile test data involves 5 components of Ti-6Al-4V at each process parameter setting thus giving a standard deviation. Further details regarding the mechanical testing can be found in Gong *et al.* [71]. The NDE modulus is estimated from coupons made with the same parameters manufactured within the same AM build. The NDE modulus follows the same trend as the Young's modulus. The components with high porosity have a lower NDE modulus prediction compared to the Young's modulus. The NDE modulus might be more sensitive to larger porosity while it becomes less sensitive as we get closer to fully dense components. The NDE modulus approximates the Young's modulus since the shear velocity in these coupons was not measured and the Poisson's ratio was assumed.

Nevertheless, the trends indicate that ultrasonic NDE can be used for porosity and elastic modulus evaluation and thus has the potential to be used as an in-situ quality NDE tool.

## 1.5 Objectives and Dissertation Format

### 1.5.1 Objectives

- 1) To select a suitable ultrasonic NDE methodology for in-situ continuous monitoring of UAM.
- 2) To design the in-situ monitoring sensor setup and install it in an industrial UAM system.
- 3) To analyze results from in-situ continuous monitoring and identify the information that can be extracted to develop process-structure-property correlations.
- 4) To develop a forward model which simulates the NDE sensor interaction with AM components, and an inversion-model that can estimate bond-quality based on the NDE sensor output.
- 5) To use the NDE results to understand the mechanism of defect formation and evolution in UAM and thus suggest practical process improvements.
- 6) To test the NDE methodology developed on the Laser Powder Bed Fusion process to study defect evolution and to improve the process.
- 7) To use in-situ and post-process NDE as a process parameter development tool for metal Additive Manufacturing.

### 1.5.2 Dissertation format

This dissertation is prepared using a multiple-paper format. Four papers are composed to describe the research results, discussions and conclusions based on the research goals and objectives mentioned from the previous section.

Chapter 2 is a conference paper published in *Proceedings of 44<sup>th</sup> Annual Review of Progress in Quantitative Nondestructive Evaluation* (2018). It explores the considerations to design and install an in-situ monitoring ultrasonic NDE system on an UAM system.

Chapter 3 is a journal paper published in the *NDT & E International* (2018). It demonstrates a model-based inversion methodology for UAM bond quality evaluation.

Chapter 4 is prepared as a journal paper to be submitted to *Journal of Materials Processing Technology*. It explores how monitoring defect evolution in UAM could help understand the process and thus propose practical solutions to improve it. A novel solid-state repair mechanism based on Friction Stir Processing (FSP) was proposed and demonstrated.

Chapter 5 is prepared as a journal paper to be submitted to *Additive Manufacturing*. It investigates the application of ultrasonic NDE to Laser Powder Bed Fusion as a process parameter development tool.

Chapter 6 discusses major conclusions from this work and identified future work. Related materials are contained in the Appendix.

CHAPTER 2  
DESIGNING AN IN-SITU ULTRASONIC NONDESTRUCTIVE EVALUATION  
SYSTEM FOR ULTRASONIC ADDITIVE MANUFACTURING <sup>1</sup>

## 2.1 Introduction

UAM involves joining thin metal tapes using the principles of ultrasonic welding. These tape layers are additively bonded followed by CNC machining to required dimensions. The additive-subtractive nature combined with low heat processing gives UAM unique capabilities such as completely enclosed internal cooling channels, metal-matrix composites, smart parts with embedded sensors, and bonding metallurgically incompatible dissimilar metals [2, 16, 93, 94]. Fig. 2.1a shows a schematic of the UAM bonding process [95]. The set of UAM layers are henceforth referred to as the UAM stack. Bond formation by ultrasonic welding requires two conditions to be fulfilled, (i) the generation of clean surfaces with no barrier layers at the atomic scale and (ii) direct contact between these clean surfaces, which facilitates diffusion and hence a metallurgical bond. Process parameters that affect bond quality in UAM are vibration amplitude, velocity of bonding, and normal force assuming a frequency of 20 kHz. Out of these, the quality is

---

<sup>1</sup> This chapter is a paper published in *Proceedings of 44<sup>th</sup> Annual Progress in Qualitative Nondestructive Evaluation* (2018). All permissions to use this paper as a part of this dissertation are contained in the Appendix.

most sensitive to vibration amplitude. Higher energy density during UAM occurs with higher vibration amplitude, normal force and lower velocity of bonding. Throughout this chapter only the vibration amplitude is varied. Higher vibration amplitude leads to better bond quality until an optimum, after which the excessive vibration induces delamination on already bonded interfaces. One such interface that is prone to debonding is the base/build interface. As shown in Fig. 2.1b, significant delamination is often observed after layer build-up. The reason for this is argued to be due to the vibration of the UAM structure as more layers are built.

With the right combination of input parameters, it is possible to arrive at dense, defect-free UAM components. Since UAM is a contact vibration-based bonding mechanism, the height and shape of the surface on which a new weld is made is important in determining the weld quality. This implies that there is not a single set of ideal parameters for a material—rather the parameters need to gradually change as the layers build up. Having a feedback control mechanism may be the best way to achieve this. Since UAM is a solid-state process during which the average temperatures are close to ambient, ultrasonic NDE is an ideal candidate for a feedback control loop. While designing an in-situ NDE monitoring system, it is important to consider the effect of introduction of the NDE setup on the quality of UAM components.

In this chapter, we explore the iterative design that was utilized to setup a continuous NDE monitoring system on a commercial UAM system. In the next section, offline ultrasonic NDE of a UAM test components is presented. Further, the designs of NDE monitoring setup from above and below the stack are discussed. An in-situ

monitoring setup from below is developed that does not cause a change in UAM component quality as evidenced by mechanical tests.

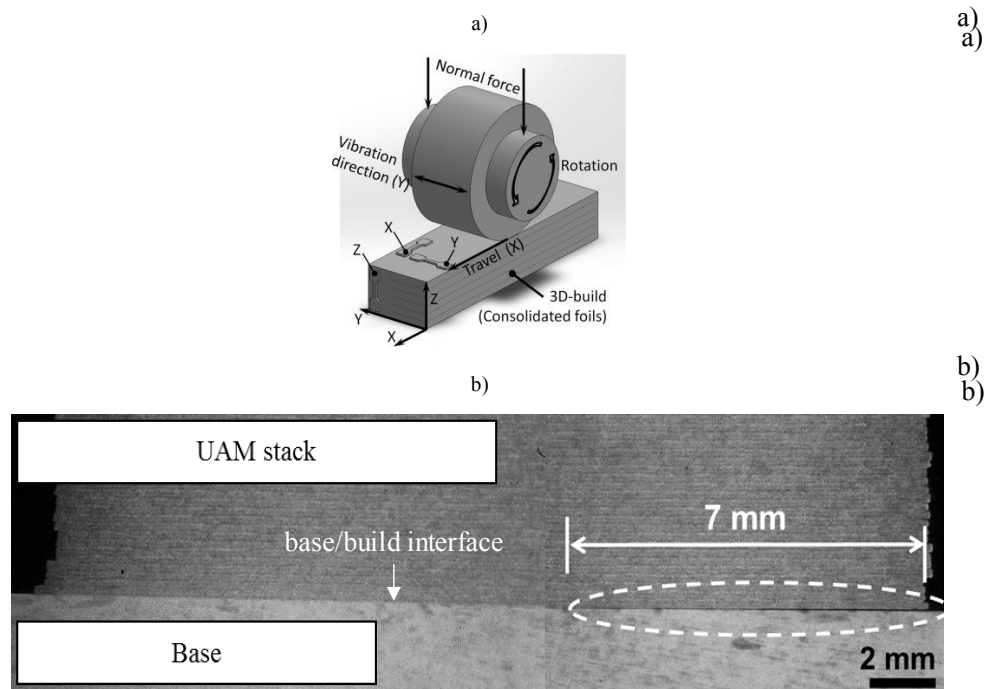


Figure 2.1 a) Schematic of the Ultrasonic Additive Manufacturing process [95]

## 2.2 Offline NDE of UAM Components

Ultrasonic NDE is well suited for in-situ quality monitoring of UAM components due to the low temperature processing and nature of defects. Typical defects in UAM are classified as Type-1 (interlayer defects) and Type-2 (inter track defects). Ultrasonic NDE is well suited to detect delamination and partially bonded regions within a component (Type-1 defects). Type-2 defects are beyond the scope of this work. Test components made of 150  $\mu\text{m}$  foils of Al 6061 measuring 101.6 mm in length, 25 mm in width and 6 mm in height were manufactured with varying vibration amplitudes, normal force of 5000 N, and

bonding velocity of 85 mm/s. The base plate dimensions were 254 mm length, 203.2 mm width and 12 mm height. These test components served as a reference set for this chapter.

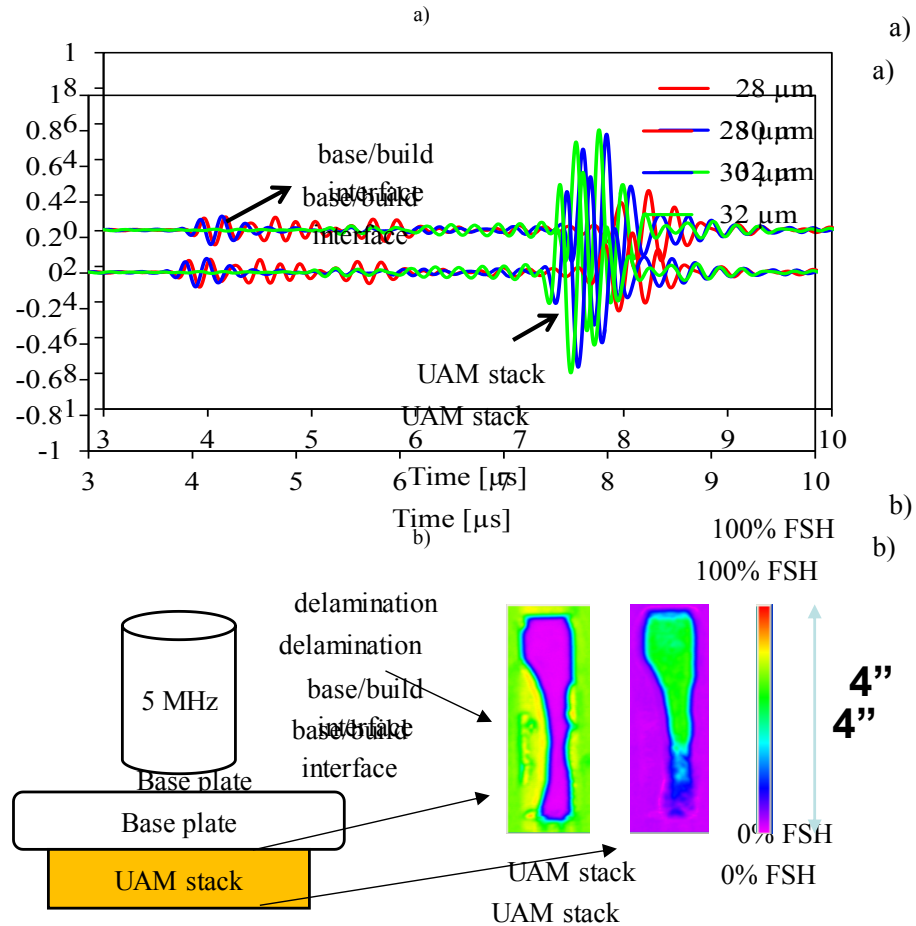


Figure 2.2 . a) A-scan captured at the center of the UAM stack. b) Acoustic microscopy C-scans gated at the base/build interface and top of the UAM stack

The vibration amplitude was changed between 28 and 36 μm to generate components of varying quality. Three components with the same build parameters were manufactured on each base plate separated by 19 mm edge to edge. Ultrasonic C-scans were collected by immersing UAM components into a SONIX acoustic microscopy tank. A-scan at the center of UAM component indicates the two distinct signals of interest, namely the base/build interface and the top of the UAM stack as shown in Fig. 2.2a. A 5

MHz delay line immersion transducer was then used to scan the bottom of the base as shown in Fig. 2.2b. Both these signals can be gated to study the quality of UAM components. The image obtained by gating the base/build interface is henceforth referred to as the reflection image and that obtained by gating the signal from the top of the stack is referred to as the transmission image. The base/build interface is of significance as it is prone to recurring delamination with layer build-up. The signal from the top of the stack represents the average quality of the whole component.

Fig. 2.3 shows the change in reflection image with varying vibration amplitudes and thus varying quality. It can be observed that as the vibration amplitude increases, the base/build delamination appears larger. The delamination starts at the edge of the component and slowly spreads inward. In previous work [96], we have demonstrated that at larger vibration amplitudes the base/build delamination results in failure at a relatively lower number of layers as compared to lower vibration amplitudes. We also observe significant delamination on components built away from the center of the base plate. The delamination initiation zone also seems to be dependent on the vibration characteristics of the base and the location of the component on it. The choice for vibration amplitude can hence be divided into three zones, namely low, optimal and high. At low amplitude, there is not enough energy to create a complete metallurgical bond. At high amplitude, metallurgical bonds formed in earlier paths are prone to delamination subsequently. Fig. 2.3 also shows the change in the transmission image with varying vibration amplitudes. Regions of delamination are clearly indicated in both the reflection and the transmission images. However, the reflection image has a higher contrast value (%FSH) at delamination in comparison to the transmission image. As the vibration amplitude increases, the %FSH



of transmission image improves thus indicating better bonding. Hence, the challenge lies in finding the optimal bonding parameters for a given geometry and material such that a good metallurgical bond is formed while avoiding a base/build delamination.

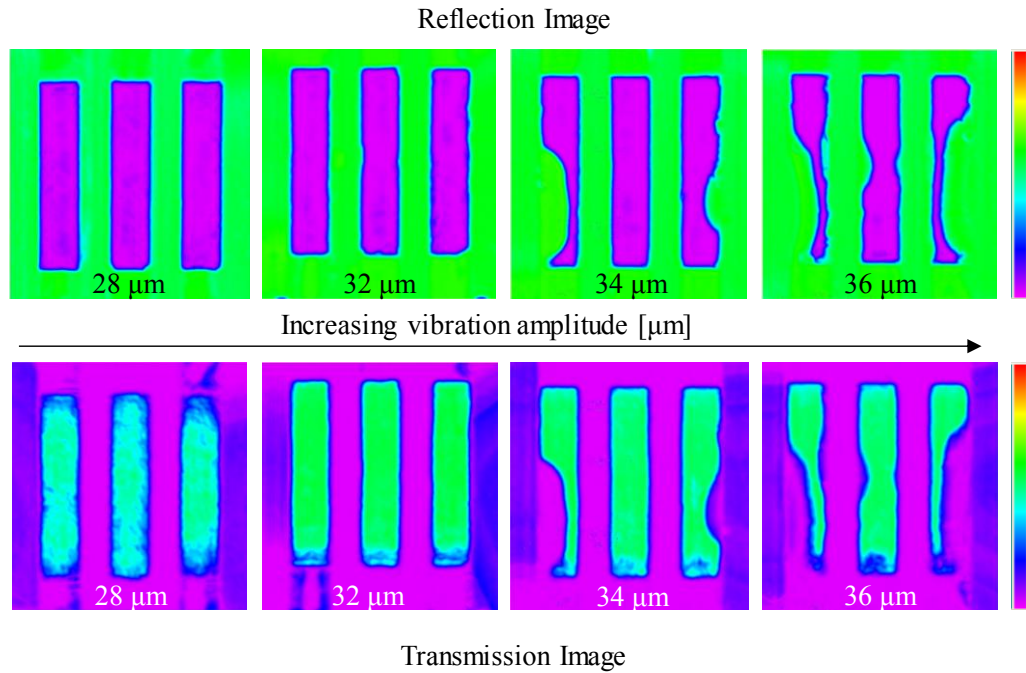


Figure 2.3 Reflection and transmission images captured on UAM components of varying build quality

### 2.3 In-situ NDE Setup

Designing an in-situ ultrasonic monitoring system can be done in two ways. Either the quality can be monitored from above or below. Both these approaches have their advantages and disadvantages, which are discussed below.

### 2.3.1 Monitoring from above the stack

An in-situ monitoring setup was installed behind the weld head to measure the quality of UAM layers after bonding (Fig. 2.4a). After each layer has been bonded, the whole UAM stack along with the base were submerged in isopropyl alcohol, and an immersion transducer was utilized to measure the quality of the UAM stack. Isopropyl was used as a couplant since it does not affect the quality and is easy to clean up between layers. The advantage of in-situ monitoring from above is that the quality of the entire component could be measured and both Type-1 and Type-2 defects could be identified. Another advantage is that the quality of the UAM component is not altered due to the introduction of the NDE monitoring system. However, the disadvantages include a rough top surface that restricts high frequency measurements and an intrusive method of operation that interrupts the UAM process until the measurement is gathered. The surface rms roughness of UAM components ranges from 7-20  $\mu\text{m}$ , which leads to a significant attenuation of the ultrasonic NDE waves going through the component. At 10 MHz inspection, 1  $\mu\text{m}$  rough surface has an attenuation of 10 dB at the front surface [97]. Typically, the UAM process is additive-subtractive and involves using a CNC mill to machine the surfaces to net shape. In such an event, the advantages of monitoring from above outweigh the disadvantages. However, within a commercial UAM system, an intrusive NDE monitoring setup is not practical.

### 2.3.2 Monitoring from below the stack

Another method of in-situ monitoring has been implemented on a Laser Powder Bed Fusion AM system [91] that involves using a contact ultrasonic transducer attached

on the bottom of the base plate that is able to measure how the quality changes with layer build up. A similar approach works with UAM where the base plate is raised by supports and a contact transducer is attached to the bottom of the base. A schematic shown below in Fig. 2.4b illustrates the setup. The primary advantage of this setup is that it is non-intrusive and does not require any changes to the UAM process itself. However, a considerable disadvantage of this setup is that the quality of UAM components might change due to the introduction of supports and the monitoring system itself. Another disadvantage is the point measurement that limits the area of the component inspected. On weighing the pros and cons, it is evident that monitoring from below is the more practical approach, which could give insightful data into the quality of the component as it is being built up.

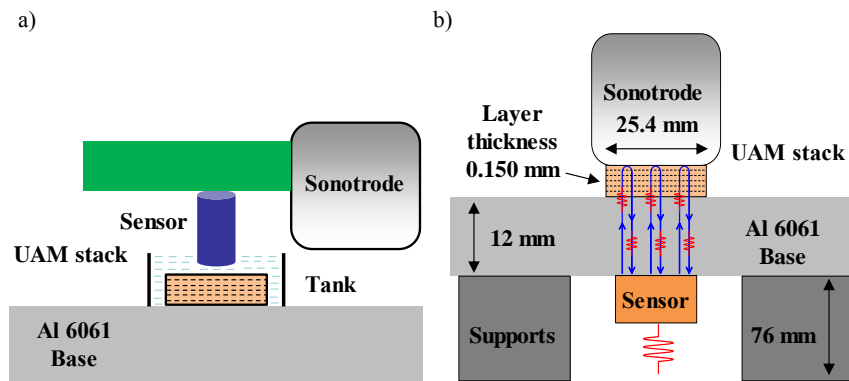


Figure 2.4 a) In-situ monitoring from above. b) In-situ monitoring from below

### 2.3.3 Effect of monitoring system on UAM component quality

It is expected that the introduction of an NDE monitoring system influences UAM component quality as the vibration characteristics of the base are changed. As shown previously in Fig. 2.3, if the location of the component is closer to the edge, it is prone to

delamination. The vibration characteristics of the base certainly affect the quality of the UAM stack. To study the impact of the NDE monitoring system, an experiment was designed with supports in the X and Y directions. A solid block of aluminum with the NDE sensor fully enclosed was used as another test case as shown in Fig. 2.5. The dimensions of the base plate on top were the same as those of the reference specimen presented previously, and UAM components of the same dimensions were built at the center of the plate.

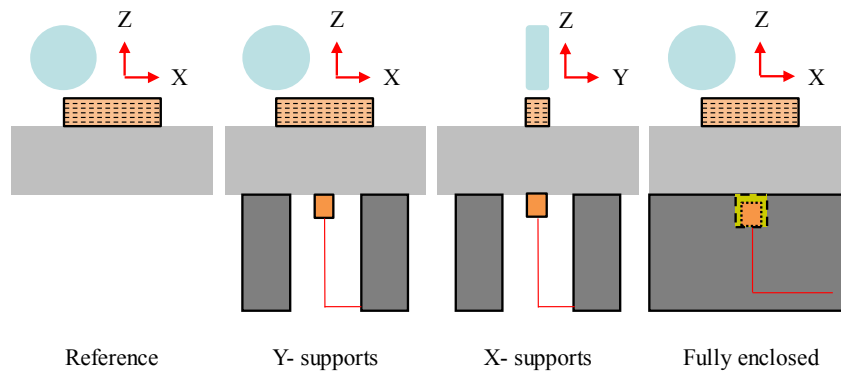


Figure 2.5 Schematic of experiment to test the effect of in-situ NDE monitoring system

Components built in various configurations were immersed in the water tank of a SONIX acoustic microscope, and C-scan images were captured. Reflection and transmission images are presented beside each other in that order for each configuration and amplitude in Fig. 2.6. In the reference components, with increasing vibration amplitude the quality of both reflection and transmission images improve until the component starts delaminating. Supports exclusively along the vibration direction (Y-direction) hinder the vibration of the base so that more energy is transferred to the part itself, leading to early delamination of the base/build interface and failure at higher vibration amplitudes. On the other hand, supports exclusively along the bonding direction (X-direction) lead to less energy transfer to the UAM stack, which leads to lower stack quality for the same vibration

amplitude. The reason for delamination at 30 and 36  $\mu\text{m}$  vibration amplitude in components with X-support is not explained by the same logic, and external factors might be involved in the failure. Thus, as seen in Fig. 2.6, having exclusive X or Y direction supports does not provide an equivalent bond quality as compared to the base line. In contrast, components built in the fully enclosed setup have similar quality in comparison to the reference and also do not fail at larger amplitudes.

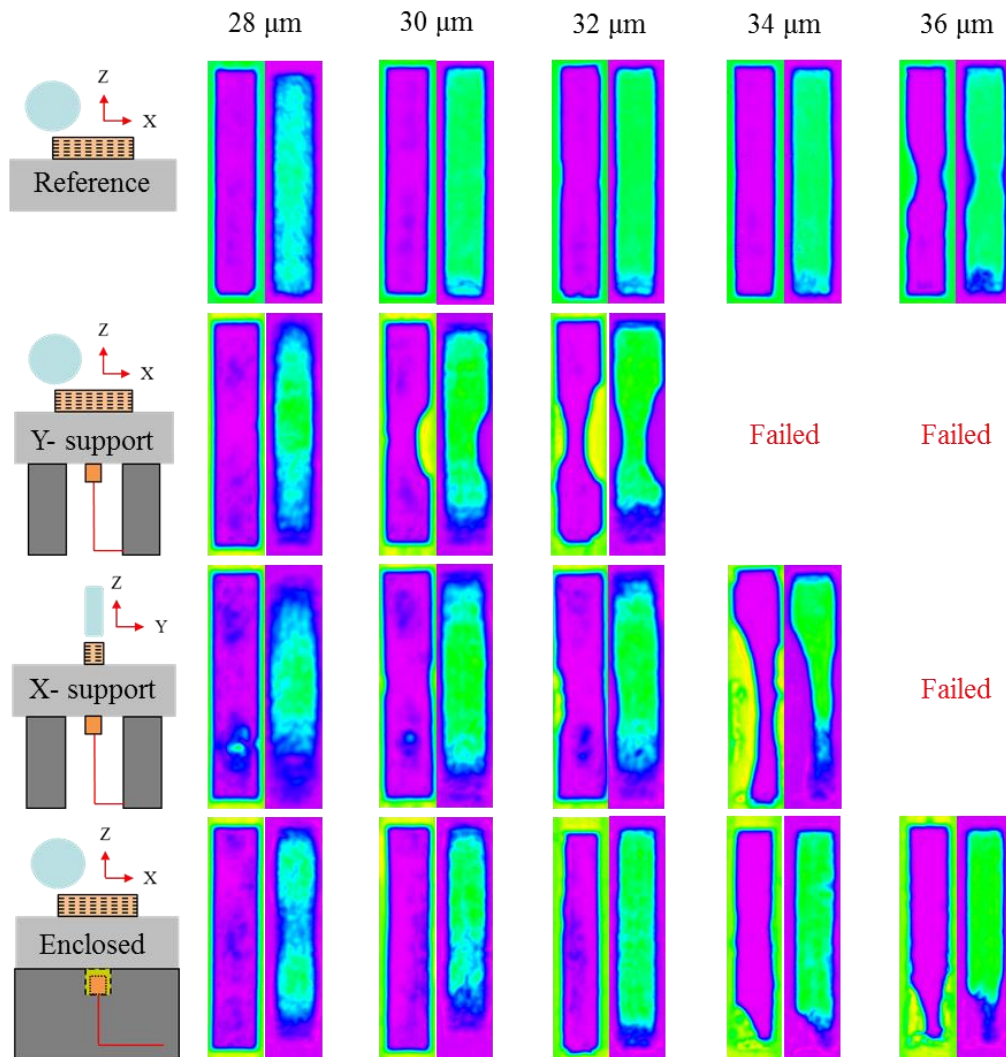


Figure 2.6 C-scan images of components built with various setup configurations

#### 2.3.4 Improved NDE setup and preliminary results

The proposed NDE setup embeds the entire ultrasonic transducer and wiring in a large solid block of aluminum attached with a base plate on top. Thereafter, a UAM stack is bonded layer-by-layer on top of the base plate. The solid block housing the ultrasonic transducer consists of a hole at the center and an oil reservoir in which the transducer is immersed, as shown in Fig. 2.5. The oil provides coupling between the transducer and the base plate so that the quality of the UAM stack can be measured from the bottom of the base plate. Previously [96], contact transducers were experimented with but due to the vibration during UAM, coupling was lost with the base plate during manufacturing. Evaluating the mechanical strength of the UAM components is often performed by push-pin testing [20, 98]. It involves pushing out a set of UAM layers in a three-point bend configuration. Push-pin specimen and test specifications were derived from Wolcott *et al.* 2014 [98]. The mechanical test results are presented for all four configurations, namely: a) base line with no transducer, b) bonding direction supports (X-direction), c) vibration direction supports (Y-direction), and d) fully embedded transducer. Fig. 2.7. shows mechanical test results which indicate that the quality of components built with a fully embedded transducer are comparable to the reference. Components built using the X-support configuration have significantly lower quality for the same vibration amplitude. Components built with Y-support configuration failed at 3 and 36  $\mu\text{m}$  amplitudes, which would be considered as optimal in our reference set. Push-pin test represents the strength of a set of UAM layers and their resistance to delamination. Area under the load-displacement curves of the push-pin test has been used along with the slope and maximum load values to characterize UAM components. Table 2.1 indicates the area under the load-

displacement curves and shows that the fully enclosed set of components behave similarly to that of the reference set with a small but consistent reduction in quality. This is expected because the larger structure below would absorb part of the vibration that was intended to go to the UAM components.

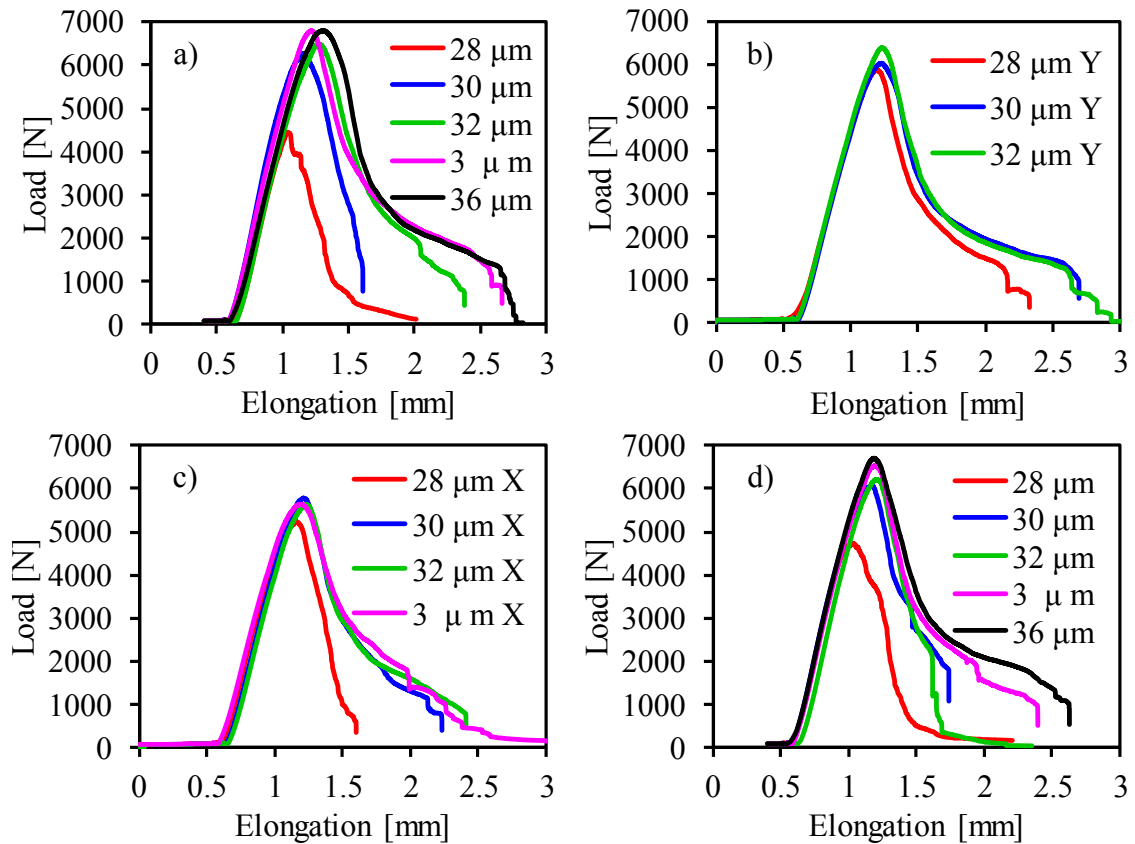


Figure 2.7 Push-pin test results for four configurations: a) reference, b) vibration direction (Y- supports), c) bonding direction (X- supports), and d) fully enclosed

Preliminary results are presented from an in-situ monitoring experiment performed on a commercial Fabrisonics R7200 UAM system. A 10 MHz immersion transducer was used on a UA stack comprised of thirty layers of 150 μm Al 6061 foils. The continuous monitoring system utilizes a pulse repetition frequency of 2000 Hz. With the addition of each layer, the signal from the top of the stack shifts to the right as it takes a longer time to travel through a thicker stack as shown in Fig. 2.8a. The time of flight (TOF) of a gated

windowed stack signal is studied at peak energy after Hilbert transformation. TOF is calculated before, during and after bonding each layer. Fig. 2.8b shows a sharp change in the TOF during bonding. It is reasoned that during welding, the TOF jumps and recovers due to the brief presence of the weld head right on top of the stack. This jump can thus be used as an indicator of the moment of bonding. Signals between layers can thus be used to monitor layer-by-layer ultrasonic NDE information regarding quality of the UAM stack. Velocity and attenuation can be studied along with backscatter to determine the quality of the UAM components. The base/build interface can also be studied simultaneously to provide indication of delamination.

Table 2.1 Area under load-displacement curves in kN-mm from push-pin tests

<b>Vibration amplitude [μm]</b>	<b>Reference [kN-mm]</b>	<b>Y-supports [kN-mm]</b>	<b>X-supports [kN-mm]</b>	<b>Fully enclosed [kN-mm]</b>
28	2.21	4.67	2.92	1.55
30	3.88	5.78	4.36	4.04
32	5.48	6.01	4.56	3.80
34	6.50	failed	5.18	5.39
36	6.75	failed	failed	6.26



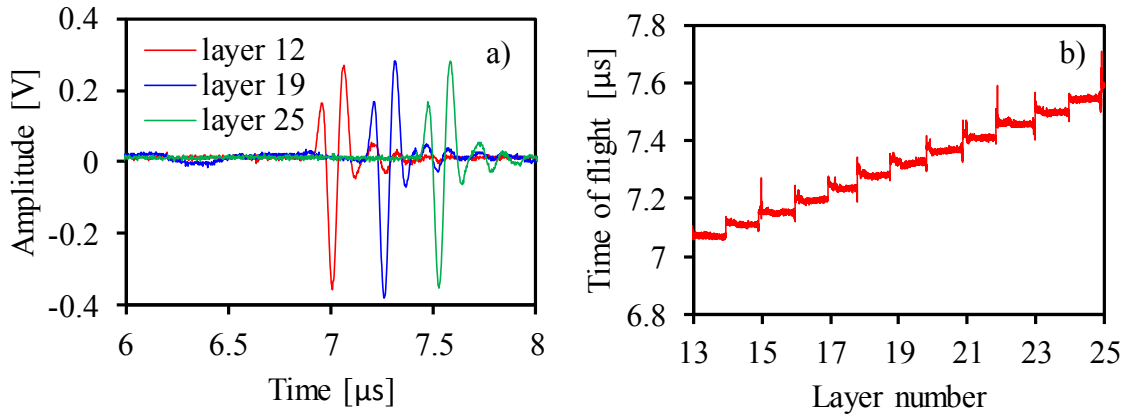


Figure 2.8 a) A-scans collected after bonding number of layers

## 2.4 Conclusions and Future Work

Ultrasonic NDE has the potential to detect typical defects observed in UAM components as evidenced through offline NDE results. One such defect of interest is the base/build interface delamination that is dependent on UAM component geometry, base plate geometry and even the location on base plate. Ultrasonic NDE is also a good tool to measure average quality along the direction of layer build up, which is the direction having the lowest modulus within a UAM component. In-situ ultrasonic NDE can be used to quantify the bond quality of each layer including the base/build interface. Two possible approaches of in-situ monitoring were proposed and tested, one from above the UAM stack and the other from below the base plate. While monitoring from above has its advantages, it is not the most practical method since it involves stopping the manufacturing process to take a measurement. Monitoring from below, on the other hand, is a practical approach that can be used for continuous online quality monitoring. The primary challenge lies in ensuring that the addition of the in-situ monitoring system does not alter the quality of UAM components. Supports are required to raise the base plate to accommodate the in-

situ monitoring system. Supports along the bonding and vibration directions were tested and it was found that raising the base plate alters the quality of UAM components as compared to the reference. Thus, a new set up was implemented wherein the ultrasonic NDE sensor is entirely embedded in a large solid block of aluminum. The ultrasonic transducer was also changed from contact to immersion mode to have stable continuous monitoring even during manufacturing. Through mechanical testing, it was shown that the quality of UAM components built on this set up was comparable to that of base line components built with no transducer beneath them. The preliminary results from continuous monitoring indicated a stark contrast in TOF measurements during the moment of bonding. This phenomenon is due to the weld head passing over the top of the UAM stack with a large normal force. TOF change can thus be utilized as an indication of bonding and helps demarcate the interval between layers. The average of signals within the interval is an A-scan representation measured at the center of the UAM component. Phase velocity, group velocity, attenuation, and backscatter can thus be calculated after bonding each new layer. In the future, modulation of signals from within the UAM component, such as the base/build interface, can be studied during bonding. Furthermore, defects that are identified by in-situ monitoring can potentially be repaired by milling off defective regions and rebuilding them. Ultrasonic NDE can thus be utilized for online qualification, closed-loop-control and offline certification of UAM components.

CHAPTER 3  
IN-SITU INTERFACIAL QUALITY ASSESSMENT OF ULTRASONIC ADDITIVE  
MANUFACTURING COMPONENTS USING ULTRASONIC NONDESTRUCTIVE  
EVALUATION <sup>2</sup>

### 3.1 Introduction

Metal UAM is a layer-by-layer metal-based solid-state bonding process which is commonly used in conjunction with a Computer Numerical Control (CNC) mill. In this process, ultrasonic energy is utilized to create solid-state metallurgical bonding between a thin foil and an existing flat substrate. CNC machining after depositing each layer is performed to achieve required shapes and dimensions, enabling a freeform fabrication. The additive-subtractive nature and the low-heat solid-state processing give the UAM process certain unique capabilities such as completely enclosed internal cooling channels, smart parts with embedded sensors, metal-matrix composites, and bonding metallurgically incompatible dissimilar metals [2, 93]. UAM involves high-speed scrubbing between foils to be joined. Several researchers have studied the mechanism of bonding both experimentally as well as through simulation [16, 23, 94]. The bonding process is a function of the three principal input parameters; force applied, velocity of bonding, and

---

<sup>2</sup> This chapter is a paper published in *NDT & E International* (2018). All permissions to use this paper as a part of this dissertation are contained in the Appendix.

vibration amplitude. It has been shown to be dependent on surface roughness, temperature, base plate characteristics, part geometry, and build height [6, 21, 27] among other factors. Traditionally, UAM utilized an ultrasonic welder of 20 kHz frequency with maximum power limit of 3 kW. Recent integration of higher power (up to 9 kW) ultrasonic welders gave UAM the capability to weld more materials [6].

Bond formation by ultrasonic welding requires two conditions to be fulfilled, (i) the generation of clean surfaces with no barrier layers at the atomic scale and (ii) a direct contact between these clean surfaces which facilitates diffusion and hence a metallurgical bond. Electron Backscatter Diffraction (EBSD) studies [16, 23] have shown that between any two foils the microstructure can be divided into upper bulk region, fine grained interface region, and lower bulk region. The most common defects in UAM components are classified as Type-1 defects which are delaminations between layers and Type-2 defects which form between adjacent tracks that are out of the scope of this study. Type-1 defects that can be seen via optical microscopy are gross delaminations and indicate process parameters which are far away from optimal that would never be used in a typical industrial setting.

Process parameter optimization within UAM has typically been performed experimentally by varying the three input parameters until a satisfactory bond quality was achieved according to the metric of Linear Weld Density (% of area that appears to be fully bonded via optical microscopy). Some researchers [16] have found that %LWD is not a good measure of the bond strength since it does not consider kissing bonds or tightly closed regions. A better qualitative mechanism was suggested [94] based on a pull out tensile test followed by measurement of the fractured surface to analyze the % bonded region. It was

argued that there is a definite presence of tightly closed surfaces in UAM that cannot be observed with an optical microscope, since only after tensile testing will these kissing bonds be visible. It was further explored how there could be what appears to be complete metallurgical bonding but on pull out tensile tests along the build direction the measured UTS could be as low as 15% that of a solid wrought material [94]. The reasoning for the same was argued to be the presence of micro-voids that form upon the application of a small amount of stress. These voids predominantly occur at the interface and coalesce into cracks leading to brittle fracture. Within the literature on bond strength measurement in UAM, mechanical tests involved using lap shear, push-pin, and tensile tests [20, 26, 27]. It is of primary interest to be able to identify those imperfect interfaces which are often invisible even to a high-magnification optical microscope. UAM aluminum components are essentially transversely isotropic due to the interface imperfections between the layers. The strength along the other two directions was shown to be roughly equal to around 80% the UTS of wrought material [94]. The quality of bonding at each interface determines the overall component stiffness. Since UAM was developed for producing end-use functional parts, it is beneficial to monitor the process online to enable closed loop control of the process. While the strength of UAM components depends on the weakest interface where failure occurs, it is beneficial to monitor the stiffness of each layer.

The existing online monitoring literature on UAM is primarily based on temperature measurement [22]. Usually, an infrared (IR) camera is used to observe the temperature of the just bonded foil during welding. The weld energy is calculated as a function of the rise in temperature and correlated to the peel strength of the welds. Another method to monitor temperature is to embed a K-type thermocouple between two UAM

layers and bond on top of the same. A truly online monitoring approach has been demonstrated with a photonic Doppler velocimeter measuring the phase and velocity of the sonotrode, foil, and base [28]. This method has shown some promise in characterizing the contrast between a good weld and a poor one but monitors only the just bonded foil. Online in-situ monitoring of layer-by-layer manufacturing processes offers a unique advantage which is to adjust the build parameters in real time to achieve closed loop process control. Most fusion based AM processes form defects in the top few layers from the solidification zone and hence monitoring the top surface is critical, leading to the use of optical techniques such as IR imaging. But in the case of UAM parts, a layer might be fully bonded initially but can form a delamination due to repeated cyclic loading several layers after it has been bonded. This makes it crucial to have a monitoring process that goes through the component. This, coupled with the lower temperatures in UAM, makes it an attractive candidate for ultrasonic NDE.

Micro-voids, kissing bonds, and tightly closed interfaces produced by the UAM process can be treated as interface imperfections. In a seminal paper, Baik and Thompson described how the interaction of ultrasonic waves with an imperfect interface could be modeled as a spring-mass system when the wavelength of ultrasound was large in comparison to the size of the interface [38]. Nagy showed how imperfect interfaces in similar and dissimilar inertial and friction welds could be characterized by ultrasound and introduced a method to differentiate between different kinds of imperfect interfaces like slip bonds, kissing bonds, and partial bonds based on their different normal-to-transverse interfacial stiffness ratios [39, 40]. Several researchers have shown ultrasonic techniques to be effective in classifying adhesive, diffusion and friction welded bonds [42, 43]. UAM

components consist of a layered structure with several imperfect interfaces and each interface is like diffusion bonded/friction welded interface. Hence, ultrasonic methods are naturally the first choice as a potential NDE technique. There exist several efforts on using NDE techniques to certify Additively Manufactured components [99, 100]. Many of them are aimed towards powder bed fusion processes, and present different kinds of defects and interface imperfections compared to UAM [101]. A similar NDE sensor setup has been developed by Reider *et al.* for the laser melting AM process [91, 102].

The current study is aimed at developing a robust, sensitive ultrasonic NDE technique that can be used for bond quality inversion of UAM components. For this purpose, the most sensitive technological parameter, the vibration amplitude is varied, and the quality of the resulting components is studied. In Sec. 3.2 preliminary results from an in-situ online monitoring study are presented, followed by the results of a qualitative offline NDE test conducted on a set of UAM components and a discussion of the effects of having an NDE sensor during UAM component fabrication [96]. Sec. 3.3 discusses modeling of a layered UAM component as a base plus stack (set of layered interfaces) such that each interface between layers is modeled as a distributed spring. An analytical model for wave propagation through UAM components is developed and verified through finite element simulations in COMSOL. Further, due to the repeating nature of the system a Floquet wave homogenization model is developed for phase velocity and impedance prediction. It is shown that at least two independent variables, namely base/build interfacial stiffness ( $\eta_1$ ) and average stack interfacial stiffness ( $\eta$ ), are necessary to represent wave propagation through UAM components. Sec. 3.4 presents an inversion algorithm determining interfacial stiffnesses  $\eta_1$  and  $\eta$  from the measured ultrasonic signals. Correlation between

experimentally measured mechanical strength versus ultrasonic velocity is established and the sensitivity of the inversion model is studied. Three components with varying quality were tested using the in-situ monitoring setup to demonstrate layer-by-layer inversion of bond quality. Finally, in Sec. 3.5 conclusions are drawn from the obtained results and directions for future work are suggested.

### 3.2 Experiment

Fig. 3.1 shows an in-situ monitoring setup that was designed to be used during the UAM process. The base plate has been lifted by supports to accommodate an ultrasonic transducer that is in contact with the base plate using high-temperature grease as couplant. 150  $\mu\text{m}$  layers of annealed and heat-treated aluminum alloy Al 6061 H18 are bonded directly on top of the Al 6061 T6 base plate. It is important to keep in mind industrial applicability while designing a monitoring system that can be used during processing real components. Several challenges were faced as the design was iterated and changed from monitoring from above to monitoring from below the base plate. Choosing an appropriate coupling medium was important along with the choice of having a thin layer vs. larger volume of couplant. The adverse effects of introducing a transducer below the base plate on stack quality have been studied though not presented in this work. Being aware of all these parameters, the design was iterated to what is shown in Fig. 3.1. The dimensions of base plate, transducer, supports and the UAM layers are indicated in the figure. To nondestructively evaluate UAM parts it is necessary to build a set of components with varying qualities and study the sensitivity of quality assessment. Of the three principal technological parameters of the UAM process (weld force, weld speed, and vibration



amplitude), it is well known that build quality is most sensitive to vibration amplitude variations. A preliminary study was performed on a manual Fabrisonics R200 research system on which the in-situ monitoring setup was installed such that ultrasonic data is collected after bonding each layer. Six vibration amplitudes ranging from 25 to 35  $\mu\text{m}$  were used to build 45 layers at a weld force of 5000 N and weld speed of 70 mm/s.

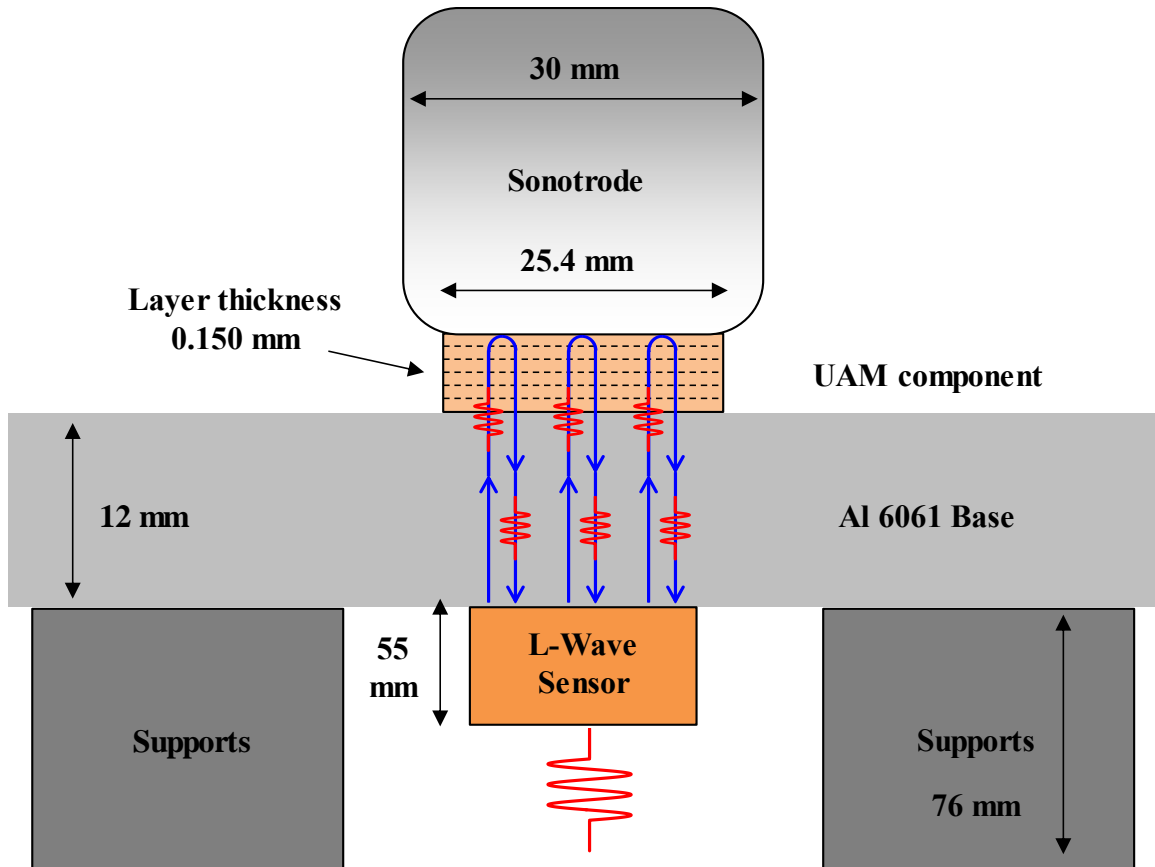


Figure 3.1 In-situ monitoring of the UAM process with access from below

A broadband longitudinal contact transducer of 5 MHz nominal frequency was driven using a JSR Ultrasonics DPR 500 remote pulser/receiver module. The data acquired was sent into a 1.5 GHz 14-bit Acquisition Logic PCI digitizer for processing. A 500 V pulse was used to drive the transducer with a damping of 50  $\Omega$  at a pulse repetition frequency of 200 Hz. 16 such waveforms are collected and averaged to produce a single

point A-scan after bonding of each layer. 16 waveforms were used for each point A-scan to increase SNR. The processed raw data was then exported to and analyzed in MATLAB. The average group delay due to adding each new layer was calculated with respect to the reference captured on the base only (zero layers). Thus, the group delay calculated after bonding  $j$  layers is due to all the layers from 1 to  $j$ . The total thickness of the UAM build is measured using digital calipers and thus the average layer thickness is calculated. This coupled with the group delay is used to calculate the average group velocity after bonding each layer which is shown in Fig. 3.2. Here the group velocity at layer  $j$  refers to the average velocity of ultrasound through layers 1 to  $j$  of the UAM component. When the signal strength drops below a threshold, the data is not plotted in the figure. The most striking feature that can be observed is that, after bonding the first two layers, the measured group velocity drastically reduces and then recovers as more layers are added. Another feature that stands out as new layers are added, is the velocity change which is not strictly monotonic and seems to jump up and down. It is conjectured that both these effects can be attributed to the interference of waves reflected from within the layered component to those reflected from the top of the stack. After bonding  $j$  layers, the strongest ultrasonic signal is the one reflected from the top of the  $j^{\text{th}}$  layer, but there could be several weaker signals which are reflected from layers 1 to  $j-1$ . Depending on the time delay between the strong signal and each weaker signal, there could be a constructive or destructive interference. This interference is expected to change both the amplitude and the velocity of the combined wave.

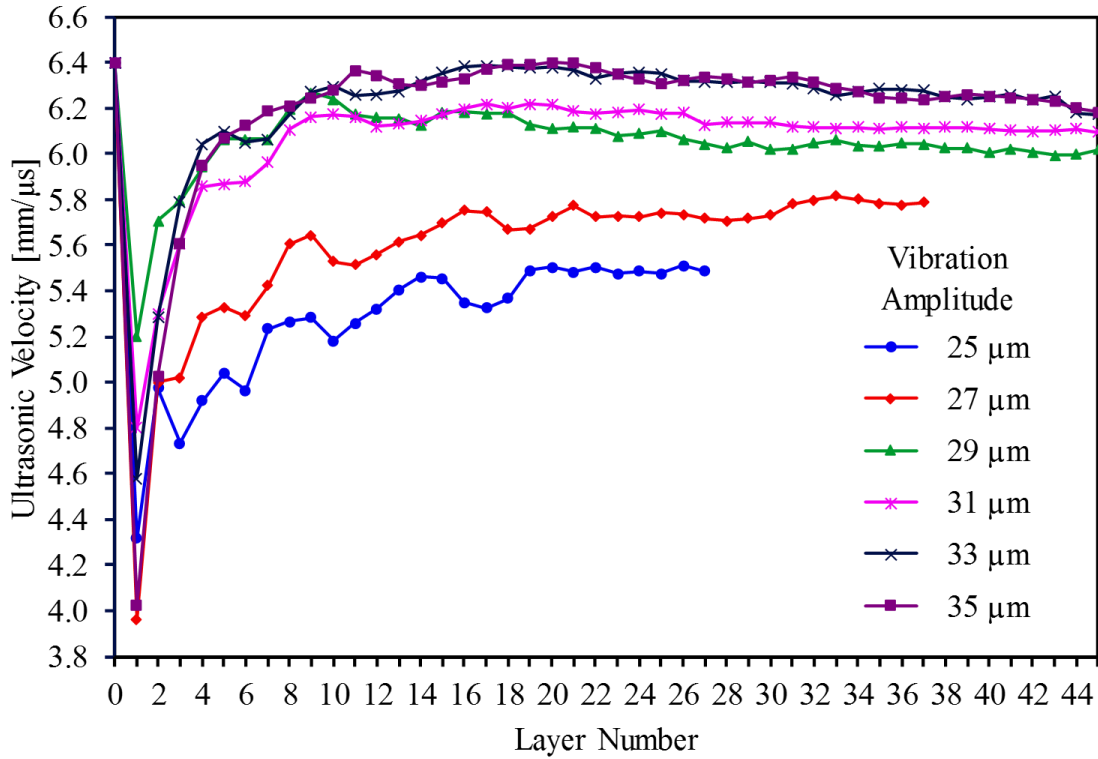


Figure 3.2 Average group velocity measured after bonding each layer

A decreasing trend was observed in the ultrasonic velocity after the initial recovery in the builds made at higher vibration amplitudes, which could be attributed to the increasing compliance of the UAM stack leading to lower transfer of power during welding [103]. It was also observed that the difference between components can be broadly distinguished through ultrasonic velocity. To correlate the nondestructive results to mechanical strength, a push-pin test was performed. Dimensions for the push-pin test are discussed in [20] and the test was performed on a universal tensile testing machine with a three-point bend chuck. The specimens used in this test were of 45 layers in thickness and the top 15 layers were pushed out. The area under the load-displacement curve until failure is the mechanical work required to push through a set of UAM layers. Fig. 3.3a shows the correlation between ultrasonic velocity and vibration amplitude. Fig. 3.3b shows the

correlation between mechanical work and vibration amplitude. While these correlations show that average ultrasonic velocity is a potential indicator of build quality, the features observed from the in-situ monitoring preliminary study need to be further explained. Industrial applicability of this method is of significance since the goal of this research is to develop an in-situ monitoring system. The fact that the ultrasonic transducer is below the base plate makes it an attractive candidate for not disturbing the manufacturing process. The limitation of course is that when there are more complex shaped components, there will be reflections from the geometry rather than from defects.

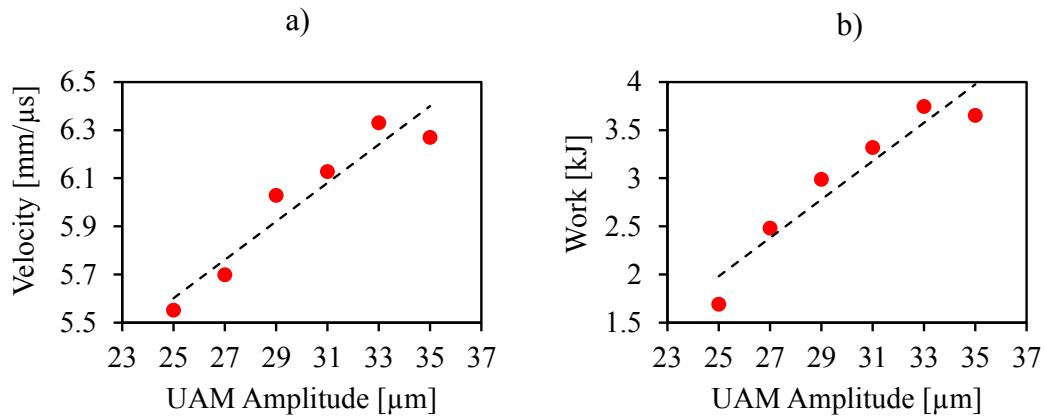


Figure 3.3 a) Variation of ultrasonic group velocity with build amplitude after 45 layers, b) mechanical work performed on pushing out 15 UAM layers and its variation with build amplitude

To measure the diffraction loss through the intact material, a reference block consisting of 7 steps was made with the lowest thickness equal to that of the base plate and the highest thickness larger than 80 UAM layers. Using the same transducer, the frequency amplitude spectrum was measured at different step thicknesses and a linear interpolation was found to be a good approximation of the diffraction loss at any given thickness. Thus, the appropriate reference spectrum was calculated for a given thickness of UAM stack plus

base. Fig. 3.4a shows the average layer thickness measured after bonding 80 layers across 15 samples and shows a significant decrease as the vibration amplitude increases. This is expected since larger vibration amplitudes at the same force lead to more plastic flow and hence smaller thickness after consolidation. Fig. 3.4b shows the average ultrasonic group velocity calculated across the 15 samples. As expected, the ultrasonic velocity increases with vibration amplitude and the standard deviation across three samples is higher for lower quality components.

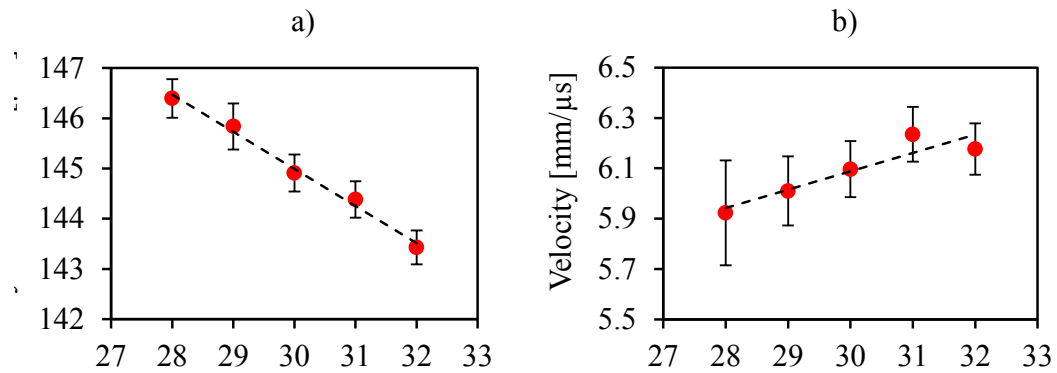


Figure 3.4 a) Average layer thickness, b) ultrasonic group velocity with varying UAM vibration amplitudes

Preliminary experiments presented in (Sec. 1.4) showed the method to capture ultrasonic A-scan response on UAM components. The measured waveforms were gated and windowed at two locations namely the base/build interface and at the top of the UAM stack. To effectively gate the signals of interest, the Hilbert transform of the waveform was used to find the approximate center of the pulse. Instead of using a tapered window function, the gate was initially chosen to be 5 cycles long on either side of the center and subsequently the end position of the gate was chosen by moving it to the very next zero crossing on either side. A rectangular window was used, and the resulting waveform

padded on either side to reach a total number of sample points equal to a chosen power of two for application of the fast Fourier transform. The padded waveform was then cut at the center and the first half placed at the end of the second half to ensure that the variation of the phase spectrum over the frequency range of interest is minimal. The resulting waveform was then fast Fourier transformed and the frequency amplitude and phase spectrum are calculated. By comparing the frequency amplitude spectrum taken at a given thickness to the reference spectrum, it is possible to estimate the attenuation coefficient. By comparing the phase shift with respect to the reference, the phase velocity is estimated. It is important to note that the attenuation coefficient thus calculated includes the stack coupled with the base/build interface and the base as compared to a solid material of the total thickness. It does not thus represent the stack attenuation exactly. Rather, it is an average of the stack attenuation coupled with the base/build attenuation. Fig. 3.5a and 3.5b show the frequency amplitude and attenuation coefficient spectra respectively, for various vibration amplitudes. The reduced transmission due to the presence of the base/build interface thus impacts the attenuation coefficient observed in Fig. 3.5b. From the reference spectrum, it was observed that the center frequency is closer to 4.5 MHz with the 6 dB cut-off frequencies found at around 3.5 and 5.5 MHz, which indicates that the bandwidth of the transducer is approximately 2 MHz. Within the lower quality components, the frequency amplitude spectrum drops down at higher frequencies. Fig. 3.5c shows the phase velocity that appears flat but, in some cases, has a small frequency dependent modulation. At the center frequency, the average phase velocity is sensitive to changes in build quality. The reduction in phase velocity and the drop in the frequency amplitude spectrum within lower quality components is indicative of the fact that the interfaces between layers are imperfect and

the higher the level of imperfection, the stronger this effect gets as the number of layers increases. The fact that the higher frequencies are affected more than the lower frequencies indicates that each interfacial layer acts like a low-pass filter. To explain the experimentally observed phenomenon, it is necessary to model wave propagation in a layered structure with imperfect interfaces between neighboring layers.

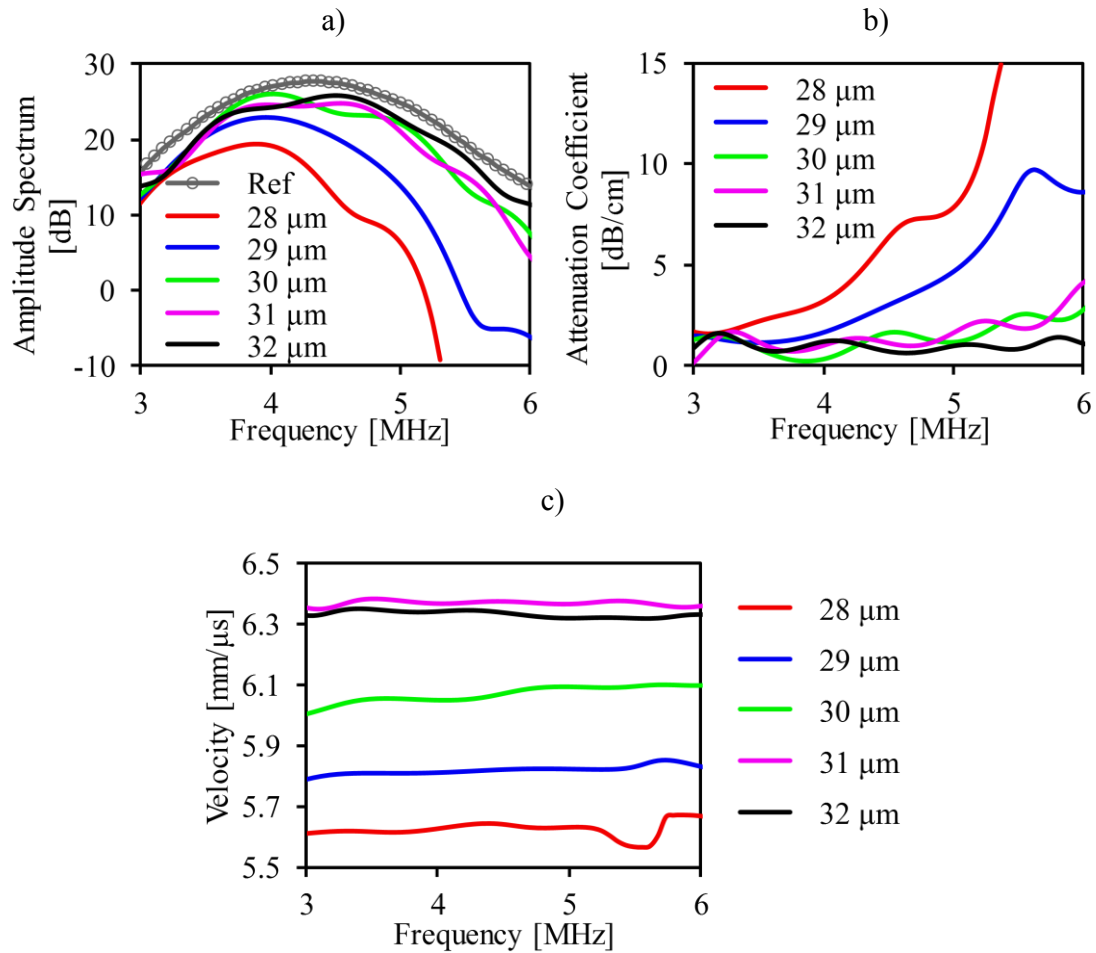


Figure 3.5 Variation of ultrasonic parameters with UAM vibration amplitude: a) frequency amplitude spectrum, b) attenuation coefficient, and c) phase velocity

### 3.3 Finite Interfacial Stiffness Model

When a tensile load is applied to an elastic solid with an imperfect interface containing cracks or voids, the far field displacement that would occur in the absence of the imperfect interface will be increased by localized deformations. This extra extension can be modeled as the response of two half-spaces connected by a layer of distributed springs. The spring stiffness per unit area, the so-called interfacial stiffness, is a function of the topography of the partially contacting surfaces [40]. If the ultrasonic wavelength is large with respect to the contact separation at the interface, a set of modified boundary conditions involving the normal interfacial stiffness  $K$  has been found to correctly predict the frequency dependence of reflection and transmission. A 1D finite interfacial stiffness model has proved to be a very useful tool in ultrasonic modeling of partially bonded/contacting interfaces. A UAM component consists of a base plate followed by  $N$  layers. The base/build interface is the first interface between the base and the very first layer. Then, there are  $N$  asymmetric units each consisting of an imperfect interface followed by a layer of thickness  $d$  as shown in Fig. 3.6a. The ultrasonic parameters of a single foil have been measured to be around 6370 m/s which is very close to that of Al 6061- H18 base material. Even high-quality UAM components exhibit detectable elastic anisotropy with transverse isotropy in the plane normal to the build direction. Interface imperfections between the layers can be most conveniently characterized by measuring the longitudinal ultrasonic wave velocity along the build direction. Hence the normal stiffness in the direction of build height is critical that can be measured ultrasonically by inspecting from below.



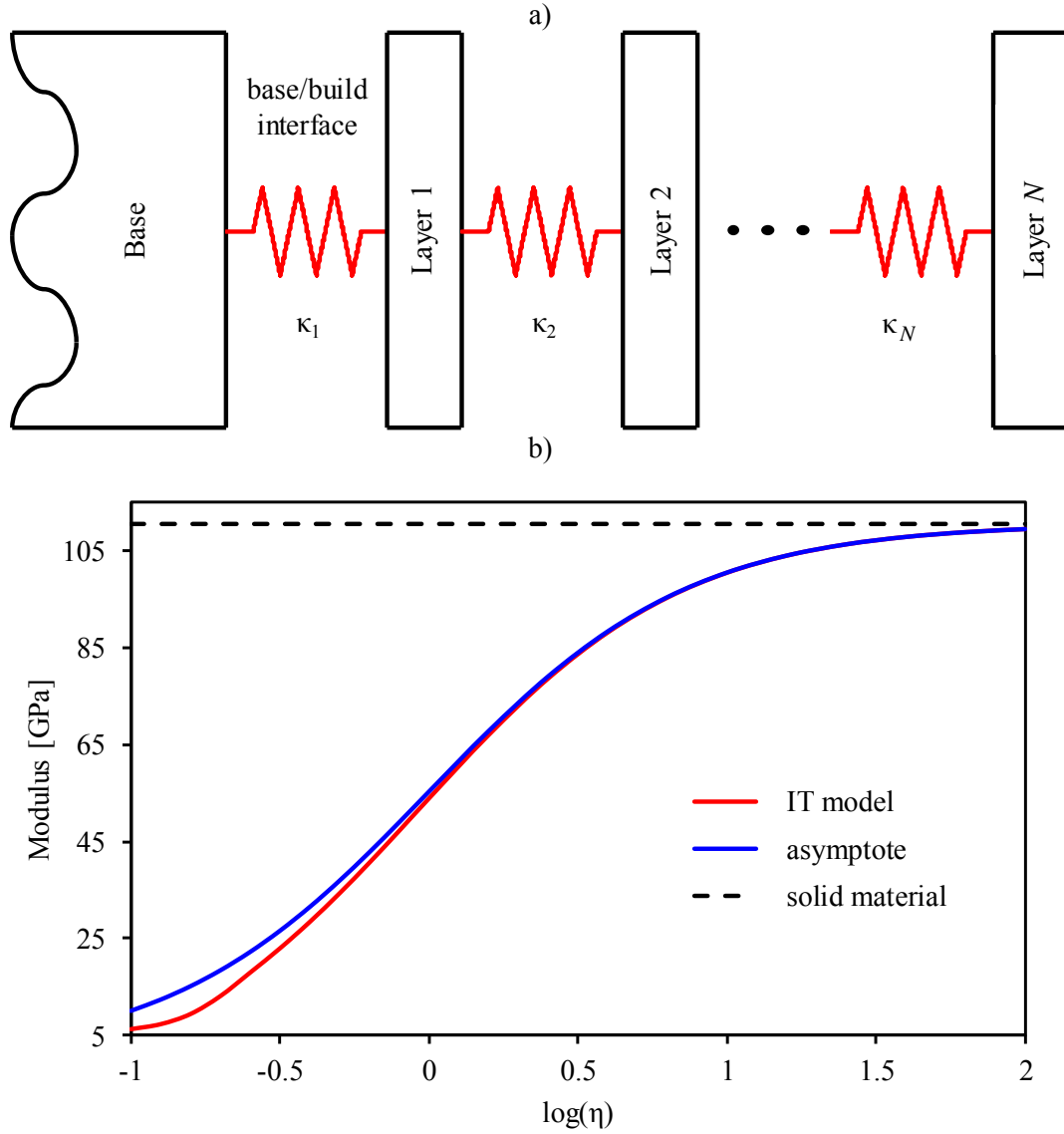


Figure 3.6 a) Schematic of layered UAM structure with interfacial springs, b) the longitudinal elastic modulus of a homogeneous structure with imperfect interfacial springs with coefficient  $\eta$  (the IT model represents  $N = 50$  layers)

The dimensionless parameter  $\eta$  characterizes the level of imperfection known as the normalized interfacial stiffness coefficient.

$$\eta = \frac{\kappa d}{\rho c_0^2}, \quad (3.1)$$

where  $\rho$  is the material density and  $c_0$  is the longitudinal velocity in the intact material. For the purposes of this chapter we are working with Al 6061 T6 alloy and we use  $\rho = 2700$  kg/m<sup>3</sup> and  $c_0 = 6400$  m/s. The interface is considered to have negligible mass. When there are no imperfections then  $\eta = \infty$  which is in fact the boundary condition for a completely rigid interface. Any finite value of  $\eta$  is an indication of the presence of an imperfect interface. The stiffness coefficient  $\eta$  can be complex valued depending on the damping factor included in the spring stiffness  $\kappa$ . As observed in Fig. 3.5, the attenuation through a set of UAM layers can be significant at lower build vibration amplitudes. There is experimental evidence suggesting that the attenuation is primarily caused by defects at the interface. Thus, the spring stiffness can be defined as a complex value to model both the change in phase as well as the attenuation at each interface. This is necessary because otherwise the homogenized finite interfacial stiffness model cannot account for scattering induced and other losses.

### 3.3.1 Impedance translation model

Rayleigh developed an impedance translation (IT) theorem for homogeneous fluid layers which can be adapted to longitudinal wave propagation through a layered elastic solid at normal incidence. The impedance translation theorem relates the specific acoustic impedance at one side of a layer to that at the other. In this manner, one may apply the theorem as many times as necessary to compute the specific acoustic impedance at any interface in a layered media. This approach resembles the classical acoustic Transmission Line Model (TLM) discussed by Kino [104] that is well suited to model acoustic waveguides and is applicable for UAM components as well. These methods enable the

modeling of wave propagation through a layered medium by translating the impedances across each layer of the system [105, 106]. It provides a methodology to calculate the input impedance and the reflection coefficient upon application of a loading impedance on a layered structure. The UAM component can be divided into a set of repeating units each having a layer of intact material with thickness  $d$  and an imperfect interface with a finite interfacial stiffness  $\kappa$ .

Let us denote the input and loading impedances of the  $j^{\text{th}}$  unit by  $Z_j^{\text{input}}$  and  $Z_j^{\text{load}}$ , respectively. Then, according to the impedance translation theorem, the input impedance of the intact layer in the  $j^{\text{th}}$  unit is

$$Z_j^{\text{layer}} = Z_0 \frac{Z_j^{\text{load}} \cosh(-ik_0d) + Z_0 \sinh(-ik_0d)}{Z_0 \cosh(-ik_0d) + Z_j^{\text{load}} \sinh(-ik_0d)}, \quad (3.2)$$

where  $Z_0 = \rho c_0$  and  $k_0 = \omega / c_0$  are the acoustic impedance and wave number in the intact layer, respectively. The input impedance  $Z_j^{\text{input}}$  of the  $j^{\text{th}}$  unit is calculated by accounting for the added compliance of the  $j^{\text{th}}$  imperfect interface

$$Z_{j-1}^{\text{load}} = Z_j^{\text{input}} = \frac{1}{\frac{1}{Z_j^{\text{layer}}} + \frac{i\omega}{\kappa_j}}, \quad (3.3)$$

where  $\kappa_j$  is the interfacial stiffness between the  $j^{\text{th}}$  and  $(j-1)^{\text{th}}$  layers. Since the end of the stack is assumed to be free, the iteration starts with  $Z_N^{\text{load}} = 0$  and iterates through  $j = N, N-1, \dots, 1$  using Eqs. (3.2) and (3.3). Finally, the reflection coefficient of the interface between the base and the stack can be calculated as follows

$$R = \frac{Z_1^{\text{input}} - Z^{\text{base}}}{Z_1^{\text{input}} + Z^{\text{base}}} \quad (3.4)$$

This reflection coefficient contains information regarding the phase and amplitude variations due to impedance translation and can be used to calculate the phase velocity dispersion across UAM components. To simplify the model, as a first approximation, all the interfacial springs are assumed to have the same stiffness such  $\kappa_j = \kappa$  for all interfaces ( $j = 1, 2, \dots, N$ ). This assumption is justifiable since each layer is built using the same build parameters. The IT model works in the frequency domain and the results are subsequently converted into the time domain by inverse Fourier transform (IFFT). The output after IFFT represents a pulse-echo measurement. The resultant waveform is then gated appropriately as discussed in the previous section, thus leading to the calculation of both the phase and group velocities.

To test the model, a component with 50 layers is chosen to have a sufficiently large number of layers and the phase velocity is calculated. The  $\eta$  value alone is changed to observe the reduction in modulus (calculated from phase velocity) due to the presence of imperfect interfaces. The reduced elastic modulus  $C_{11}^{\text{reduced}}$  that is expected to be observed in sufficiently large number of layers can be estimated as

$$\frac{1}{C_{\text{reduced}}} = \frac{1}{C_{\text{layer}}} + \frac{1}{\eta C_{\text{layer}}}, \quad (3.5)$$

where  $C_{\text{layer}} = C_{11}^{\text{intact}}$  is the longitudinal elastic modulus of the intact material. The reduced longitudinal velocity  $c_d$  and acoustic impedance  $Z_d$  of a stack of imperfectly bonded layers can be calculated as

$$c_d = c_0 \sqrt{\frac{\eta}{1+\eta}} \text{ and } Z_d = Z_0 \sqrt{\frac{\eta}{1+\eta}}, \quad (3.6)$$

respectively. In fact, the calculated modulus asymptotically approaches this value as the number of layers is increased as shown by the results in Fig. 3.6b. The asymptotic modulus was calculated directly from Eq. (3.5). In the case of the IT model the above described iterative calculation was run through  $N = 50$  layers to determine the longitudinal velocity of the stack from the time of arrival of the reflected signal and then this velocity was used to calculate the longitudinal elastic modulus using Eqs. (3.5) and (3.6). This indicates the potential for homogenization due to the repeating nature of the system. In experimental signals though, there is not only a variation of  $\eta$  across a sample, but also attenuation and dispersion at each interface. These issues are further dealt with while discussing the inversion of  $\eta$  from experimental signals in Sec. 3.4.

### 3.3.2 Finite element model

To validate this impedance translation model, a COMSOL finite element (FE) model was developed. Fig. 3.7 shows the 2D COMSOL model for a UAM component with 50 layers. The input excitation was chosen to be the same as in the impedance translation model. Each interface was modeled as a massless spring, the boundaries on the sides are chosen to be rollers and the meshing along the wave propagation direction, was chosen to be much denser than the other direction to approximate a 1D model. Probes were introduced at different locations along the model. The displacements at these selected locations were monitored for various  $\eta$  values and a convergence study was performed by increasing the mesh density and time steps. Appropriate values for the same were chosen

to have a reasonable trade-off between accuracy and solution time. It was found that the IT and the FE models are numerically equivalent.

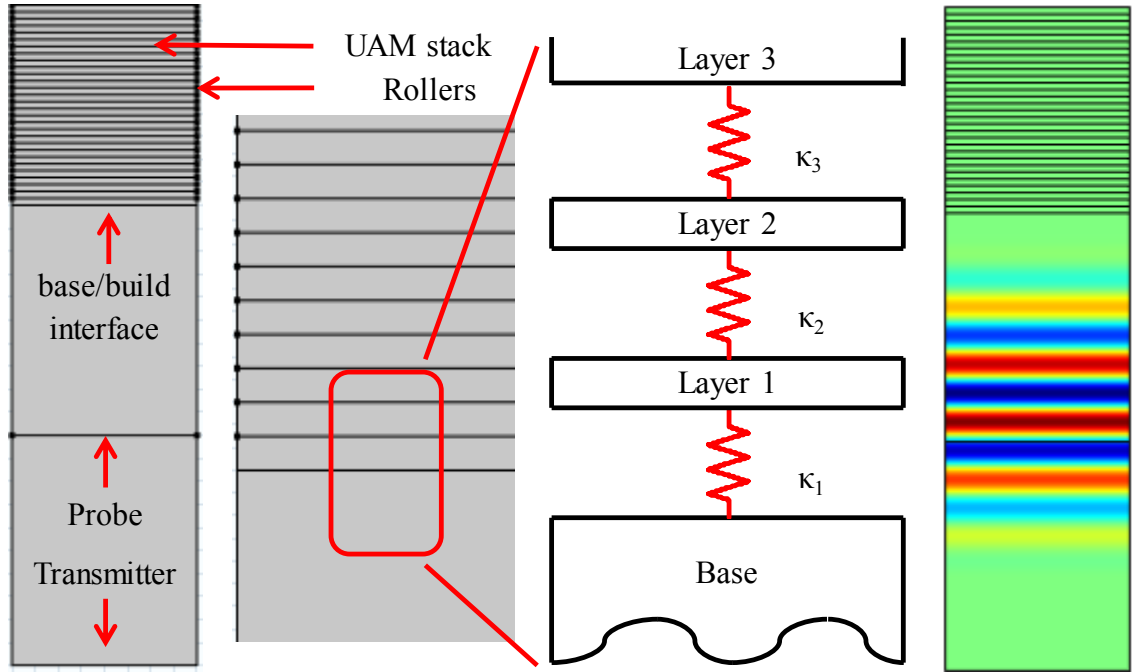


Figure 3.7 COMSOL FE model of a UAM component for modeling of ultrasonic NDE

It was found experimentally that the assumption that all the interfacial springs have the same stiffness, was not sufficient and at least two independent stiffness values are required to model UAM components, namely a common interfacial stiffness coefficient  $\eta_j = \eta$  within the stack ( $j = 2, 3, \dots, N$ ) and a separate one  $\eta_1$  for the base/build interfacial stiffness coefficient ( $j = 1$ ). The very first interface between the base and the stack is of special significance since this interface is most prone to delamination and defects. Referred to as the base/build interface, its quality needs to be studied independently. The IT model was thus changed to accommodate the two parameters and the ultrasonic group velocity was studied. The output from the IT model which is a simulated pulse-echo signal was used for calculation of the group velocity as explained in Sec. 3.1, Fig. 3.8 shows the velocity

change as layer build up occurs. Like the measured group velocity previously shown in Fig. 3.2, the simulated ultrasonic group velocity also drops during the first few layers and then recovers. Most notably, at layer two, there was a significant reduction in ultrasonic velocity for all bond qualities. This effect can now be explained to occur because of the interference of the base/build interface signal with that reflected from the top of the stack both of which have the same polarity since they have been reflected from a high-to-low impedance transition boundary. The reason this interference was destructive at the second layer is because after two layers the total travel distance within Al 6061 is around 0.6 mm which is close to half the wavelength at a center frequency of 5 MHz.

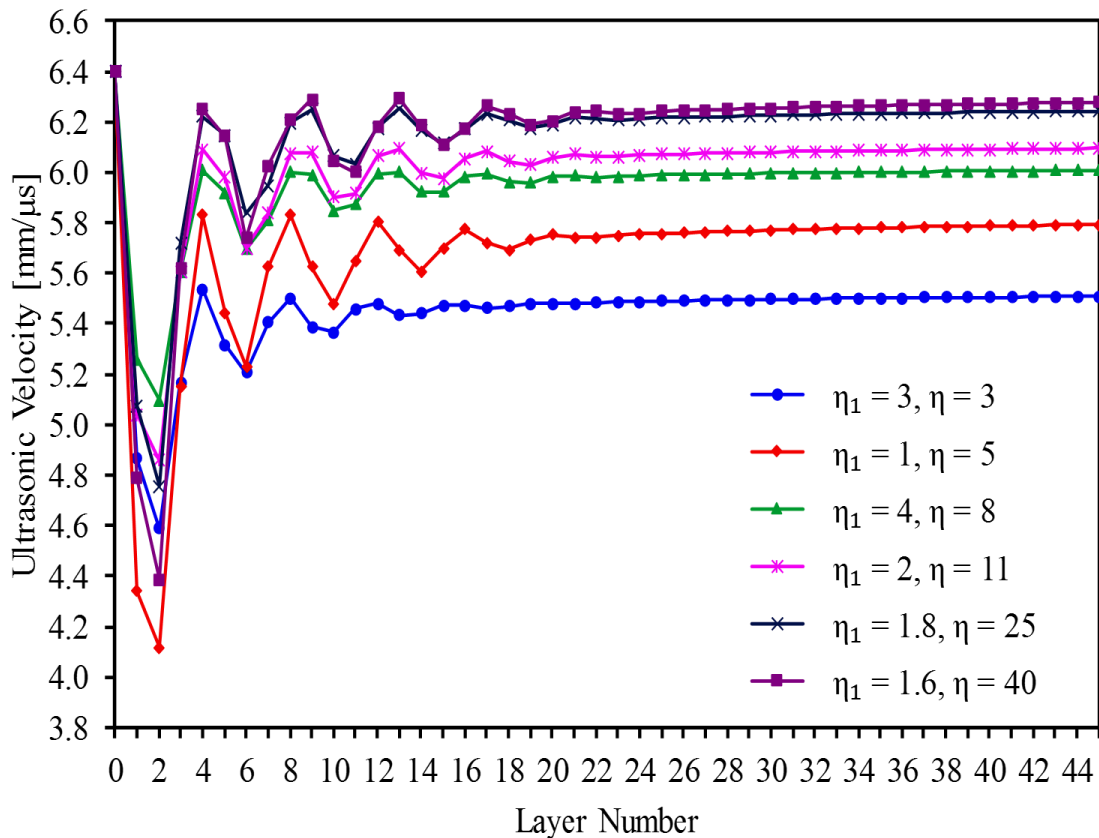


Figure 3.8 Simulated velocities for various  $\eta_1, \eta$  values

### 3.3.3 Floquet homogenization model

Due to the repeating nature of UAM components, after sufficiently large number of layers, the stack should asymptotically approach a homogeneous structure. It is of interest to calculate the impedance and phase velocity through a stack of  $N$  layers under the assumption of it being a homogeneous structure. That could provide a quick method to arrive at an average homogeneous quality parameter for a system composed of  $N$  imperfect layers. Wave propagation through periodic anisotropic media has been well documented [107, 108] especially for composite materials. To study guided wave propagation through composites, Floquet analysis was used coupled with transfer matrix/stiffness matrix methods to obtain dispersion curves at various thickness and incident angles. When ultrasonic longitudinal waves are normally incident upon periodically layered composite structures, there exist Floquet pass bands and stop bands at different frequencies. Above the first stop band, the Floquet wave behavior is rather complicated, but below the first stop band, the component can be assumed to be relatively homogeneous and only moderately dispersive.

According to finite element predictions at  $\eta = 1$  and layer thickness of  $d = 150 \mu\text{m}$ , the first stop band occurs at a frequency of  $\approx 12.3$  MHz. At  $\eta = 1$ , the build quality is considered poor since the average modulus drops to half that of the intact material. Hence at 5 MHz, the components belonging to the range of interest should lie below the first stop band, hence forming the basis for a Floquet wave homogenization approach. The periodic structure of the stack can be considered as a composite material with a repeating ABA configuration where A is the solid with half the layer thickness and B is the interfacial spring as shown in Fig. 3.9. Starting from location 1, the stress amplitudes of the forward



propagating  $A_+$  and reverse propagating  $A_-$  waves can be related to the velocity and stress as follows

$$\begin{bmatrix} v_1 \\ \tau_1 \end{bmatrix} = \mathbf{M} \begin{bmatrix} A_+ \\ A_- \end{bmatrix}, \text{ where } \mathbf{M} = \begin{bmatrix} -1 & 1 \\ Z_0 & Z_0 \\ 1 & 1 \end{bmatrix}. \quad (3.7)$$

Here and in the following equations,  $v_i$  and  $\tau_i$  denote the complex particle velocity and stress amplitudes, respectively, at the  $i^{\text{th}}$  location ( $i = 1,2,3,4$ ). At location 2, the particle velocity and stress can be related to those at location 1 according to

$$\begin{bmatrix} v_2 \\ \tau_2 \end{bmatrix} = \mathbf{N} \mathbf{M}^{-1} \begin{bmatrix} v_1 \\ \tau_1 \end{bmatrix}, \text{ where } \mathbf{N} = \begin{bmatrix} -e^{ik_0d/2} & e^{-ik_0d/2} \\ Z_0 & Z_0 \\ e^{ik_0d/2} & e^{-ik_0d/2} \end{bmatrix}. \quad (3.8)$$

Similarly, at location 3,

$$\begin{bmatrix} v_3 \\ \tau_3 \end{bmatrix} = \mathbf{P} \mathbf{N} \mathbf{M}^{-1} \begin{bmatrix} v_1 \\ \tau_1 \end{bmatrix}, \text{ where } \mathbf{P} = \begin{bmatrix} 1 & -\frac{i\omega}{\kappa} \\ 0 & 1 \end{bmatrix}. \quad (3.9)$$

Finally, at location 4,

$$\begin{bmatrix} v_4 \\ \tau_4 \end{bmatrix} = \mathbf{R} \begin{bmatrix} v_1 \\ \tau_1 \end{bmatrix}, \text{ where } \mathbf{R} = \mathbf{N} \mathbf{M}^{-1} \mathbf{P} \mathbf{N} \mathbf{M}^{-1}. \quad (3.10)$$

The Floquet periodicity condition requires that

$$\begin{bmatrix} v_4 \\ \tau_4 \end{bmatrix} = \mathbf{I} e^{-i\beta d} \begin{bmatrix} v_1 \\ \tau_1 \end{bmatrix}, \quad (3.11)$$

where  $\mathbf{I}$  denotes the identity matrix and  $\beta$  is the so-called Floquet wavenumber. If Eqs. (3.10) and (3.11) are subtracted from each other, a homogeneous matrix equation results for the velocity and stress amplitudes that has a non-trivial solution only when the following determinant vanishes

$$\left| \mathbf{R} - \mathbf{I} e^{-i\beta d} \right| = 0. \quad (3.12)$$

Then,  $\beta$  can be calculated from Eq. (3.12) and the characteristic impedance of the Floquet wave can be obtained as

$$Z^{\text{Floquet}} = \frac{\rho\omega}{\beta}. \quad (3.13)$$

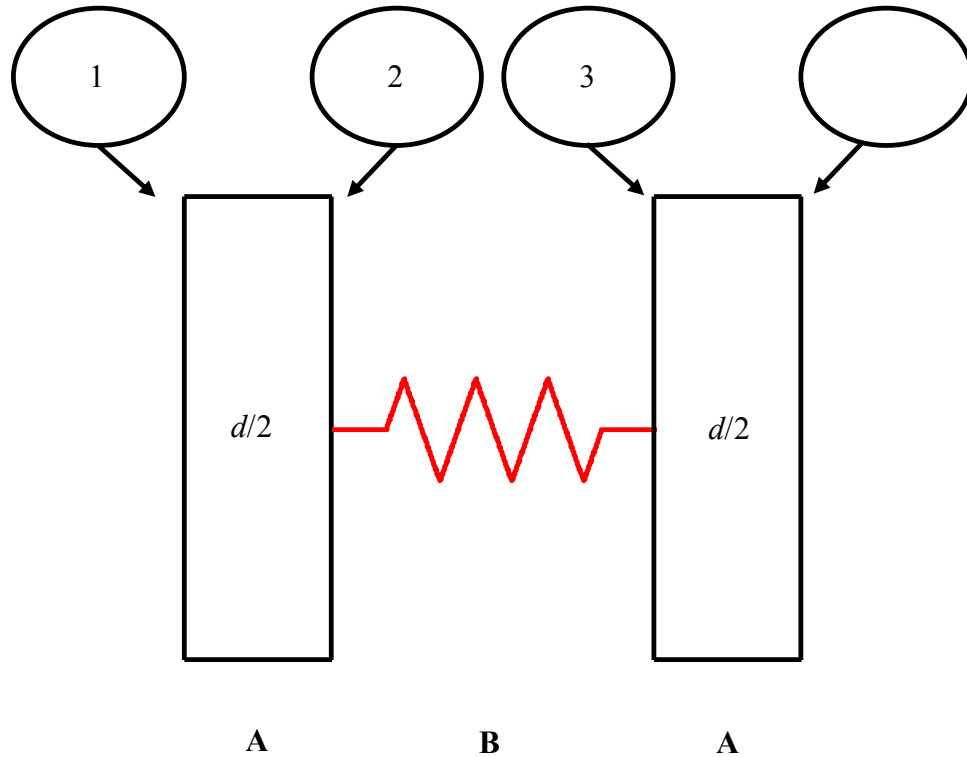


Figure 3.9 Symmetric unit cell for Floquet wave homogenization

Within Eq. (3.9), the spring stiffness ( $\kappa$ ) related to  $\eta$  appears which eventually leads to the calculation of the Floquet homogenized impedance. That is, for any given  $\eta$  value, a corresponding Floquet impedance can be calculated. In the case of UAM components, this first estimate contains coupled information regarding both the base/build interface as well as the stack. To validate the Floquet wave homogenization, a COMSOL model was used with only the UA stack at  $\eta = 10$  and a constant total stack thickness of 10 mm. A probe

on the top of the stack was used to measure the received vibration. In order to better compare the transmitted waveform, the received waveform is shifted backward by the time delay calculated from Eq. (3.6), that yields the non-dispersive or low frequency asymptote of the phase velocity. This shifting helps us estimate the amount of dispersion by comparing the received waveform to the transmitted one. The Floquet wave number was used as a propagator on the transmitted waveform in the Fourier domain and an inverse Fourier transform was used to calculate the received Floquet waveform. Several cases were studied with different layer thicknesses and three of them presented in Fig. 3.10. Interfacial stiffness coefficient  $\eta = 10$  is chosen since it represents approximately 10% reduction in the modulus and represent relatively good quality components. At low layer thickness and large number of layers, there appears to be no dispersion because the stop band is far away in frequency and the component is practically homogeneous. At layer thickness of  $400 \mu\text{m}$  some dispersion was observed and the Floquet method seems to accurately capture it. At  $500 \mu\text{m}$  layer thickness, a clear dispersion was observed and the Floquet method closely captures it with some amount of spectral distortion since the system approaches the stop band at the upper end of the bandwidth of the transmitted waveform. If the periodic system has not reached the first stop band within the bandwidth of the ultrasonic waveform used, this kind of homogenization can be utilized to estimate the dispersive phase velocity and impedance of the UAM stack. The forward problem of estimating the ultrasonic parameters such as phase/group velocities through periodic UAM structures of varying qualities was solved and validated using three different models (IT model, FE simulation, and Floquet homogenization). It is important now to solve the inverse problem of assessing the quality parameter ( $\eta$ ) from experimentally obtained ultrasonic waveforms.

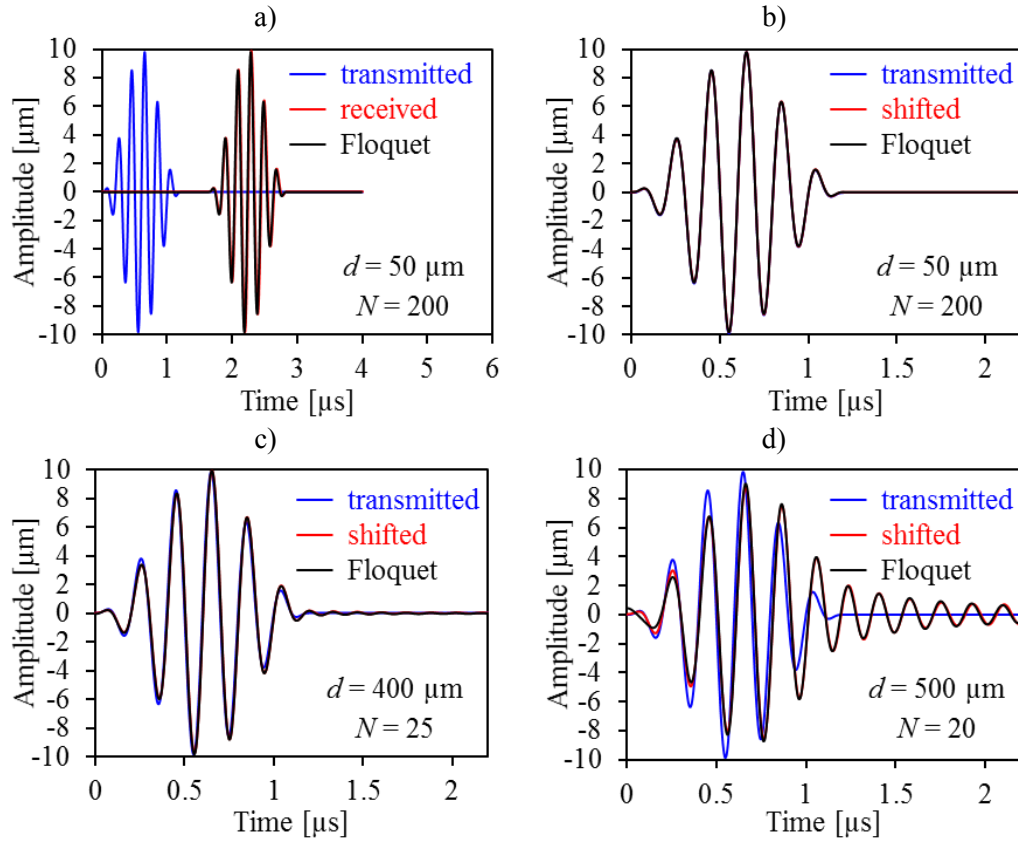


Figure 3.10 Comparison between FE model and Floquet wave homogenization model for a constant stack thickness and variable layer thickness at  $\eta = 10$ . (a) presented in the same time scale (b), (c) and (d) signals shifted to compare dispersion with respect to the transmitted signal

### 3.4 Inversion Model

Of all the imperfect interfaces in the UAM stack the base/build interface is a special one. It forms the link between the stack and the base and often is most prone to delamination with layer buildup. The reason for this is attributed to the fact that as the build height increases, the stack vibrates along with the UAM head thus producing a stress concentration at the base/build interface making it the weakest link in the chain. Often the discussion regarding the quality of base/build interface in the literature was limited to

whether the UAM stack has completely delaminated from the base. Measuring and potentially being able to control the quality of the base/build interface would create several applications where UAM can be used for repair or building on top of existing structures.

### 3.4.1 Analytical inversion model

Inversion of the bond quality of an imperfect interface between two media with impedance  $Z_1$  and  $Z_2$  was studied by several researchers for a variety of applications most prominently in rough surface contact, friction welded/diffusion bonded joints [43, 47] and adhesively bonded joints [39, 42]. Baik and Thompson [38] discussed the finite interfacial stiffness model and calculation of reflection and transmission coefficients from an embedded imperfect interface. According to the finite interfacial stiffness approximation, i.e., without interfacial inertia effects, the displacement reflection coefficient would be

$$R = \frac{\frac{Z_0 - Z_{\text{stack}}}{Z_0 + Z_{\text{stack}}} + \frac{i\omega Z_p}{2\kappa_1}}{1 + \frac{i\omega Z_p}{2\kappa_1}}, \quad (3.14)$$

$Z_0$  and  $Z_{\text{stack}}$  are the acoustic impedances of the base and the stack, respectively,  $\omega$  is the angular frequency,  $\kappa_1$  is the normal interfacial stiffness, and  $Z_p$  is a combination of the two acoustic impedances

$$Z_p = \frac{2Z_0 Z_{\text{stack}}}{Z_0 + Z_{\text{stack}}}. \quad (3.15)$$

The reflection coefficient  $R$  is calculated from an echo signal that has interacted with the base/build interface in a single action of reflection. The displacement amplitudes of all waves are measured in the incident coordinate system, therefore the reflection coefficient

from a traction-free surface is unity, i.e., positive, therefore there is no need for normalization. The reflection coefficient at the base/build interface can be re-written as follows

$$R = \frac{R_0 + y}{1 + y}, \quad (3.16)$$

where  $R_0$  is the reflection coefficient from the perfectly bounded base/build interface

$$R_0 = \frac{Z_0 - Z_{\text{stack}}}{Z_0 + Z_{\text{stack}}} \quad (3.17)$$

and  $y$  is the normalized complex inspection frequency

$$y = \frac{i\omega Z_p}{2\kappa_1}. \quad (3.18)$$

As a first approximation, the stack was assumed to be perfectly built ( $\eta \rightarrow \infty$ ), therefore  $Z_{\text{stack}}$  is real and frequency independent, though possibly different from  $Z_0$ , therefore  $R_0$  is also real. The normalized frequency  $y$  is determined from the reflection using Eq. (3.16)

$$y = \frac{R - R_0}{1 - R}. \quad (3.19)$$

The corresponding complex interfacial stiffness estimate is

$$\kappa_{\text{estimate}} = \frac{i\omega Z}{2} \frac{1 - R}{R - R_0}. \quad (3.20)$$

Eq. (3.20) is used to estimate the base/build interfacial stiffness ( $\eta_1$ ). This whole methodology depends on estimating the UAM stack impedance ( $Z_{\text{stack}}$ ) in a reliable way. The first approximation for  $Z_{\text{stack}}$  could be given by Eq. (3.6) assuming a nondispersive

reduced impedance. A simulation study was conducted with varying levels of  $\eta_1$  and  $\eta$  ranging from 1 to 100 that calculated the expected output waveform as measured in pulse-echo mode of operation with a 5 MHz broadband transducer. The respective waveforms were gated appropriately. The reflection and transmission coefficients were used to calculate  $\eta_1$ . It was found that the nondispersive approximation is lacking and is unable to predict  $\eta_1$  especially when the stack is of lower quality ( $\eta < 5$ ). Indeed, this is expected since the UAM stack behaves differently at different frequencies, but when the stack quality is high ( $\eta > 10$ ) it is practically nondispersive at 5 MHz center frequency. A better approximation for a dispersive UAM stack is given by Eq. (3.13) which uses Floquet wave homogenization. It was found that the dispersive approximation works well to estimate  $\eta_1$  when  $\eta$  is already known. This forms the basis for the proposed inversion methodology and the problem now becomes one of estimating  $\eta$  from measured ultrasonic signatures on UAM components.

Ultrasonic parameters that can be readily measured experimentally include phase velocity and attenuation. After correcting for diffraction loss, significant amount of attenuation was observed in UAM components. Under the influence of ultrasonic vibration, the modulus of the UAM stack is better represented with a complex dynamic modulus  $\tilde{C}_{\text{stack}}$  having both real and imaginary components that represent the storage and loss moduli, respectively. A complex stack modulus leads to a complex value of interfacial stiffness ( $\kappa$ ) and thus a complex quality parameter ( $\eta$ ). After some tedious algebra, the complex stack impedance can be estimated as

$$\tilde{C}_{\text{stack}} = \rho c_p^2 (1 + 2i\psi). \quad (3.21)$$

where  $\psi$  is a dimensionless real quantity representing the ratio between the imaginary ( $c_i$ ) and real ( $c_r$ ) parts of the phase velocity. It can also be related to experimentally measured attenuation ( $\alpha$ ) and phase velocity ( $c_p$ ) as

$$\frac{\alpha c_p}{\omega} = \frac{c_i}{c_r} = \psi. \quad (3.22)$$

Thus, the dynamic modulus of the UAM stack can be estimated from experimentally measured phase velocity and attenuation. The modulus of the UAM stack can be thought of as the combination of the set of imperfectly bonded layers one on top of the other. Hence, for a component of  $N$  layers and one base/build interface the modulus can be estimated as

$$\frac{N}{\tilde{C}_{\text{stack}}} = \frac{1}{d} \left( \frac{1}{\kappa_1} + \frac{1}{\kappa_2} + \dots + \frac{1}{\kappa_N} \right) + \frac{N}{C_{\text{layer}}}. \quad (3.23)$$

Since the first interface is deemed different than the rest, we can rewrite the above equation as

$$\frac{N}{\tilde{C}_{\text{stack}}} = \frac{1}{\eta_l C_{\text{layer}}} + \frac{N-1}{\eta C_{\text{layer}}} + \frac{N}{C_{\text{layer}}}. \quad (3.24)$$

For a large enough number of layers, when the system is close to homogeneous the first guess of  $\eta$  is

$$\eta \approx \frac{\tilde{C}_{\text{stack}}}{C_{\text{layer}} - \tilde{C}_{\text{stack}}}. \quad (3.25)$$

Thus, the stack quality parameter can be divided into real ( $\eta_r$ ) and imaginary ( $\eta_i$ ) parts with both terms being frequency dependent. It is important to note that this was just the



first estimate since it also includes the effects of the base/build interfacial stiffness. The proposed inversion algorithm is illustrated in Fig. 3.11. From the first guess of stack interfacial stiffness the dispersive and attenuative complex stack impedance  $Z_{stack}$  can be calculated according to Eq. (3.13). Using this and Eqs. (3.14-3.20) the first estimate of  $\eta_1$  is obtained. Then, using Eq. (3.2)  $\eta$  can be recalculated and the recursive loop run until convergence is reached. In simulation studies, the convergence was typically obtained in 2-3 loops and the predicted values of  $\eta_1$  and  $\eta$  were within 1% of the input values for simulation. The inversion methodology was shown to work well and can quickly calculate the two important quality parameters namely the average stack and the base/build interfacial stiffness coefficients.

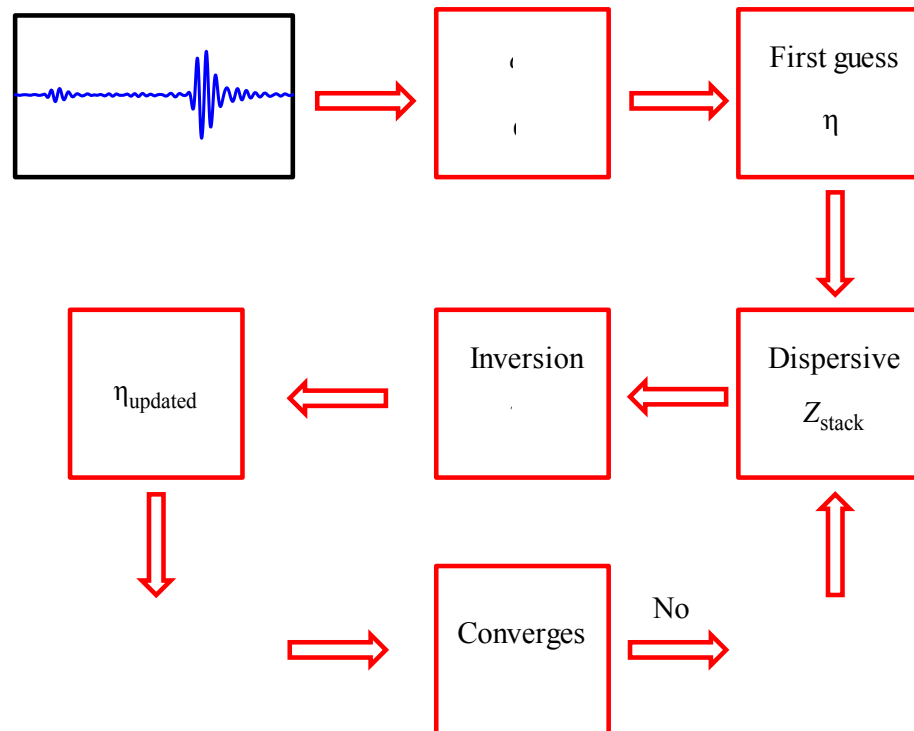


Figure 3.11 Schematic of inversion model to calculate  $\eta_1$ ,  $\eta$

Simulated waveforms are idealized cases while the waveforms from real components are often corrupted by material noise as well as changes in quality within the component. To study the sensitivity of this inversion method, another simulation study was conducted but this time a random variation of up to +/- 25% is added to the interfacial stiffness of each of the stack layers while the stiffness of the base/build interface was kept constant. It is important to calculate the sensitivity parameter ( $S$ ) of the inversion technique which can be defined as

$$S = \frac{\eta_s}{|\eta_s - \eta_{inv}|}, \quad (3.26)$$

where  $\eta_s$  is the input for the simulation and  $\eta_{inv}$  is the output inverted coefficient. Sensitivity parameter determines the region where the inversion works best. It was observed that the sensitivity parameter of measurement for  $\eta_1$  is better than that for  $\eta$ . This was expected since average random variation across several layers of the stack lead to a similar average complex stack impedance thus the error in estimation of  $\eta_1$  is significantly smaller. The average sensitivity of  $\eta$  as shown in Fig. 3.12 indicates that the inversion methodology is robust when the quality of the component lies between fair, good qualities while the sensitivity decreases when the quality of the component is very poor or very good. This indicates that not only is the inversion robust when necessary, ultrasonic NDE is well suited for measurement of UAM component quality.

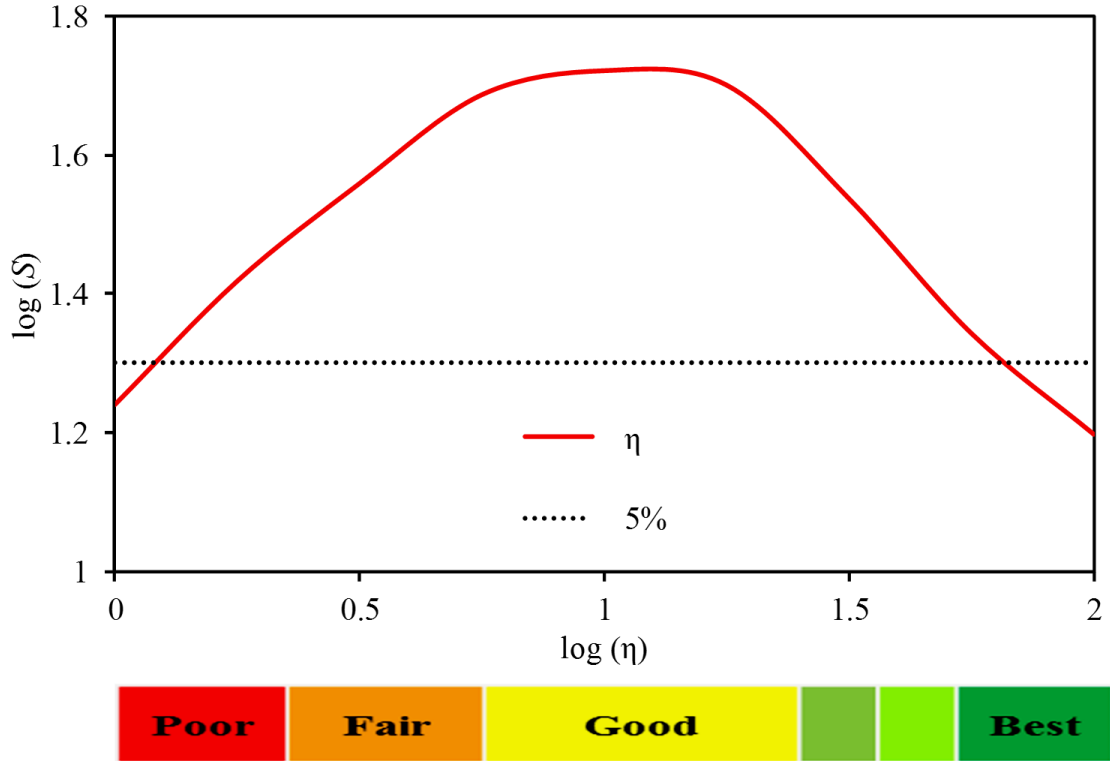


Figure 3.12 Sensitivity of the inversion model. The 5% line indicates a level of sensitivity parameter ( $S$ ) which gives greater than 95% confidence on the inversion. For  $S$  above the dotted line, the inversion methodology can be considered sensitive and robust

### 3.4.2 Inverted experimental results

Application of model-based inversion on experimentally obtained signals involves the following steps. Firstly, as it was mentioned in Sec. 3.1, two reference waveforms need to be established, one for the base thickness and the other for the stack thickness. For this purpose, a set of staircase steps were machined on an Al 6061 block ranging from a thickness of 12 mm to 24 mm with 2 mm gradation between each pair. The base plate thickness was typically around 12 mm and the stack thickness not more than that of the base. The steps were measured using the same 5 MHz ultrasonic transducer in a similar experimental setup and the diffraction loss coupled with material attenuation was

measured. Seven reference waveforms were collected on the steps that were used to measure the combined diffraction and scattering loss of the signal. The attenuation through 12 mm of solid Al 6061 was assumed to be negligible for all practical purposes. The Fourier spectrum of these reference waveforms was plotted and a linear interpolation in the Fourier domain was carried out between the spectrum of the 12 mm and 24 mm steps. It was found that all the gradations in between could be well approximated using such an interpolation. This methodology was used to estimate the base and stack reference waveforms. Secondly, the base/build interface and the stack waveforms need to be determined by appropriately gating the received signals. Gating the base/build interface signal was self-evident since it always appears at a certain time, but the same cannot be said about the reflection from the end of the stack. Using Hilbert transform, the half energy point of the stack waveform was evaluated and the gate constructed to be  $m$  cycles to the left and right of the half energy point where  $m$  depends on the number of cycles of the input signal.

The results of inversion from a set of 5 UAM samples with different vibration amplitudes is shown in Fig. 3.13. In Fig. 3.13a we see the real part and in 14b the imaginary part of the interfacial stiffness. It can be observed that the lower vibration amplitudes have both a weaker first interface (lower  $\eta_1$ ) as well as weaker stack (lower  $\eta$ ) whereas higher vibration amplitudes have both higher  $\eta_1$  and higher  $\eta$ . The imaginary parts seen in Fig. 3.13b are much smaller than the real parts seen in Fig. 3.13a. This is because the complex stack impedance has a much smaller imaginary component. Thus, physically it represents a small viscoelastic response of the layered UAM stack.

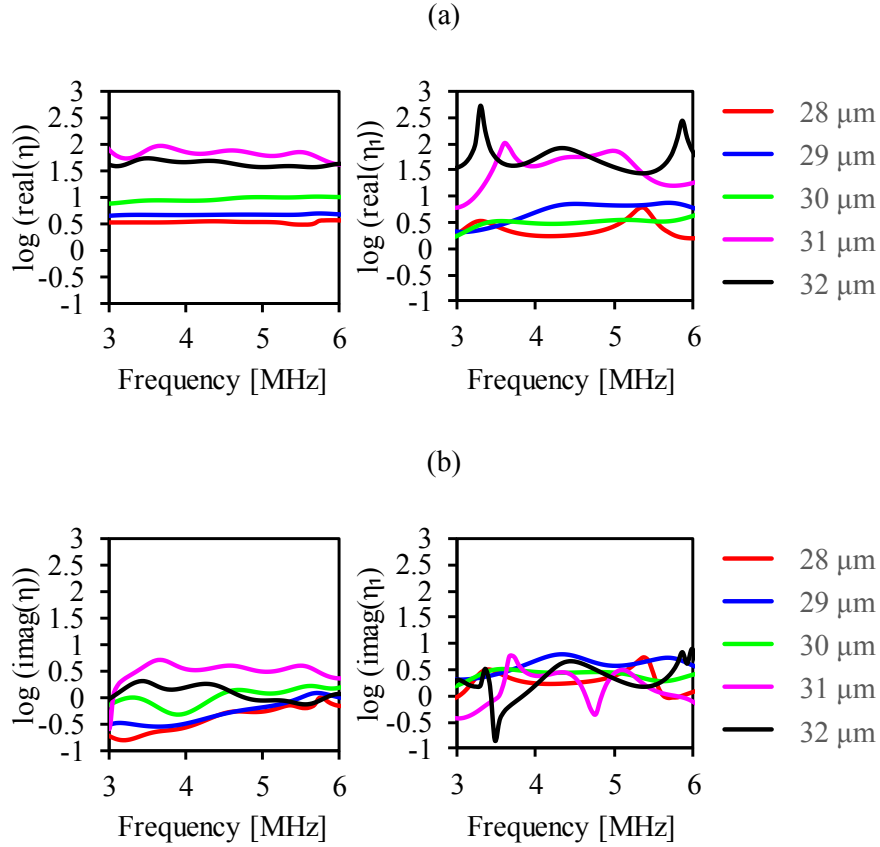


Figure 3.13 Inversion of  $\eta$ ,  $\eta_1$  after bonding 80 layers (a) real part, (b) imaginary part

It is important to note that these results are not representative of the entire 100 mm-long build and focus primarily on the best bonded regions in each sample. In this regard, it becomes obvious why  $\eta_1$  and  $\eta$  seem to follow similar trends whereas upon closer examination of the acoustic microscopy images it becomes evident that larger vibration amplitudes can cause base/build interface delaminations starting from the edges. Using the calculated  $\eta$  of the UA stack, Floquet wave homogenization can be used to estimate the homogeneous phase velocity for the calculated level of imperfection. Fig. 3.14 shows the experimentally obtained phase velocity plotted in solid line and the homogenized phase velocity plotted with markers. The average interfacial stiffness coefficient  $\eta$  calculated from inversion of the experimental signals, when used within the Floquet wave

homogenization, accurately predicts experimental phase velocities. After 80 layers, considering that the calculated  $\eta$  is an average, it is expected that the component will appear to be homogeneous. Clearly, the inversion model as well as the Floquet wave homogenized model exhibit considerable predictive power in estimating the quality of UAM components, especially after many UAM layers.

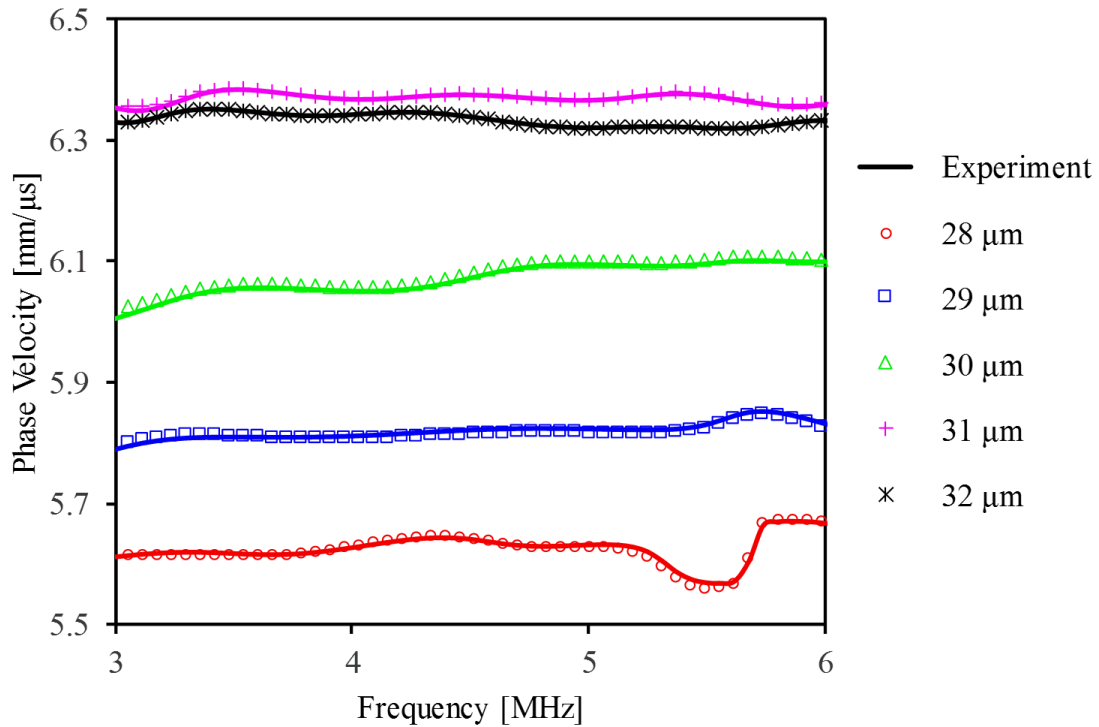


Figure 3.14 Floquet wave velocity calculated from inversion as compared to experimentally measured phase velocities. Markers represent Floquet velocities and solid lines represent experimental velocities

To test the capabilities of the inversion methodology, three components were built while performing layer-by-layer ultrasonic monitoring. Build parameters for the components were chosen such that they fall under fair, good, and best quality. Ultrasonic signals were collected continuously with an internal trigger at a repetition frequency of 4 kHz. During the bonding process, the ultrasonic signals are distorted due to intensive

vibrations. Signals acquired between layers were averaged to obtain the ultrasonic response of the layered UAM component. The inversion methodology was applied to calculate the stack interfacial stiffness. During the first twenty layers, there is an interference between the base/build echo and that from the top of the stack. Hence the results presented in Fig. 3.15 are from layer 20 onwards. It can be observed that the interfacial stiffness quality parameter oscillates with layer build up while at the same time is sensitive to build quality variations. The oscillations can be attributed to the defects within the stack, as each data point is an average of all the layers until that point. Similar behavior has also been observed in composite multilayer structures [105]. Lot of information is embedded in the layer-by-layer ultrasonic response with significant temporal resolution. By triggering the signals appropriately, it is possible to also analyze the quality of the component during bonding, though that is out of the scope of this chapter.

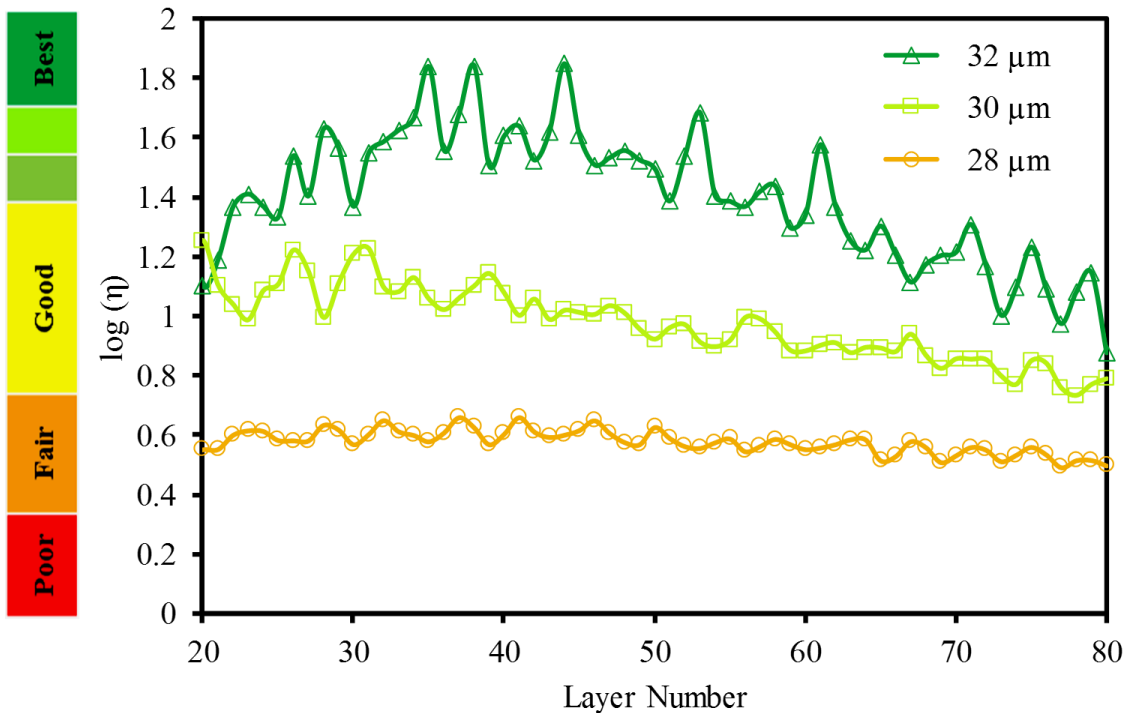


Figure 3.15 In-situ layer-by-layer inversion of bond quality

### 3.5 Conclusion

Ultrasonic Additive Manufacturing (UAM) is a promising solid-state additive layer technology with a few key problems that need to be addressed. First, the limit on building large heights due to base/build interface delamination. Second, the reduction in individual layer bond quality with layer build up. Third, inconsistent bond quality among components manufactured with the same set of technological parameters. Fourth, the reliability of existing mechanical testing methods. Fifth, the existence of tightly closed kissing bonds which are often invisible under optical examination. To solve these issues an ultrasonic nondestructive test is designed to be used in-situ during and after processing each UAM layer.

To understand how ultrasonic waves, interact with UAM component with layer build up, a wave propagation model was developed with each UAM interface being modeled as a massless interfacial spring with finite stiffness. The model was validated using Finite Element simulations. It was found experimentally that one interfacial stiffness was not sufficient to accurately model the observed phenomenon and hence two independent parameters ( $\eta_1$  and  $\eta_2$ ) were utilized. Switching to a two-parameter model, experimentally observed artifacts caused by interference between pulses could be accurately simulated. Due to the periodic nature of the structure, homogenization was attempted. It was found that Floquet wave homogenization best represents the homogeneous equivalent of the UAM stack.

Quantitative assessment of the interfacial stiffness of the imperfect interfaces between neighboring layers is required if the NDE feedback were to be used for predictive and control purposes. A two-parameter inversion algorithm was developed which centers



on calculating the base/build interfacial stiffness coefficient ( $\eta_l$ ) if the average stack interfacial stiffness coefficient ( $\eta$ ) is known. Using experimentally obtained phase velocity and attenuation curves, a frequency dependent  $\eta$  value was arrived at. At the same time, the corresponding stack impedance was estimated using Floquet wave homogenization. Both  $\eta$  and  $\eta_l$  can be recursively calculated and updated until convergence is reached. Sensitivity analysis on the inversion scheme indicates that the proposed ultrasonic NDE technique is most sensitive between average and very good quality builds with the sensitivity parameter dropping off at both extremes which indicates that the technique is robust where necessary.

The objectives of developing this methodology are two-fold. First, to evaluate components offline and acquire average quality information to be used for post-process NDE. Second, to estimate what information can be gathered in-situ for online monitoring with the goal of developing a tool that can be used within the manufacturing process. Compared to other in-situ monitoring techniques applied to the UAM process in literature, we found that the ultrasonic monitoring technique has the advantage of being able to measure the modulus of the material and the quality of each interface.

The predictive power of both the Floquet wave homogenization and the inversion algorithm were shown by correctly estimating the experimentally obtained phase velocity from the average interfacial stiffness coefficient ( $\eta$ ) of the stack. Preliminary online in-situ monitoring results indicated the sensitivity of layer-by-layer ultrasonic monitoring. The results of this work pave the way for the development of an online in-situ ultrasonic NDE monitoring system. Even if ultrasonic NDE might not be utilized online for more complex-shaped components, this work provides a framework for quantifying the NDE results.

Monitoring the evolution of bond quality not only inside the stack but also at the base/build interface would help prevent delaminations and improve the reliability of the UAM process. NDE of the base/build interface quality requires further extension of the work presented in this chapter and will be discussed in Chapter 4 of the dissertation.

CHAPTER 4  
MONITORING AND REPAIR OF DEFECTS IN ULTRASONIC ADDITIVE  
MANUFACTURING <sup>3</sup>

#### 4.1 Introduction

Metal Ultrasonic Additive manufacturing (UAM) is a layer-by-layer metal solid-state bonding process which is commonly used in conjunction with a Computer Numerical Control (CNC) mill. A 20 kHz ultrasonic horn or sonotrode vibrates at amplitudes varying from 10 to 50  $\mu\text{m}$ . A high normal force is applied to facilitate solid-state ultrasonic welding of thin metal foils on a base substrate. UAM can produce functional components with embedded optical sensors or electronics, parts with fully enclosed internal cooling channels or heat exchangers, parts in multi-materials or composites [2, 4, 109, 110, 111, 112]. The quality of UAM parts is dependent on several factors including process parameters (amplitude of vibration, clamping force, welding speed, and substrate temperature), surface condition of the foil, substrate, and sonotrode, geometry of the build [6, 21].

UAM can produce good quality functional components but these components are sometimes prone to defects and delamination typical to UAM. Several studies focus on developing optimal process parameters for UAM and then eliminating defects through

---

<sup>3</sup> This chapter has been prepared as a manuscript to be submitted to *Journal of Materials Processing Technology*. All permissions to use this paper as a part of this dissertation are contained in the Appendix.

post-weld treatments [11, 23, 27, 94, 103, 113, 114, 115, 116]. To form a good bond, there must be enough power input into the ultrasonic weld while at the same time ensuring that already bonded interfaces are not pulled apart due to excessive vibration or power input [103]. Defects in UAM are labeled as Type-1 for inter-layer defects and Type-2 for inter-track defects [4, 115]. While most of UAM literature is focused on reducing Type-1 defects, fewer studies focus on Type-2 defects. It is useful to classify Type-1 defects into two subgroups, Type-1a for base/build delamination and Type-1b for defects within the stack. Nadimpalli *et al.* [96] found that this distinction is important because the base/build interface is prone to delamination. In fact, this is one of the limiting factors while building components with height-to-width ratio  $> 2$  [11, 116]. Since UAM part quality is geometry dependent, the optimal build parameters need to be changed with build height. Hehr *et al.* [103] reported on the effects of build compliance on bond quality and suggested power compensation. While this works for Type-1b defects, it might exacerbate Type-1a defects and doesn't address Type-2 defects. It is important to consider Type-1a defects since the base could also form a part of the final UAM component.

The low process temperatures in UAM allow for monitoring of Type-1 defects during part fabrication using ultrasonic NDE techniques [96, 117, 118]. Further, Type-I defects are characteristically planar and ultrasonic NDE is well-suited for such defects. In previous work Nadimpalli *et al.* [117, 118] has designed an in-situ monitoring setup with a fully enclosed high frequency (5-10 MHz) NDE transducer below the base substrate. Preliminary results indicated that Type-1a defects are common even if they are not physically visible to the naked eye since the UAM component is strongly bonded to the base but parts of it are delaminated at the base/build interface. An interfacial spring model-

based inversion technique was proposed which considers each UAM interface to be acting like a spring under ultrasonic NDE vibrations. There is ample evidence that suggests the modeling of UAM components as imperfect interfaces [38, 40, 47]. The stiffness of such interface layers can be measured in-situ layer-by-layer and can provide a quantitative evaluation of UAM interfaces. Offline ultrasonic NDE can also be used to calculate the elastic constants of UAM components and image internal features such as Type-1a defects [26]. NDE studies need to be backed up with destructive correlation which can be achieved through the means of a push-pin test proposed by Zhang *et al.* [20]. Other mechanical tests such as lap-shear and tensile have been shown to be correlated to area under push-pin load-displacement curves which represents the work done in extruding 10-15 UAM layers in a 3-point bend configuration.

Both Type-1 and Type-2 defects in UAM components need to be eliminated either through improving the process or healed after manufacturing, so that UAM components can be used for structural applications [94,114]. Post-process heat treatment of UAM components was shown to be effective in increasing bond quality and reducing Type-1 defects, but heat treatment can't fix Type-2 defects. Due to the variability in processing conditions that affect bond quality, it is imperative to develop a methodology to heal/repair the typical defects in UAM. Given that the primary advantage of UAM is solid-state processing, it is meaningful to consider only solid-state techniques for repair of defects in UAM parts. Several other friction-based solid-state additive manufacturing techniques like friction deposition [119], friction lap-seam welding [120] and Friction Stir Additive Manufacturing (FSAM) [121, 122] have been proposed and demonstrated for various materials. All these methods involve a layer-by-layer manufacturing or joining of material

to near-net shape and have been suggested for making larger size components compared to UAM. Out of the existing friction-based solid-state processes, FSAM, which is essentially layer-by-layer Friction Stir Welding (FSW), appears to be most promising. Mishra *et al.* [123] proposed Friction Stir Processing (FSP) as a solid-state tool for improving the microstructural characteristics of materials. FSP has been demonstrated for creating fine grain microstructure, surface and bulk composites, in-situ multi-material synthesis and for healing crack and surface defects. In Sec. 4.2 of this chapter, we present the mechanism for Type-1a (base/build interface) delamination and propagation along with a qualitative nondestructive evaluation of Type-1 defects using both in-situ and offline ultrasonic NDE. In Sec. 4.3, we propose Friction Stir Processing as a novel repair tool to completely heal both Type-1a and Type-2 defects. Type-1a defects are necessarily healed after UAM processing while Type-2 defects can be healed in-situ. We thus propose for the first time an integrated solid-state process with UAM as the primary bonding mechanism and FSP as a repair and refinement tool.

## 4.2 Monitoring Evolution of Defects in UAM

### 4.2.1 In-situ and offline ultrasonic nondestructive evaluation

Two possible approaches of in-situ monitoring were previously proposed and tested [96, 117, 118], one from above the UAM stack and the other from below the base plate. Monitoring from below was found to be a practical approach which can be used for continuous online quality monitoring. The primary challenge was to ensure that the addition of the in-situ monitoring system does not alter the quality of UAM components. Supports were required to raise the base plate to accommodate the in-situ monitoring

system. Supports along the bonding and vibration directions were tested and it was found that raising the base plate alters the quality of UAM components as compared to the reference. Thus, a new set up was implemented wherein the ultrasonic NDE sensor was entirely embedded in a large solid block of aluminum as shown in Fig. 4.1. The sensor was changed from contact mode to immersion so that the vibrations produced during UAM processing do not affect the coupling. High temperature lubricant oil was chosen as the coupling agent since it is stable up to 500 °C. Through mechanical testing, it was shown previously that the quality of UAM components built on this set up were comparable to that of reference components built with no transducer beneath them.

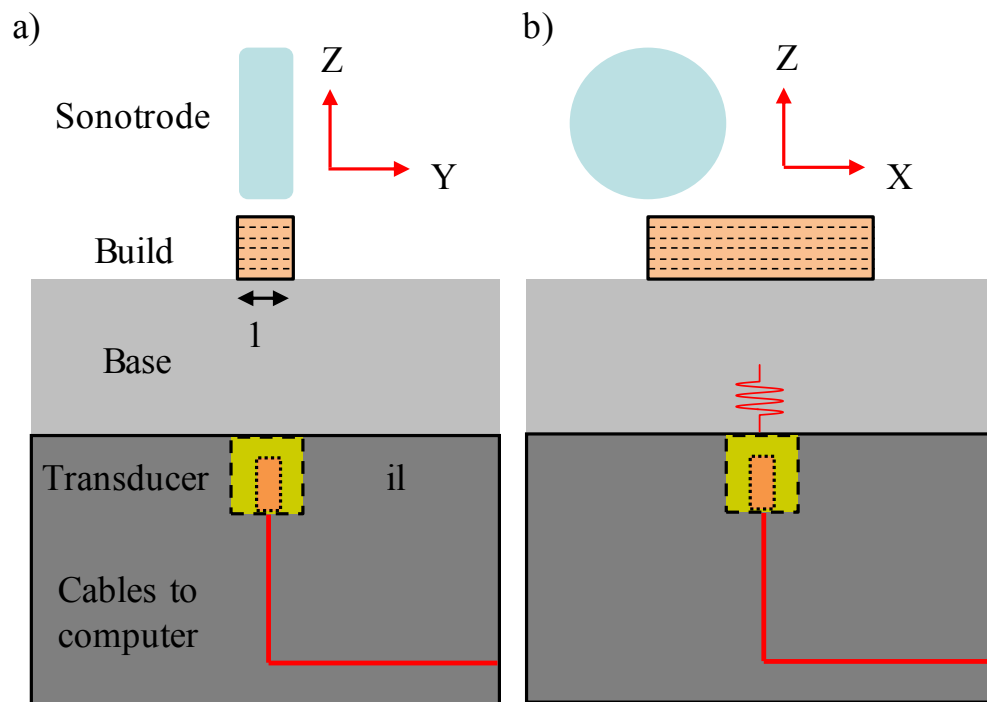


Figure 4.1 In-situ monitoring ultrasonic NDE setup with fully embedded sensor a) front view, b) side view

Using the optimized in-situ sensor setup, UAM components were built with 30 layers of Al 6061- 18 foils (150  $\mu\text{m}$  thick) on an Al 6061 base plate. Using 5000 N normal

force, 85 mm/s welding speed and 100 °C baseplate preheating, six test components were made by varying the amplitude of sonotrode vibration in the range of 30 to 37  $\mu\text{m}$ . The UAM experiments were conducted on Soniclayer R7200 system located at Fabrisonic. The in-situ NDE sensor was a 10 MHz, 6 mm unfocused delay line immersion probe. In-situ continuous monitoring was performed so that information was captured throughout the bonding process. In an earlier work, Nadimpalli *et al.* [117, 118] observed that high frequency noise corrupts the NDE response during UAM, which creates both an amplitude modulation and a phase shift in the signal. The bonding time for a 100 mm long single track is around 1.2 seconds with a dwell time of 70 ms in the central 6 mm section that is illuminated by 10 MHz ultrasound. With a pulse repetition frequency (PRF) of 20 kHz, 1400 waveforms are collected and saved in this time interval. The amplitude and frequency modulation of the NDE sensor (10 MHz) by the ultrasonic horn (20 kHz) are beyond the scope of this current chapter. The vibration amplitudes produced by the NDE sensor are in the sub-nanometer scale and wouldn't conceivably affect the UAM bond quality. Since we are continuously monitoring, we can focus on the interval after UAM bonding before a new layer begins during which time the NDE sensor is able to measure the UAM component with no interference. During this time, the UAM system snips the tape and prepares for the next layer with the whole process taking around 10 seconds. Capturing the data after each layer of UAM bonding provides information about the evolution of quality with layer build up. Fig. 4.2 shows two components of vibration amplitude 36 and 37  $\mu\text{m}$ . The lower amplitude (black) has good bonding and the higher amplitude (red) has a delamination at the base/build interface. The ultrasound first travels through the oil followed by the base. It then hits the base/build interface which might have a reflection



depending on the quality. The transmitted ultrasound travels through the UAM stack and gets reflected from the top layer. The reverberations at the start of the oil buffer are edited out so that the features of interest can be focused on. To compare the signals from two components, the reflection from the oil/base interface is used to line up the signals so that the time delay can be compared.

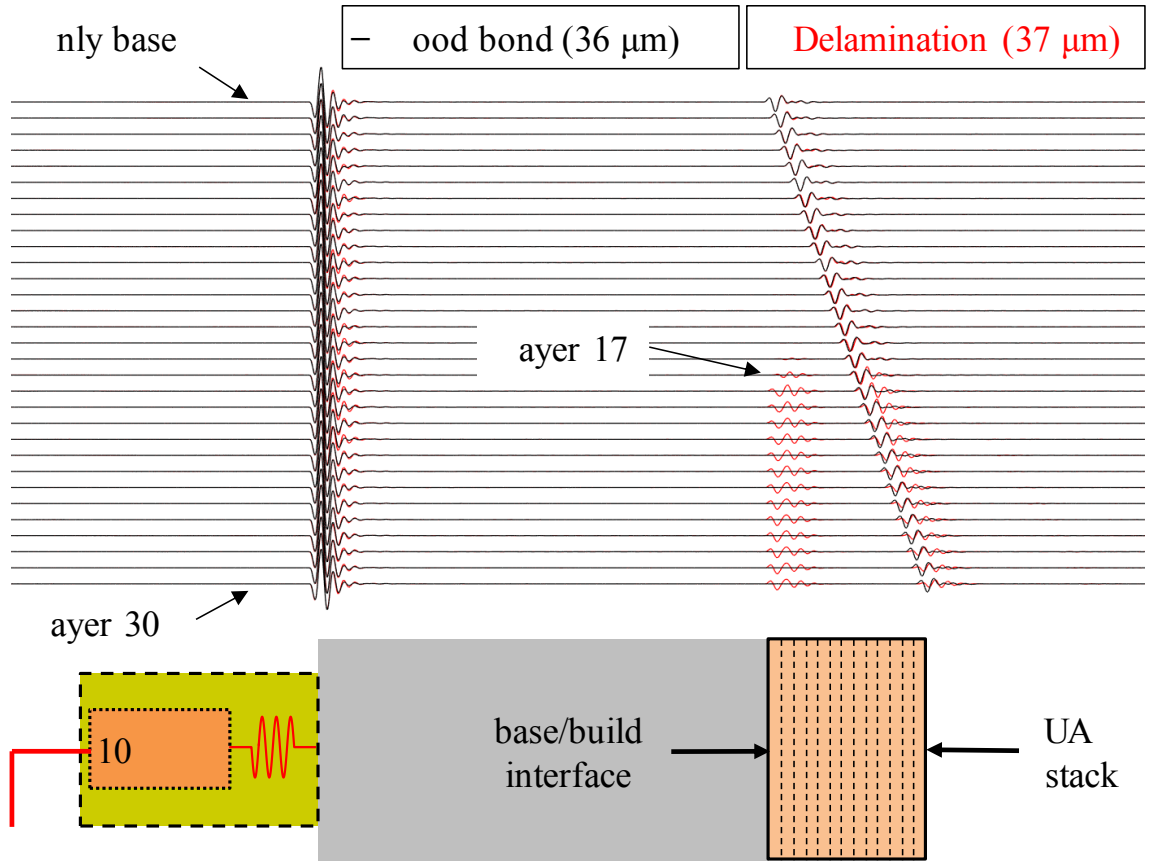


Figure 4.2 In-situ monitoring after bonding each UAM layer for two components of varying quality. The reverberation from the oil buffer was cut out from the signals, so that the features of interest can be better represented

With increasing layer number, the signal appearing from the top of the UAM stack appears after a time delay due to the addition of extra propagating distance. In the delaminated component, from the 17<sup>th</sup> layer an indication for base/build interface delamination appears that grows stronger. At the same time, there is also propagation

through the base/build interface evidenced by the signal from the top of the stack. To extract bond quality information from the experimental signals, it is important to model wave propagation through UAM components. Modeling the experimentally observed phenomenon requires a distinction between the base/build interface and the rest of the stack. A framework for modeling wave propagation through UAM components has been presented in Nadimpalli *et al.* [117]. UAM components have a clear distinction between bulk foil layer and a small interface layer where bonding occurs. Thus, a wave propagation model was developed with each UAM interface acting as a massless interfacial spring with finite stiffness as shown in Fig. 4.3. The interfacial stiffness ( $\kappa$ ) represents the quality of the interface layer and is defined as the ratio of the stress to the interface crack opening displacement. It is normalized according to  $\kappa = \eta C_{11} / d$ , where  $\eta$  is an interfacial stiffness coefficient,  $C_{11}$  is the elastic stiffness modulus of the layer material, and  $d$  is the layer thickness. The interfacial stiffness coefficient ( $\eta$ ) is a normalized, dimensionless coefficient which represents the quality of an imperfect layer.

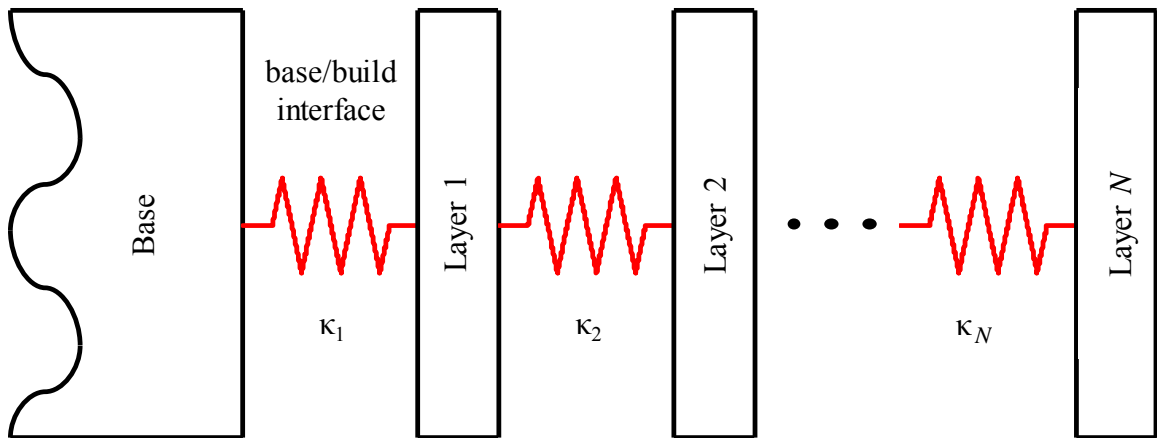


Figure 4.3 Schematic of UAM interfaces as finite stiffness springs [117]

A zero-stiffness layer indicates a free surface and an infinite-stiffness layer indicates a rigid boundary. Two interfacial stiffnesses  $\kappa_1$ ,  $\kappa$  represent the base/build

interface and the average stiffness of each layer in the UAM stack respectively. A layer thickness ( $d$ ) of  $150\ \mu\text{m}$  is considered so that the stiffness values can be compared to those of a single UAM layer. The interfacial spring stiffness has been used extensively in NDE literature as a measure of quality of imperfect interfaces. A model-based inversion methodology was presented in Nadimpalli *et al.* which details the extraction of stiffness values from in-situ ultrasonic signals [117]. Fig. 4.4 shows the two independent stiffness values  $\kappa_1, \kappa$  for the six components.

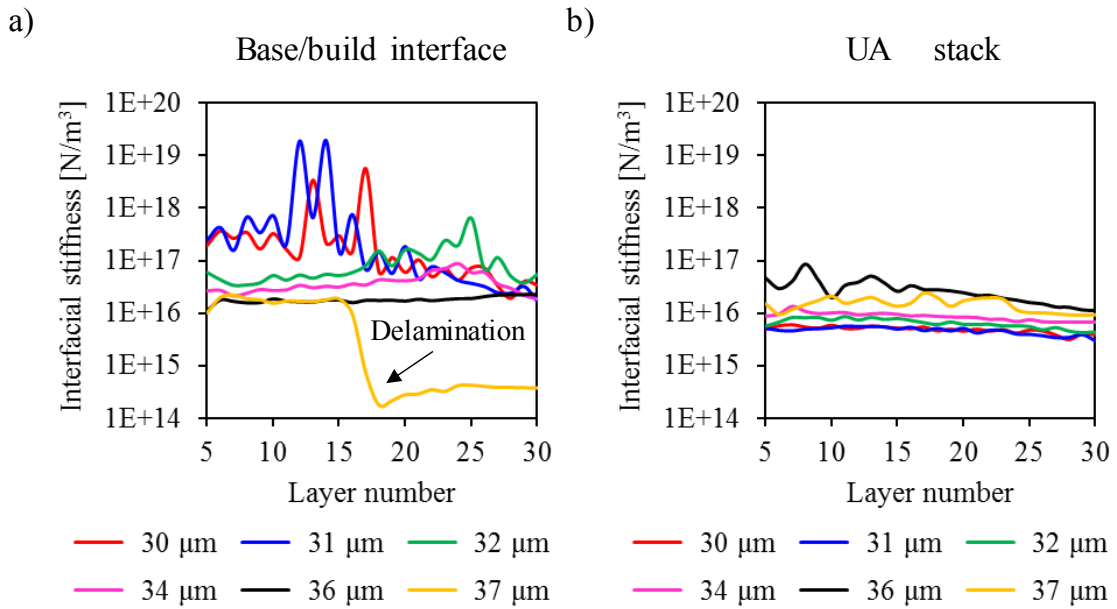


Figure 4.4 Interfacial stiffness values of components with varying quality a) base/build interface, b) average of UAM stack

As the vibration amplitude increases, the stack stiffness increases until  $36\ \mu\text{m}$  and then decreases. The base/build interface stiffness on the other hand decreases with increasing amplitude. The component with  $37\ \mu\text{m}$  amplitude shows a stark reduction in the base/build interface stiffness from layer 17 onward as seen from the raw signals data presented in Fig. 4.2. UAM literature widely agrees that the optimal UAM bonding

conditions need to have enough energy input into the component to create a good bond but not too much so that it causes a delamination either at the base/build interface (Type-1a defect) or within the UAM stack (Type-2 defect).

#### 4.2.2 Base/build interface evolution

The base/build interface is most prone to delamination with layer build up. Delamination at this interface is often a limiting factor on build height. For certain applications, the base is also a part of the structure of interest. In such a case, it is necessary to measure and monitor the quality of the base/build interface. For applications where the base is not a part of the structure of interest, a certain amount of base/build delamination is acceptable if the structure remains firmly attached to the base. In both cases, it is imperative to understand the mechanism of base/build interface delamination. Ultrasonic NDE is a useful tool to measure the quality of UAM components not only in-situ but also after fabrication. This is henceforth referred to as offline NDE, since the UAM component is removed from the machine. The top surface of a UAM component is rough and its texture is dependent on sonotrode roughness (typically 7-20  $\mu\text{m } R_a$ ). This level of surface roughness limits the frequency of measurement due to surface attenuation. Hence, offline NDE is best performed from below the base substrate. The six UAM components were hence immersed in a SONIX acoustic microscopy tank filled with water and a delay line immersion unfocused transducer of frequency 5 MHz was used for inspection. Ultrasonic A-scan signals gathered from below the base have three distinct features, the oil/base interface, the base/build interface, and the top of the UAM stack as can be observed from Fig. 4.2. Ultrasonic C-scans were obtained by gating a region of interest that corresponds

to a height within the component while scanning across the other two axes as shown in Fig. 4.5. A 100  $\mu\text{m}$  resolution was used along both the scanning and stepping axes to generate an image of the base/build interface henceforth referred to as the reflection image, and an image from the top of the UAM stack henceforth referred to as the transmission image. In existing literature, the mechanism of base/build interface delamination has not been thoroughly explored.

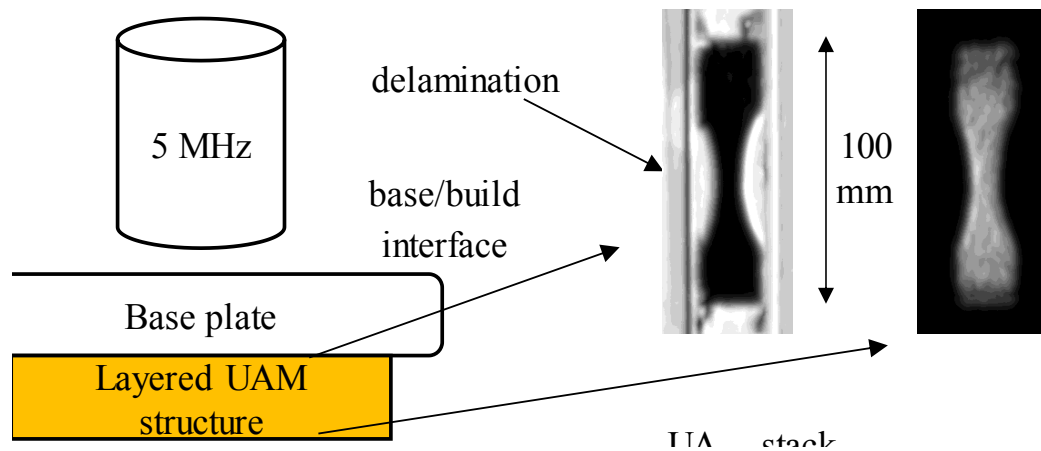


Figure 4.5 Acoustic microscopy gated to generate images at the base build interface (reflection image) and the UAM stack (transmission image)

Before bonding the first layer, the base was machined and retextured to facilitate better bonding conditions. It was experimentally observed that this produces better results as far as Type-1a defects are concerned. Fig. 4.6 shows C-scan images that are presented in grey scale with white indicating a higher value. The reflection image depicts the quality of the base/build interface, with a lower reflection representing better quality. The transmission image depicts the quality of the UAM stack, with a higher transmission representing better quality. Base/build delamination can be observed in both the reflection and transmission images. In the reflection image, good bonding corresponds to a black

region, while in the transmission image, good bonding corresponds to a white region. At each point. The reflection images indicate that the base/build delamination increases with vibration amplitude and can be far more prevalent than what is visible to the naked eye.

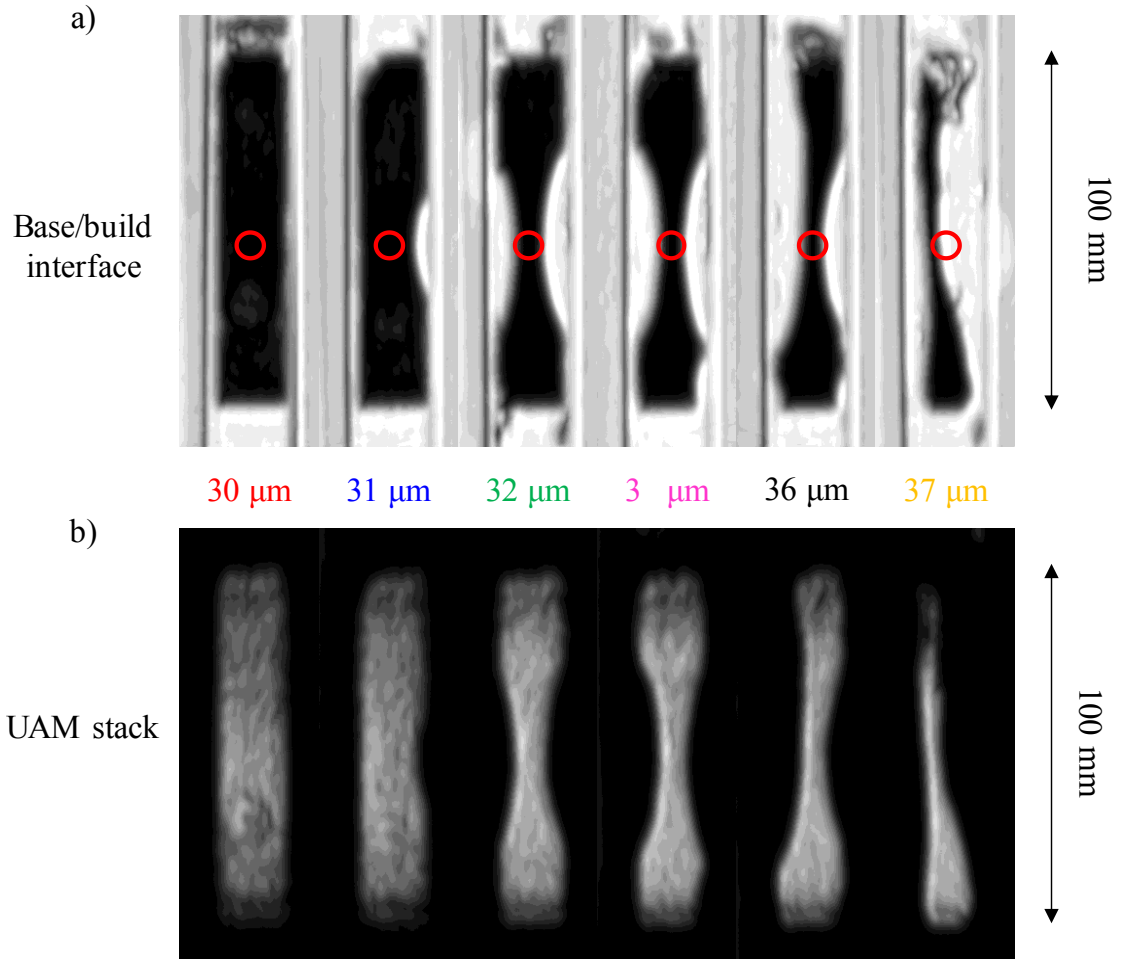


Figure 4.6 Acoustic microscopy of UAM components at a) base/build interface (reflection image) and b) The top of UAM stack (transmission image). In the reflection image, black indicates a good bond while in the transmission image white indicates a good bond

In the components built with 30, 31  $\mu\text{m}$  vibration amplitude, the base/build delamination occurs on the inside and is localized to a small region (below the red circles). The red circles indicate the location of the in-situ monitoring NDE sensor for comparison

with the interfacial stiffness values. Components 31-37  $\mu\text{m}$  have delamination starting from either one or both long edges. In Fig. 4. , up to amplitude 36  $\mu\text{m}$ , no delamination was visible, but that is primarily because of the small field of view. It should be noted that all these components were firmly attached to the base and the component couldn't be manually separated. The component with 37  $\mu\text{m}$  vibration amplitude has Type-1a defects of two types, starting from the edge and regions of partial bonding that don't appear to have started on the edge. Based on the acoustic microscopy images, components 32, 34 and 36  $\mu\text{m}$  should have shown at least a small reflection during in-situ monitoring. It is hence conceivable that after removal from the heated base plate of the UAM system, the components relax and the delamination spreads further inward.

Due to the visualization provided by offline ultrasonic NDE, we can distinguish between three kinds of Type-1a defect evolution. The first is due to low energy input which leads to poor bonding. It occurs primarily on the inner side of the UAM weld and likely occurred during building the first few layers. The second kind of defect starts from the edge and occurs due to the vibration of the UAM stack with build height. The base/build interface acts as a stress concentration which takes the load from the vibrating stack. It is hence prone to delamination starting on the edges. In several components these cracks start from the edge and propagate inward along a circular arc. The UAM bonding process itself is akin to 20 kHz cyclic fatigue. All evidence indicates that these interfaces were once bonded and then delaminated due to cyclic loading. The third kind of defect is due to excessive energy input during building the first few layers that leads to a damaged base/build interface which also occurs on the inside of the UAM weld. Thus, to maintain a good base/build interface, the vibration amplitude must be optimal during building the first

few layers followed by which there must be a reduction in vibration amplitude to reduce the load on the base/build interface. But this approach is not feasible since it leads to Type-1b defects which will be discussed in further detail below.

#### 4.2.3 UAM stack quality

UAM stack quality is dependent on geometry as substrate stiffness affects the ultrasonic energy input. The effect of build compliance on power drawn during UAM has been reported by Hehr *et al.* [103]. Optimum vibration amplitude is dependent on component geometry. In single track components, the vibration amplitude requires change after every layer with build height. This is referred to as an amplitude-compensated UAM component. Contrary to the quality of the base/build interface, it is important to increase the vibration amplitude so that the same amount of power is input into the UAM component. Fig. 4.7 shows the cross section of 80-layer, 11.5 mm thick component built at 32  $\mu\text{m}$  vibration amplitude. The first 7.5 mm from the bottom have good layer bonding with no visible delamination (up to the dashed white line). In the remaining 4 mm, several delamination defects are observed at interfaces between layers. These are referred to as Type-1b defects and are caused due to the insufficient power input into the UAM component.

To utilize vibration amplitude as a parameter to control and study UAM component quality, it is pertinent to establish the accuracy and resolution of the ultrasonic welder. For this purpose, a laser vibrometer was aimed at the weld-head of a Fabrisonic R200 UAM system and the vibration amplitude was measured. The R200 system is an experimental open architecture machine that is ideal for research and development. The percent



amplitude setting is an operator input into the UAM system. The DUKANE iQ welder used in UA allows for a 1 resolution which approximately corresponds to 0.5  $\mu\text{m}$  amplitude change. The average standard deviation measured with laser vibrometer at various amplitude setting levels was approximately 0.2  $\mu\text{m}$ . This indicates that the control system is highly accurate and there is a clear distinction between vibration amplitude settings separated by 0.5  $\mu\text{m}$  or more. UA components were also measured during welding and it was found that the control is equally good under load.

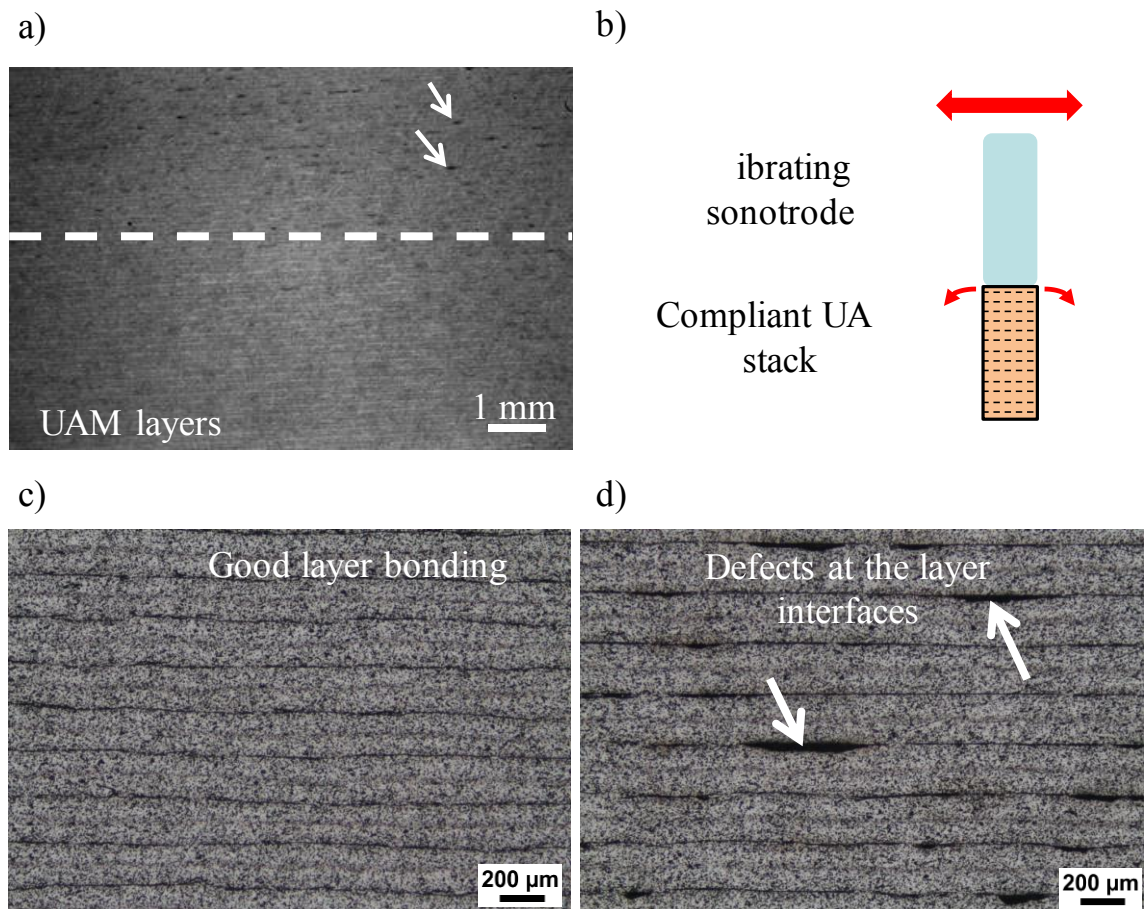


Figure 4.7 (a) Low-magnification optical micrograph of a 11.5 mm height UAM sample. (b) Schematic of a compliant UAM stack. In the first 7.5 mm from the bottom, the sample showed good layer bonding (c). In the top 4 mm, several Type-1b defects (marked by arrows) were seen at the layer interfaces (d)

After validating that the vibration amplitude of the horn is very close to the input value, the mechanism of Type-1b defect formation becomes evident. As the build height increases, the UAM structure is more compliant thereby requiring less power to keep the ultrasonic horn vibrating at the same amplitude.

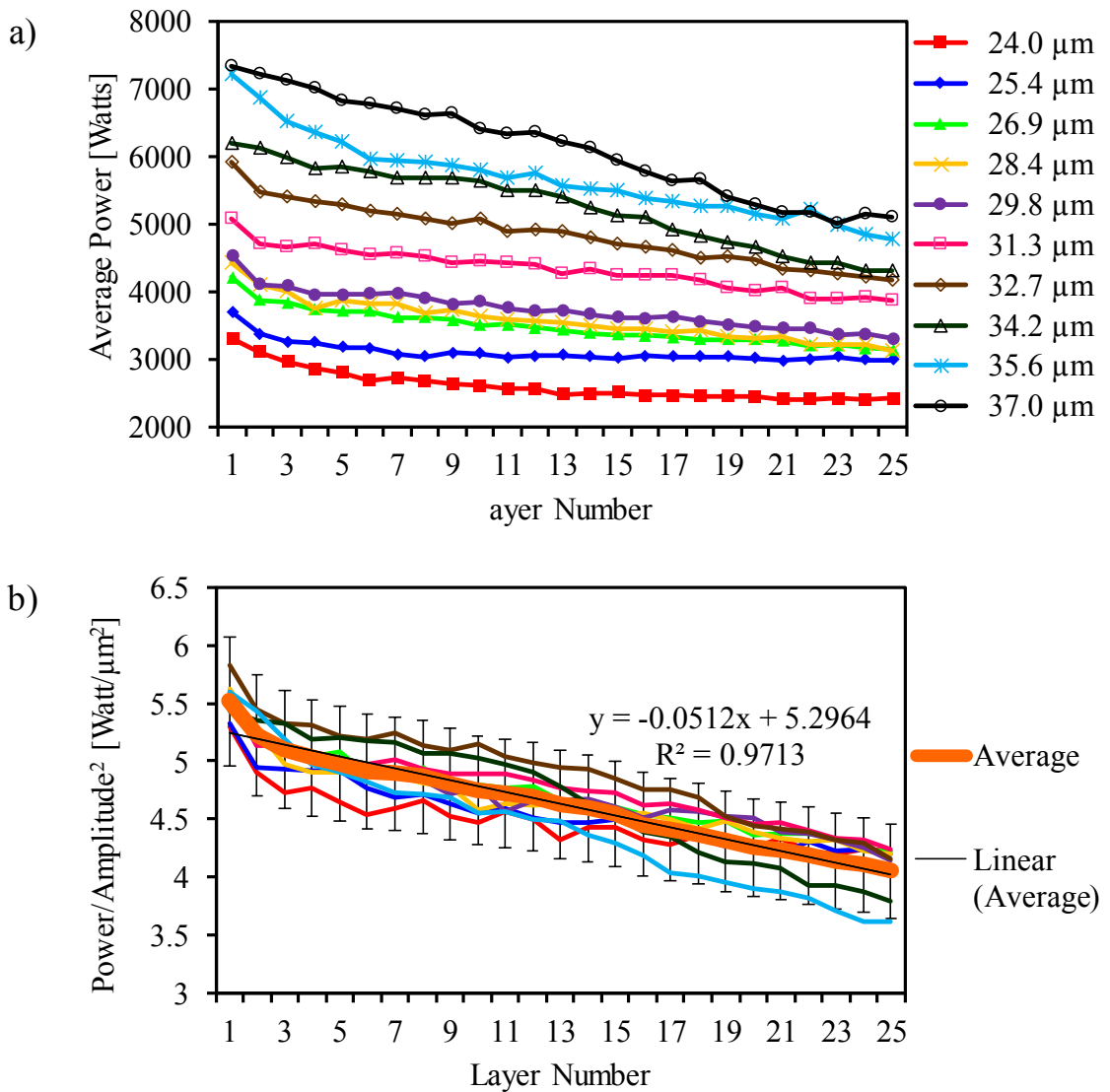


Figure 4.8 a) Change in average weld power with layer height for varying vibration amplitudes b) Normalized power

To test the change in weld power with layer height, a test was conducted on the R200 system. UA components with 25 layers of 150  $\mu\text{m}$  thick Al 6061 foils that are 76 mm long were manufactured with varying vibration amplitudes. The average power is a readout parameter on the DUKANE iQ welder. It represents the average power drawn by the ultrasonic horn to accurately maintain the vibration amplitude. Fig. 4.8a shows the changes in average weld power with layer height for varying vibration amplitudes. In each case, the power reduces with layer build-up. Fig. 4.8b plots the power normalized with square of the vibration amplitude. The normalized power at various amplitudes falls within a  $\pm 10\%$  standard deviation at every layer height and follows a decreasing trend. In an amplitude compensated UAM build, the power does not reduce with build height thereby enabling similar ultrasonic energy input into each layer. The orange line represents the average of normalized power for all the vibration amplitudes. A linear fit has an excellent R-squared value and indicates that the average power is decreasing with build height. The negative slope is representative of the compliance of the UAM stack while the intercept of the linear fit indicates the normalized power for the other bonding parameters (normal force, welding speed) and material.

With in-situ monitoring, it is possible to quantify the change in modulus with layer build up in an amplitude-uncompensated UAM build. Fig. 4.9 shows the modulus of various components calculated from the average stack interfacial stiffness. These components were built on the Fabrisonic R7200 UAM system located at Edison Welding Institute. With increasing amplitude, the stack modulus is higher and with increasing layer number, and the stack modulus steadily reduces. The component with 37  $\mu\text{m}$  vibration amplitude has a lower stack quality than the one with 36  $\mu\text{m}$  amplitude. For the first several

layers, the 37  $\mu\text{m}$  amplitude inputs extra power into the component which causes Type-1a and Type-1b delamination. This is also evident from Fig. 4.6 which shows the third kind of Type-1a defects that form due to excessive power input.

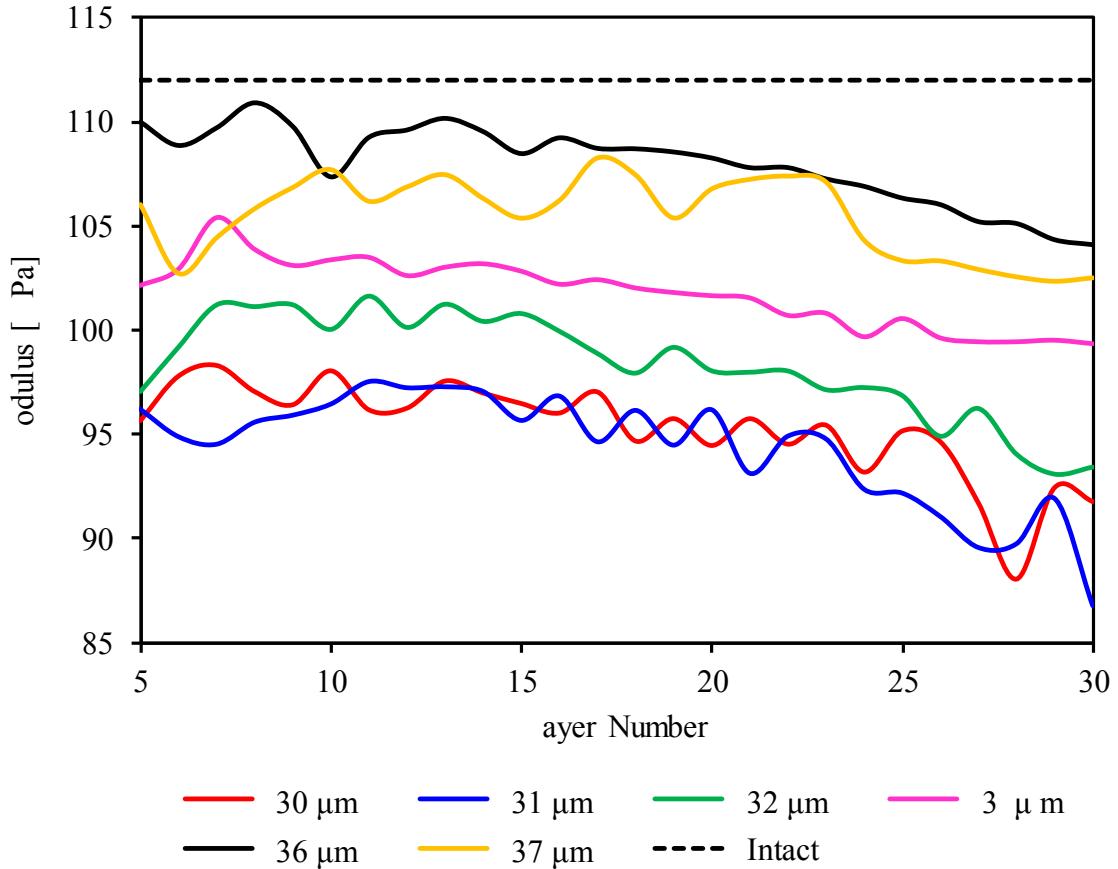


Figure 4.9 Change in UAM stack modulus with layer height and vibration amplitude calculated by a model-based inversion of in-situ monitoring NDE signals

To validate the results from nondestructive evaluation, it is important to verify the results with destructive tests. Push-pin mechanical test has been widely used to evaluate the mechanical strength of UAM components. It involves pushing out a set of UAM layers in a three-point bend configuration. Push-pin specimen and test specifications were derived from Hopkins *et al.* [27]. Two modes of failure are typically observed, first is a premature failure at the base/build interface and second is a failure through a set of UAM layers. The

former is primarily indicative of a poor base/build interface and does not necessarily indicate the quality of the stack. The latter represents the quality of the top few layers of the UAM stack. The different failure mechanisms are well documented in literature. Fig. 4.10 shows the results of push-pin testing. The area under push-pin curves is the mechanical work required to push out a set of UAM layers. This represents the mechanical strength of the component and is combination of shear and tensile loading capability. As the vibration amplitude increases, the area under load-displacement curve increases until an amplitude of  $36\ \mu\text{m}$  and then drastically reduces at an amplitude of  $37\ \mu\text{m}$ . The failure of the  $37\ \mu\text{m}$  component occurred at the base/build interface and is not indicative of the quality of the entire stack. It is clear from these results that the destructive and nondestructive tests are well correlated. Another kind of UAM stack defect is the Type-2 or inter-track defect which occurs between adjacent tracks. Type-2 defects will be discussed in further detail in Sec. 3 where we present a novel method of repairing Type-1a and Type-2 defects in UAM components.

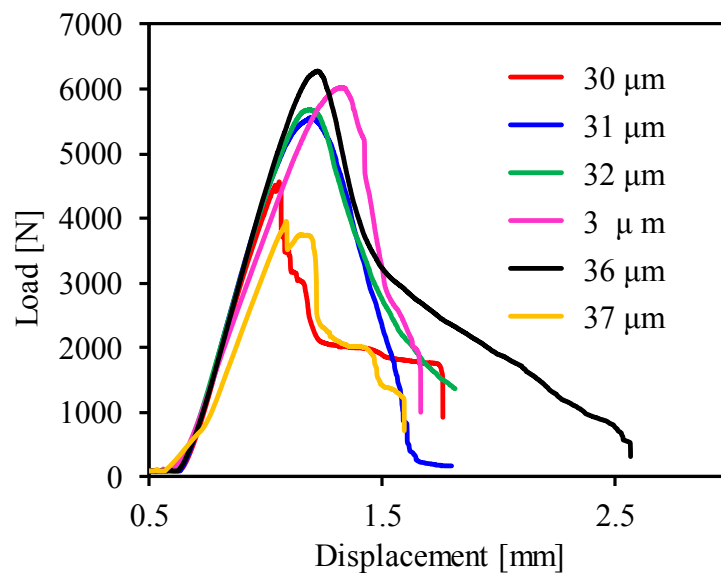


Figure 4.10 Push-pin test results for various vibration amplitudes

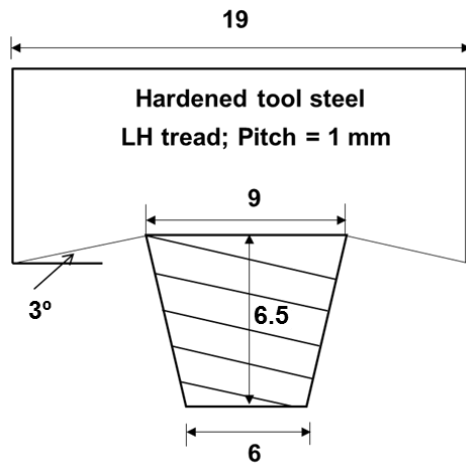
### 4.3 Repairing UAM Defects through Friction Stir Processing

Friction stir processing (FSP) achieves microstructural refinement, densification, and homogeneity using a rotating tool. The microstructure and mechanical properties of the processed zone can be accurately controlled by optimizing the tool design, FSP parameters, and active cooling/heating. The depth of the processed zone can be adjusted by changing the length of the tool pin, with the depth ranging from several hundred micrometers to tens of millimeters. FSP does not change the shape and size of the processed components. For these reasons, FSP is an effective solid-state processing technique for achieving localized microstructural modification in metallic components. UAM distinguishes itself from other additive technologies because of its low temperature solid-state processing. UAM is uniquely suited for producing parts with enclosed internal cooling channels and embedded sensors as well as for producing parts in multi-materials and metal-matrix composites. Even dissimilar metals that are not metallurgically compatible can be combined to produce multi-material parts without embrittlement or cracking. Repairing defects in UAM components using traditional joining methods undercuts the advantages of using UAM. A solid-state processing technique like FSP is an excellent add-on to the UAM process for repairing cracks as well as refining existing microstructures. The two most commonly observed defects in UAM are, base/build interface defects (Type-1a) and inter-track defects (Type-2). FSP can be used to repair defects of both types. Repairing Type-1a defects can be carried out during component fabrication but it requires the removal of the base plate and would require some setup time. Type-2 defects can be healed in between UAM layers by changing the weld head for an FSP tool. Type-1b defects are better addressed by changing the UAM process parameters. The UAM system is well equipped

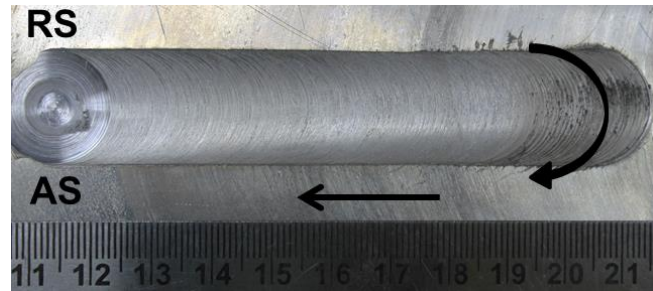
to facilitate tool changes since it utilizes a CNC milling operation between layers. Adding an FSP tool is a low-cost method to heal defects in-situ between layers as and when required. The process parameters utilized during FSP are presented in Table 4.1. Fig. 4.11 shows a schematic of the friction stir tool used in the current study. A UAM sample after FSP is also shown in Fig. 4.11.

Table 4.1 FSP process parameters

FSP Process Parameters				
Rotation speed (rpm)	Traverse feed (mm/min)	Dwell time (sec)	Shoulder plunge (mm)	Tool backward tilt angle (degrees)
1000	10	10	0.2	2



**FSP tool**



**FSPed sample**

Figure 4.11 Schematic of FSP tool and a typical FSPed sample (top view). Arrows show the directions of tool rotation and travel. AS and RS denote the advancing and retreating sides of the processed region

#### 4.3.1 Repairing base/build delamination

UAM components can be manufactured while having a good quality stack alongside a base/build interface delamination as observed in Sec. 2.2. If the UAM stack is the sole component of interest and the base can be discarded after manufacturing, then the repair of the base/build interface is often not required. However, when the base is a part of the component or when the delamination at the base/build interface interferes with satisfactory part fabrication, then repair is required. Base/build delamination also prevents the transmission of ultrasonic NDE signals and hence hinders in-situ monitoring. In-situ monitoring can give indication of Type-1a defects far before they become visible to the naked eye. Fig. 4.12 shows an optical image of base/build delamination that is visible to the naked eye. The cross section shown is made of 80-layer, 11.5 mm thick component built at 32  $\mu\text{m}$  vibration amplitude on a Fabrisonic R7200 UAM system.

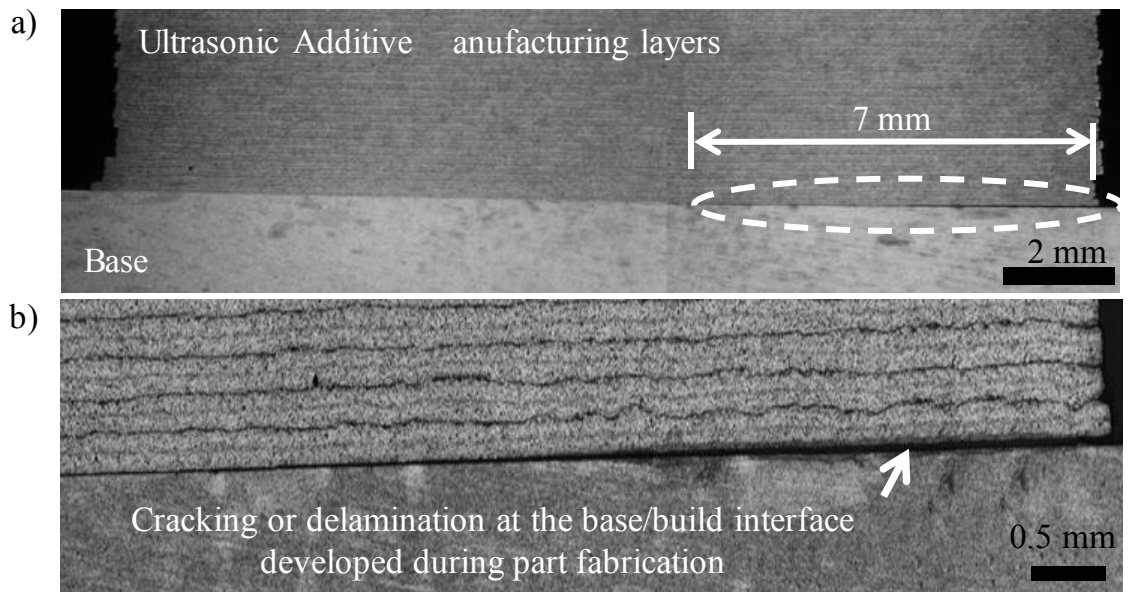


Figure 4.12 (a) Optical micrograph of a UAM build. Encircled region marks a crack at the base/build interface. The crack is shown at a higher magnification in (b)



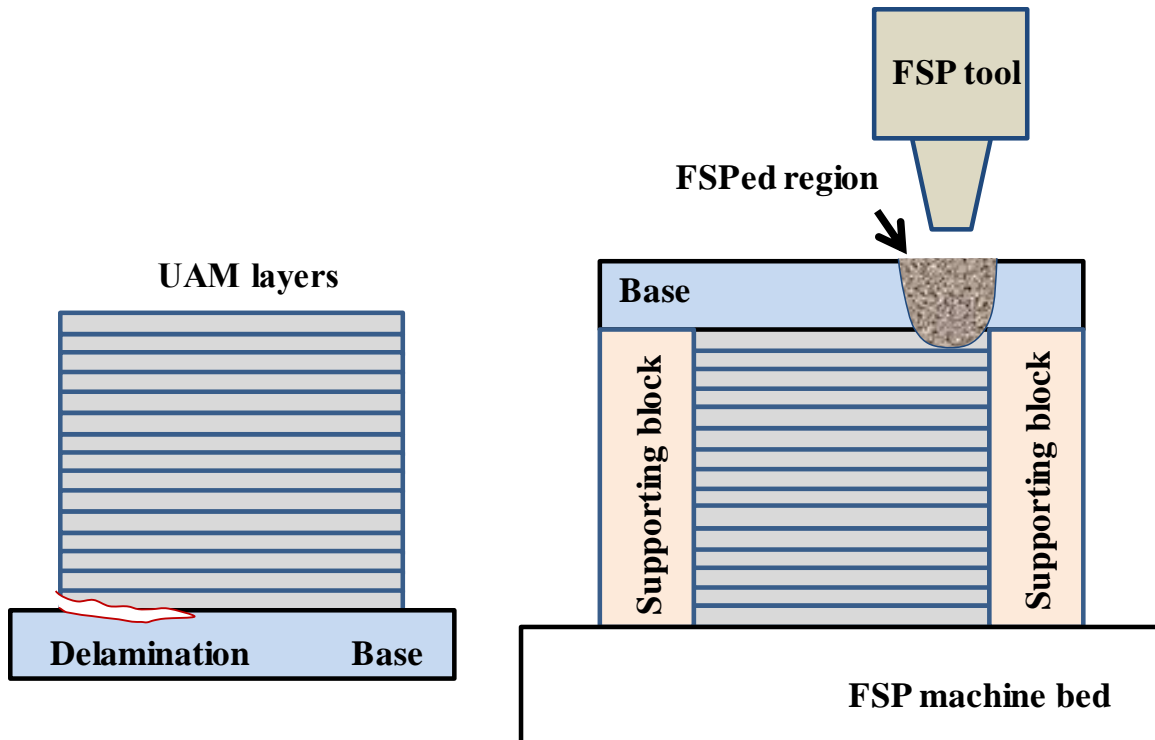


Figure 4.13 Schematic illustration of the use of FSP for healing base/build interface delamination (Type-1a defects)

The same component is also shown in Fig. 4.7 where the reduction in stack quality with layer build-up was discussed. Fig. 4.13 shows a schematic of inverted UAM component with support blocks on either side. The length of tool pin is chosen such that it penetrates through the base and 2 mm (14 layers) into the UAM component. Fig. 4.14 shows the optical micrograph of the cross-section after FSP. The crack developed at the base/build interface is completely healed. The regions marked 1 to 8 represent the interaction of the UAM component and FSP. The enlarged optical micrographs in these regions, clearly indicate the plastic deformation around the rotating tool as seen in Fig. 4.14. Friction stir processing has completely healed the large delamination observed and refined the layered microstructure of the UAM component.

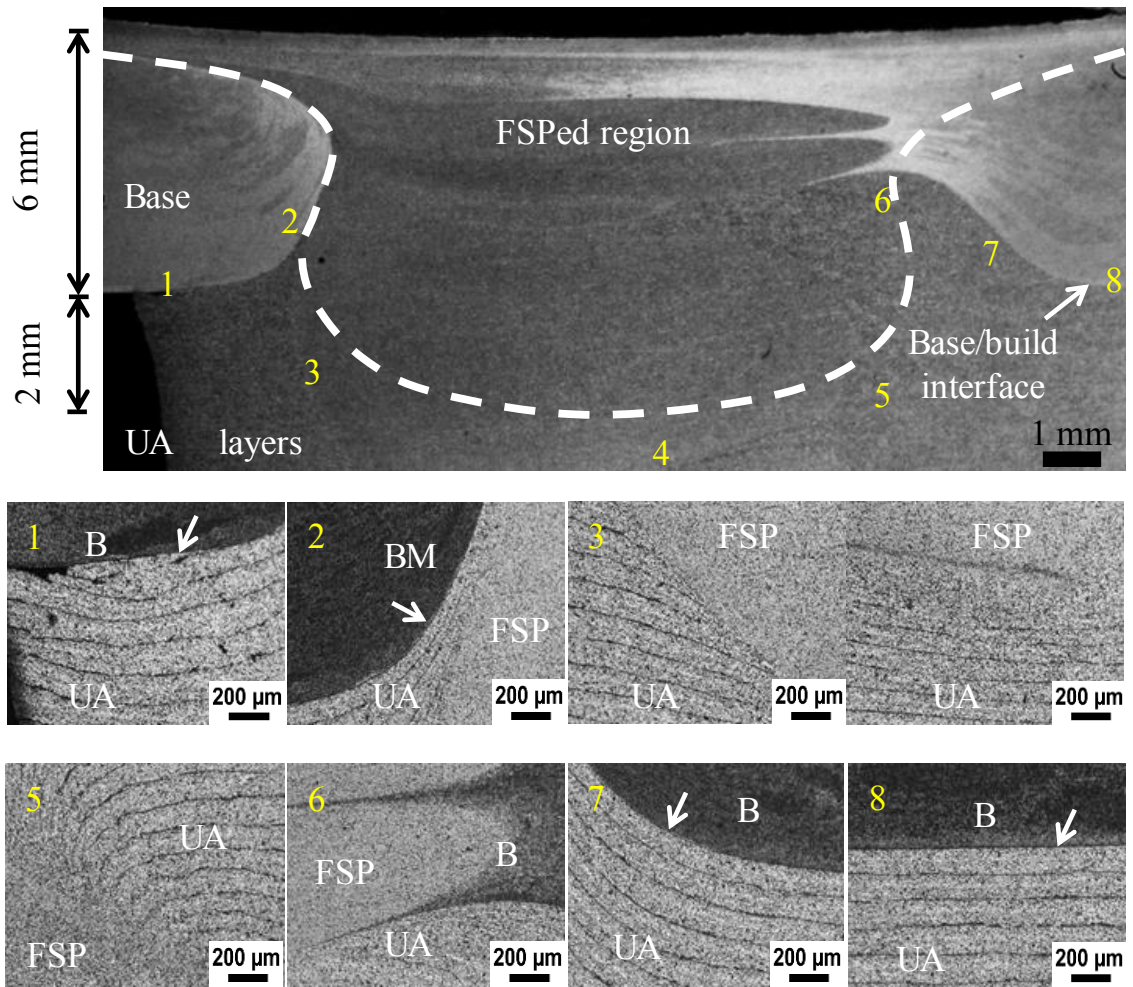


Figure 4.14 Optical micrographs a UAM sample FSPed for repair of a base/build interface (Type-1a) defect. The crack is completely healed by FSP

Even though the delamination is visible to the naked eye, the extent of delamination is unknown, hence we performed acoustic microscopy to look inside the component. After removing from the UAM system the component was immersed into a SONIX acoustic microscope and scanned according to scan parameters discussed in Sec. 2.2 to generate a C-scan reflection image gated at the base/build interface. A color palette was applied for better visualization and Fig. 4.15a shows the delamination visible to the naked eye. Unlike the components seen in Fig. 4.6, the delamination has not propagated all the way to the center and is only on one side. This is because the vibration amplitude is low (32  $\mu\text{m}$ ) and

the amount of power into the component keeps decreasing with layer build-up. This causes the delamination to be localized to one corner of the component. Fig. 4.15b shows the reflection image after FSP processing. The white lines mark the FSPed region. The color palette for the two images is different but the important feature is the contrast between delaminated and well bonded regions. A low amplitude in the reflection image indicates a good bond and thus we can observe from the contrast that the delamination was completely healed in the region where friction stir processing was performed. Two kinds of Type-1 defects have opposing bonding criteria and optimizing UAM process parameters require a balance between the UAM stack quality (Type-1b) and base/build delamination (Type-1a).

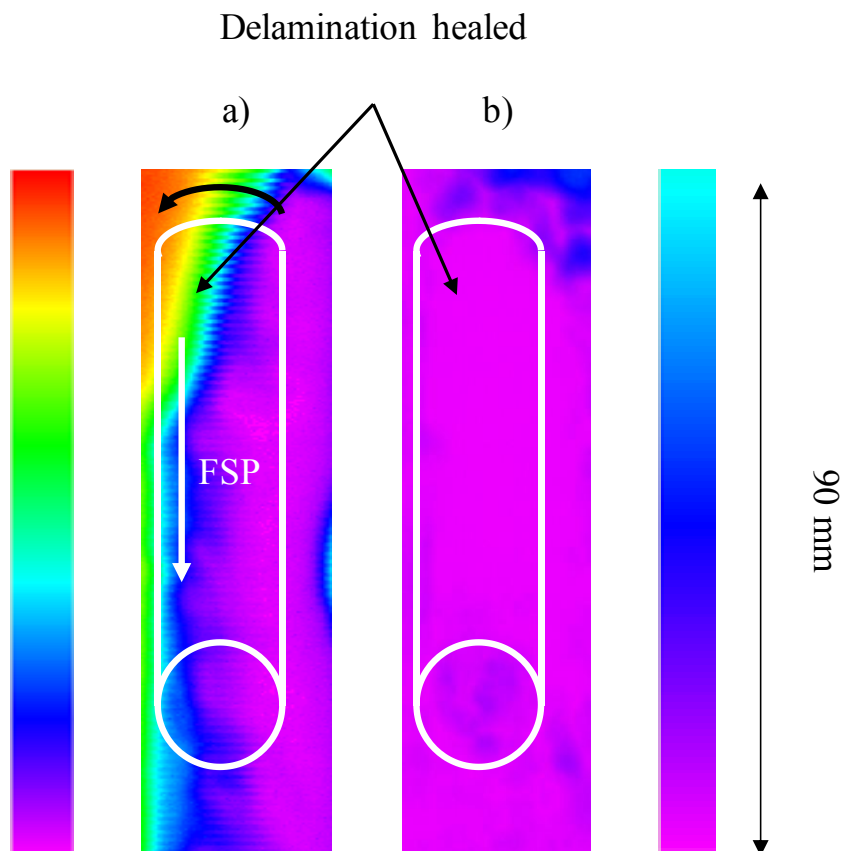


Figure 4.15 Acoustic microscopy images: (a) as-built, (b) after FSP. The color scale of the two images is different with a higher value representing a larger reflection and thus a delamination

### 4.3.2 Repairing inter-track defects

There have been a few attempts in literature to optimize the UAM process for minimizing Type-2 defects [115]. The Fabrisonic R7200 UAM system has a build area of 3.24 m<sup>2</sup> while a single foil width is 25.4 mm. The build height of UAM components is limited when the component consists of a single track. With multiple tracks, the build height can be significantly increased. For these reasons, it is critical to address Type-2 defects. The most typical approach to tackle Type-2 defects relies on changing the overlap between adjacent foils to achieve good inter-track bonding. The mechanism of Type-2 defect formation is through the lack of bond formation between adjacent tracks laid side-by-side. While an overlap region helps to reduce Type-2 defects, it might not entirely eliminate them. To illustrate the working of FSP, a test component of 40 layers and 3 tracks was built to have inter track defects, a typical Type-2 defect is shown in Fig. 4.16.

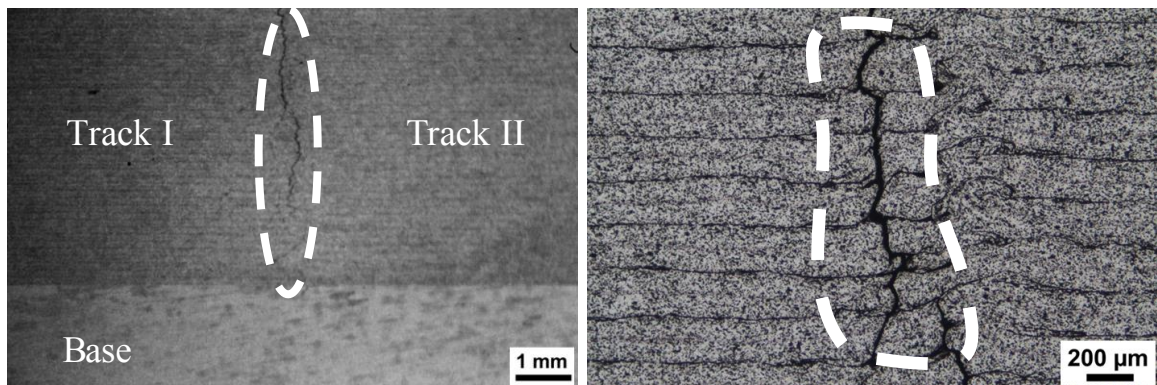


Figure 4.16 Inter-track defects typically found in UAM components

While it is possible to make components with limited Type-2 defects, when hundreds of inter-track regions are present across a large UAM component, it becomes tough to ensure that all the inter-track regions will be perfect. When it comes to Type-1 defects, the bonding mechanism and defect evolution are well understood, and it is possible to expect reasonable bond quality in an amplitude compensated UAM build. With Type-2

defects, the reasonable expectation of bond quality might depend on several localized geometrical factors which are tough to control. This is a limiting factor for making large UAM components for structural applications.

UAM components often have several tracks laid one beside the other to make components larger than 1 inch along the vibration direction. Typically, these tracks have small overlap region to ensure that the tracks laid down beside each other have metallurgical bonding. This overlap region is often prone to crack initiation and propagation. FSP is particularly well-suited to repair inter-track UAM defects. UAM is performed in conjunction with CNC milling wherein the weld head can be replaced with a CNC tool for machining components to a required dimension. This makes it possible to incorporate an FSP tool that can be programmed to move according to the existing CNC infrastructure. This provides the chance to repair inter-track regions after every few layers. Fig. 4.17 shows the schematic of repairing UAM Type-2 defects using FSP.

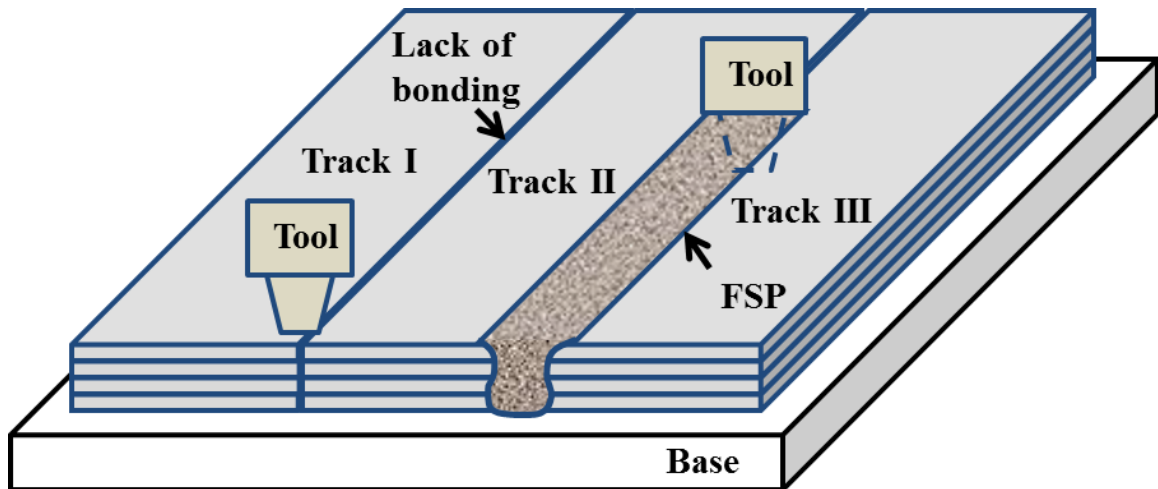


Figure 4.17 Schematic illustration of the use of FSP for repair of Type-2 defects in UAM parts

Fig. 4.18 shows the optical micrograph of the cross-section after FSP. The crack developed between the two adjacent UAM tracks is completely healed. The regions marked 1-8 represent the interaction of the UAM component and FSP. The enlarged optical micrographs in these regions, clearly indicate the plastic deformation around the rotating tool and show that the Type-2 defect is completely healed as seen in Fig. 4.16.

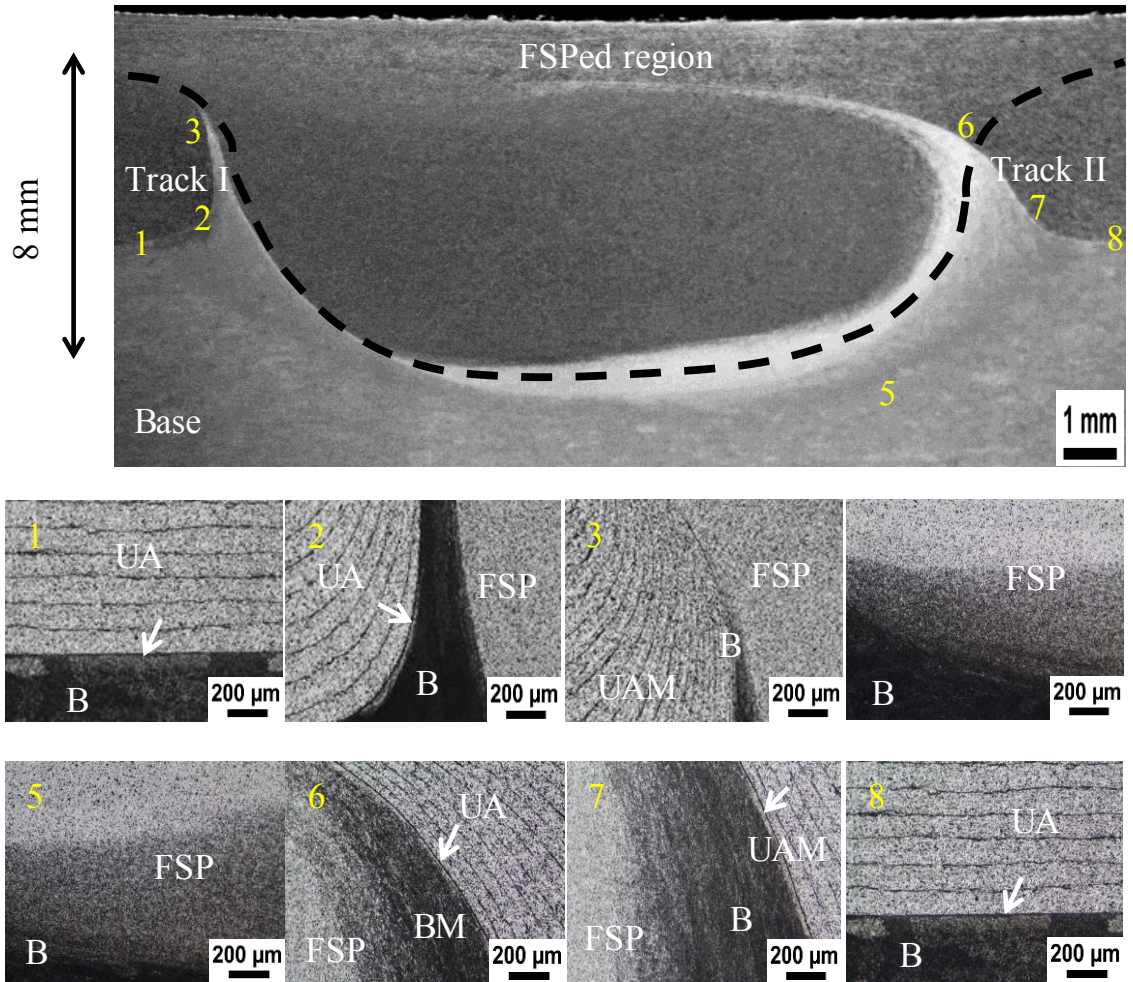


Figure 4.18 Optical micrographs of a UAM sample FSPed for repair of a Type-2 defect. The defect is completely healed by FSP

It can be observed that the inter-track defects as well as base/build delamination were entirely healed and the region where the process was performed had a homogenous quality throughout. Even if there is no clear indication of cracking, FSP of inter-track

regions offers a microstructural and mechanical improvement in quality due to solid-state processing. There are several advantages of using FSP as a complimentary repair mechanism specifically to heal existing inter-track defects as well as to improve the quality of inter-track regions. FSP offers the unique advantage of being able to control the tool depth and thus the processing zone. A change in tool width is also possible which can be used on the complex geometries common in UAM. The results demonstrate the use of FSP tool with UAM as the primary bonding mechanism and FSP as a repair and refinement mechanism to be utilized in specific regions where the quality of components can be improved.

#### 4.4 Conclusion

The current study is aimed at developing methods for monitoring and repair of defects in UAM. Defects in UAM are classified into two kinds namely, Type-1 and Type-2. Type-1 defects are further divided into Type-1a and Type-1b defects. Type-1a defects occur at the base/build interface while Type-1b defects are inter-layer defects that occur at other locations within the UAM stack. Type-2 defects also occur within the stack but between two adjacent UAM tracks. Ultrasonic NDE is well suited for monitoring UAM defects. An in-situ continuous online monitoring ultrasonic NDE setup was designed and installed on a Soniclayer R7200 UAM system. Ultrasonic A-scan data was collected before, during and after each layer. A two-parameter wave propagation model previously developed in [117] was used to study the interaction of ultrasonic waves with UAM components. Each UAM interface between neighboring layers was modeled as an interfacial spring. Two independent stiffness coefficients are necessary to model wave

propagation are base/build interface ( $\eta_1$ ) and bulk stack stiffness ( $\eta$ ). A bond quality inversion methodology was used for continuous quality evaluation. Both kinds of Type-1 defects were measured which allows the understanding of the mechanism of evolution of Type-1 defects in UAM.

Acoustic microscopy (offline NDE) was utilized to map base/build interface delamination. The geometry of the component, location on base substrate and its dimension play a significant role in the initiation and propagation of this delamination. Among all the interfaces, the base/build interface is especially prone to delamination since it acts as a stress concentration during vibration. Ultrasonic NDE provides a physical visualization of the delamination which could be more catastrophic than is observable through visual examination. The mechanism of formation and evolution of Type-1a defects was proposed based on NDE results. Three kinds of Type-1a defects were identified and the reasons for formation of these defects were discussed.

UAM stack quality was also studied and the reduction in quality with layer build up was quantified. Type-1b defects form within the stack either due to low or excessive power input. Based on laser vibrometer studies, the UAM sonotrode in a Fabrisonic R200 research machine was calibrated. The DUKANE iQ welding controller maintains the average vibration amplitude close to the setpoint (1 % s.d.) in free air and during welding. Hence it becomes clear that with increasing build height, given that the amplitude at the sonotrode remains the same, less power is transmitted into the UAM weld. The average power drawn by the ultrasonic horn for various amplitude settings was presented which shows a decreasing trend as expected. These results agree with the UAM stack modulus measured by the in-situ monitoring setup. Type-1b defects of two kinds were examined.



The defects caused by lower power are a systemic problem in UAM components and can be remedied by amplitude compensation with build height. Higher power input leads to a disruption of previous layer bonds and hence inter-layer defects.

Based on our understanding of the UAM defect evolution, Friction Stir Processing (FSP) was presented as a novel in-situ repair and refinement tool for UAM components. While inter track defects are repaired from the top of UAM stack, base/build delamination is repaired from below the base. To illustrate the working of FSP, a test component of 40 layers and 3 tracks was built to have inter track defects. Another test component was built with single track stacked with 80 layers and had base/build delamination. Friction Stir Processing repaired the defective zones in both test components as observed through optical and acoustic microscopy. There are several advantages of using FSP as a complimentary repair mechanism specifically to heal existing inter-track defects as well as to improve the quality of inter-track regions. While further research is required to justify the use of FSP for complex shaped UAM components, the results of this work lay the foundation for incorporating FSP into the UAM process.

CHAPTER 5  
ULTRASONIC NONDESTRUCTIVE EVALUATION AS A PROCESS PARAMETER  
DEVELOPMENT TOOL FOR LASER POWDER BED FUSION ADDITIVE  
MANUFACTURING<sup>4</sup>

### 5.1 Introduction

Laser Powder Bed Fusion (L-PBF) is a prominent metal additive manufacturing technology for making functional components in various materials. The quality of L-PBF components depends on several factors including laser power, scan speed, hatch spacing, layer thickness, particle shape/size distribution and other build conditions. Developing process parameters for a new material is an expensive, time consuming and complex optimization problem which typically involves the manufacture of several coupons, test bars to characterize the relationships between the build conditions and L-PBF part quality. In this study, we propose using ultrasonic nondestructive evaluation to evaluate a wider range of process parameters and narrow the optimal range based on process-structure-property correlations. Ultrasonic in-situ monitoring of L-PBF has been explored by Rieder *et al.* [90,91]. Their system has the ultrasonic transducer below the base plate. This is in contrast with other online monitoring systems including laser ultrasonics [92],

---

<sup>4</sup> This chapter has been prepared as a manuscript to be submitted to *Additive Manufacturing* (2018). All permissions to use this paper as a part of this dissertation are contained in the Appendix.

thermography [85], x-ray, and eddy current measurements [86, 89] all of which are performed from above. Ultrasonic monitoring from below the base can only be used on regular shaped components with the component firmly attached to the base, i.e. with no support structures. It is not a viable tool for in-situ monitoring of complex shaped AM components, but it offers the advantage of being sensitive to macro- and microstructural changes. Rieder *et al.* [90] have shown that in-situ pulse-echo ultrasonic NDE can detect poor regions sandwiched between good quality regions. A porosity estimation was also proposed based on the reflection from high porosity zones or the calculation of ultrasonic velocity. AM components offer some challenges towards in-situ inspection due to inter-layer defect formation. In a typical metal AM component, using a 10 MHz ultrasonic transducer, the largest size of the defect that can be resolved is half the wavelength ( $\lambda/2 \sim 0.3$  mm). Defects much smaller than that provide indications in the ultrasonic velocity and attenuation. Estimation of ultrasonic velocity is typically performed by the means of time of flight or phase delay calculation. When a new defective AM layer is added to an existing component, the layer thickness of 50  $\mu\text{m}$  is an order of magnitude smaller than the wavelength of a typical 5-10 MHz ultrasonic wave. While the individual defects cannot be resolved, the boundary of a defective layer has partial reflection and transmission. After sufficient number of layers accumulate, the reflection from the defect can cause a constructive or destructive interference with the signal from the top of the stack. This behavior might lead to spurious phase and time of flight calculations. Hence, the most important consideration during in-situ ultrasonic NDE, is the interference of ultrasonic waves from within the AM sample with those from the top of the AM stack. Studying these interference effects is a complex problem and requires a modeling approach.

In Nadimpalli *et al.* [117], we proposed a finite interfacial spring stiffness model to characterize layer defects in Ultrasonic Additive Manufacturing (UAM) components. This approach proved to be useful to separate the interference effects with the help of a model-based inversion of bond quality. Finite interfacial stiffness springs proposed by Baik and Thompson [38] are used in the ultrasonic NDE literature to characterize imperfect layers of defects. Zone II defects typically occur via three mechanisms. The first is keyhole defect that occurs at a certain depth inside the weld track [124]. The second occurs when particles which get thrown away from the melt pool and get remelted and solidify on top of the weld [86]. The third is when the recoater blade removes these spherical particles and causes the formation of pits [70, 71]. Each of these mechanisms causes defects at certain heights within the component which might be considered as a layer of defects. Zone III defects occur due to partially sintered or unmelted powders caused by insufficient energy input. These defects can be also considered as a layer of defects. Even if Zone II and Zone III defects are stochastic, for modeling wave propagation, a layer-spring model can be considered. The defects in AM components can be represented by an equivalent layer-spring system under the influence of ultrasonic vibration. The thin defective layer is characterized as an imperfect interface which is a massless finite interfacial stiffness spring. Fig. 5.1a shows the layer spring model where  $\kappa$  is the interfacial stiffness and  $d$  is the layer thickness. A quality parameter  $\eta$  is a dimensionless stiffness coefficient defined as

$$\eta = \kappa d / C_{11} \quad (5.1)$$

Ultrasonic wave propagation through the layer-spring model is achieved through impedance translation [117]. The homogenized Young's modulus of an Inconel 625 A component with number of layers ( $N$ ) whose total height ( $l \gg \lambda$ ) is calculated and

presented in Fig. 5.1b. The model is used to calculate the elastic stiffness coefficient ( $C_{11}$ ) and thus estimate Young's modulus ( $E$ ) according to Eq. (1.3). When the quality parameter  $\eta < 1$ , the modulus is less than half the nominal value and is considered poor quality. When  $\eta = 10$ , the modulus approximately is 90 % that of a fully dense component. For  $\eta > 100$ , the modulus is close to 100 %.

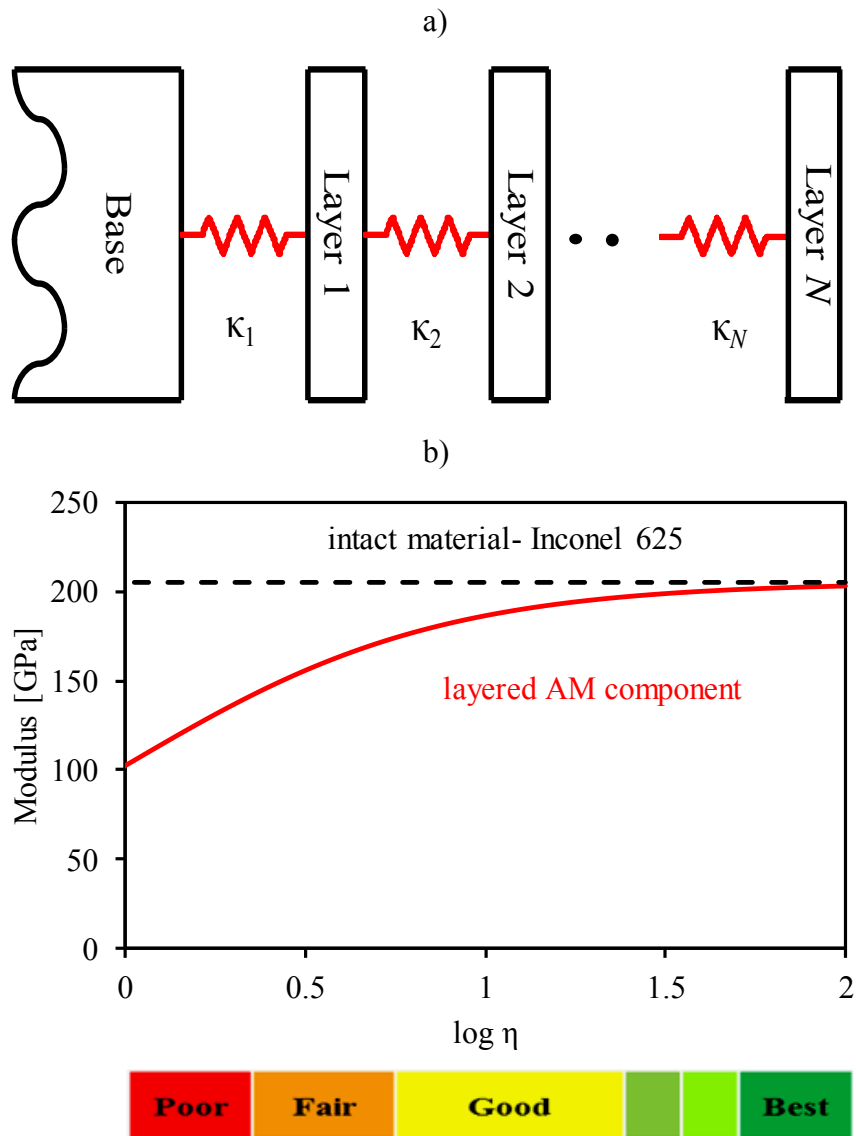
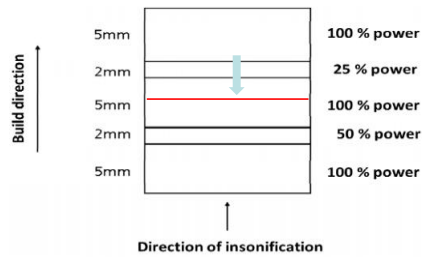


Figure 5.1 a) AM interfaces are modeled as spring stiffnesses b) Change in modulus with interfacial stiffness coefficient ( $\eta$ ) which is a dimensionless quality parameter

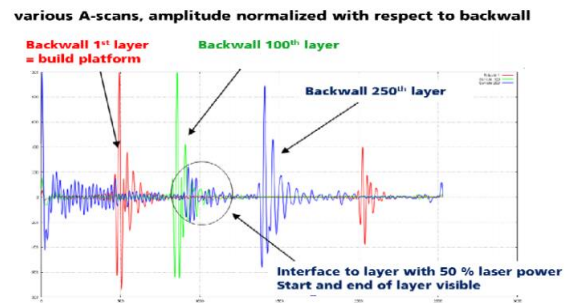
The quality parameter scale can now be used to characterize individual layers during in-situ monitoring. This approach is a forward model since we assume the quality of the layer and then calculate the output ultrasonic signal in the time domain by means of an inverse Fourier transform.

We take the example presented in Rieder *et al.* [90], to demonstrate the working of the forward model, in which 2 mm of defective zone is embedded between good quality layers of an Inconel 718 component. In-situ ultrasonic NDE signals along with the process parameters of L-PBF are shown in Fig. 5.2. To simulate the first 10 mm of this AM component, we use the quality parameter  $\eta = 50$  for the first 5 mm,  $\eta = 1$  for the defective 2 mm, and  $\eta = 50$  for the next 3 mm. The total number of layers is thus 250 with the layer thickness being  $0 \mu\text{m}$ . The red signal seen in the experiment is captured only on the base with no AM component while the blue signal is captured after 250 layers have been deposited on the base. As the ultrasonic waves travel through this AM component of 250 layers, we observe a reflection echo from the beginning and the end of the defective 2 mm region. These echoes are separated because the wavelength of 10 MHz ultrasonic signal is 0.6 mm. In the signal from the experiment, energy loss occurs through diffraction and attenuation as the wave travels through the sample. Part of the attenuated signal gets reflected to the transducer. In the simulated signal, energy loss occurs due to the partial transmission at the interface between the layers. To better simulate the diffraction and attenuation loss, the interfacial stiffness is considered as a complex number with a small imaginary component.

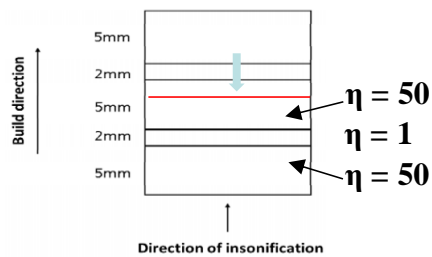
## Experiment



a)



## Simulation



b)

Input waveform      Output waveform

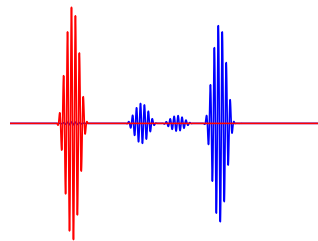


Figure 5.2 a) In-situ monitoring of IN-718 with varying laser power taken from Reider *et al.* [90, 91], b) Simulation of ultrasonic wave propagation through AM component shows the experimentally observed signal features

The experimental and simulation signals from Fig. 5.2 show the separation of the echoes from the defective region after sufficient number of layers have been built on top. The challenge for in-situ ultrasonic NDE is that as defective layers are being added, the signal from the top of the AM stack interferes with the signals from within the AM component. This issue is especially prevalent at the base/build interface because there is often an impedance mismatch between the base and the AM component. The impedance mismatch leads to a reflection echo from base/build interface even if the interface has excellent quality. Hence, there is an interference during the first few mm of in-situ

monitoring. It was observed that the phase velocity during in-situ monitoring reduced by 15% even though the AM component was fully dense. Rieder *et al.* [90, 91], proposed that the reduction in velocity might be due to the heat build-up within the sample. Several studies [84, 88] have demonstrated using thermocouples, that the average temperature measured on the base is typically under 100 °C. Considering the thermal conductivity of the material and the fact that the coupon was firmly bonded to the base, it is conceivable that the coupon temperature is close to the ambient base plate temperature. The change in ultrasonic velocity in Inconel 718 with the 100 °C change in temperature cannot cause >10% change in ultrasonic velocity. Hence, there must be some other reason for this behavior. To investigate further, we use our model to simulate a typical AM component on top of a base. It is useful to model AM components with two independent parameters namely,  $\eta_1$  for base/build interface and  $\eta$  for quality of the rest of the stack.

Fig. 5.3a shows the simulation results for a good quality stack with an impedance mismatch at the base/build interface. A random quality change in  $\eta$  is introduced to simulate experimental signals since each layer will not be the same. The output simulation (blue) has a small reflection at the base/build interface and even smaller reflections throughout the AM stack. The layer-by-layer phase velocity of the simulated signals is shown in Fig. 5.3b plotted on the same scale as experimental velocity. We can observe the reduction in phase velocity in the first few mm of the AM build, and the zig-zag pattern in the velocity later both occurring due to interference effects. This is a much more plausible explanation of the experimentally observed phenomenon. Another factor which might have caused the reduction could be a change in coupling medium due to rise in temperature.



Based on the simulation results, a decrease in phase velocity in the first few mm is expected due to interference effects.

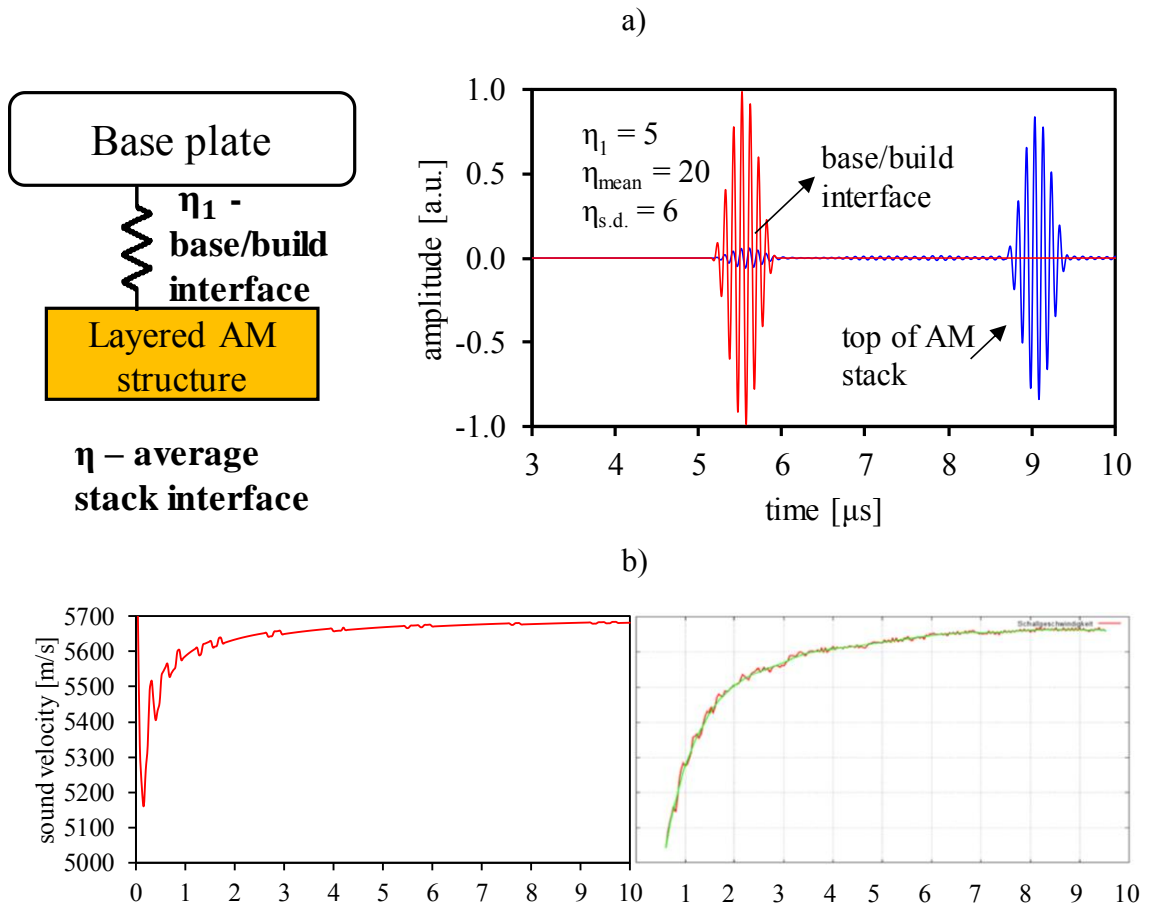


Figure 5.3 a) Simulation of ultrasonic wave propagation through an AM structure, b) Comparison of phase velocity calculated from simulation on left and from experiment on the right published in Reider *et al.* [91]

Since interference effects are a concern, it is important to have a model-based quality evaluation while estimating the elastic stiffness from ultrasonic velocity. Hence, a layer-by-layer bond quality inversion methodology is required. A two-parameter inversion technique was previously proposed and demonstrated for UAM components [117]. The method is explained below briefly and the readers are directed to Nadimpalli *et al.* for

further details. Using in-situ continuous ultrasonic monitoring, a time-averaged A-scan signal can be collected after bonding each layer. With the deposition of a layer, the A-scan signal shifts in time. The signals collected after each layer can be compared to the reference signal which has only the base. The phase velocity and attenuation of ultrasound within the AM component are used to estimate the average elastic stiffness ( $C_{\text{stack}}$ ) and dispersive impedance of the AM stack. Then the quality of the newly deposited  $N^{\text{th}}$  layer ( $\eta_N$ ) can be calculated as

$$\frac{N}{C_{\text{stack}}} = \frac{1}{C_{11}} \left( \frac{1}{\eta_1} + \frac{1}{\eta_2} + \dots + \frac{1}{\eta_N} \right) + \frac{N}{C_{11}}, \quad (5.2)$$

where  $C_{11}$  is the elastic stiffness coefficient of the layered material. The inversion is iteratively performed until convergence is achieved for the quality of the newly deposited layer. This methodology does not eliminate the interference effects, but it can identify good-quality layers hidden behind poor-quality layers by accounting for the interference. To account for the differences between UAM and L-PBF components, an improved inversion is proposed, which divides the AM component into two groups, first from layers 1 to  $N-5$  and second consisting of the top 5 layers. This approach helps in arriving at updated quality estimates for the last 5 layers since those are the layers which potentially get re-melted and whose quality is subject to change. The quality of the AM stack below a depth of 5 layers is assumed to remain constant. This approach is in contrast with the inversion presented in Nadimpalli *et al.* [117]. In UAM components, the base/build interface quality can change over time. In L-PBF components however, it practically remains unchanged after 5-10 layers are built on top. In the new inversion methodology, a matrix of  $\eta$  values for each layer are estimated starting from the first layer. Once the current layer  $N$  is more than 5 layers away from a layer whose stiffness has been calculated, that

value doesn't change. This inversion method is efficient and is well suited for the L-PBF in-situ monitoring.

## 5.2 Design of Experiment

Design of an in-situ ultrasonic NDE sensor setup requires an open architecture L-PBF system to install the sensor. Hence, we collaborated with Advratech, that designed and built such a L-PBF system. The purpose of this test bed is to be a research tool to allow easy study and development of the L-PBF processes. The test bed has far greater flexibility to adjust and measure key process variables than any commercially available AM machine. It consists of a two-platter system, one as a reservoir of supply powder and the other as a build area. A powder spreading blade transfers thin layers of metal powder  $\sim 50 \mu\text{m}$  thick, to the build area where the laser melts the powder in the desired location to add to the part being fabricated. The remainder of powder is swept off and recycled. The platters and spreading mechanism are driven by linear actuators, and controller software. The laser source is an IPG fiber laser (500W YLR-500-SM). The laser beam is guided over the build area by Direct Machining Control software and a ScanLabs galvanometer scan head. The test bed is controllable and programmable through a desktop computer. The size of the build volume is approximately  $100 \text{ mm} \times 100 \text{ mm} \times 100 \text{ mm}$ , and the entire test bed is housed in an atmospheric chamber equipped with oxygen sensors. During processing, the chamber is filled with an inert gas, such as argon, to prevent oxidation during the build process. The test bed also has a suite of sensors including a laser profilometer, high speed camera, IR camera and spectrometer. In this study, we present data only from an in-situ ultrasonic NDE sensor. Ultrasonic monitoring from below the base is ideal for process parameter

development of regular shape components. A high temperature adhesive couplant was used to bond a 5 MHz delay line, dual element, high temperature (up to 600 °C) ultrasonic transducer onto an Inconel 625 base plate.

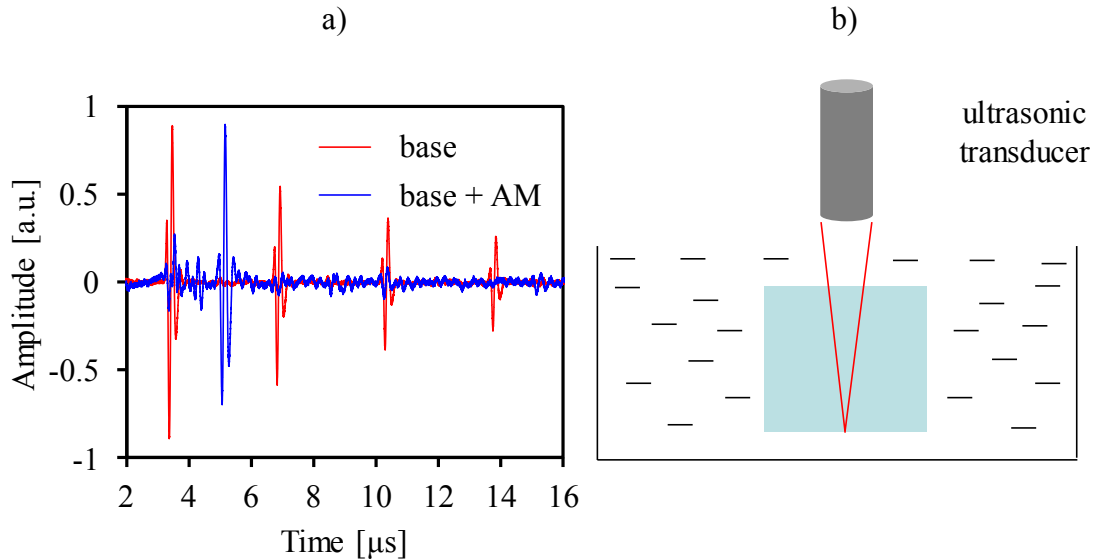


Figure 5.4 a) Ultrasonic response of an IN 625 AM component (5 mm) attached to an IN 625 base (10 mm). b) Acoustic microscopy of a coupon that has been removed from the base

Inconel 625 was chosen because access to coupons manufactured on an EOS M270 SLM, L-PBF system were available for comparison. Dilip *et al.* [72], showed that at a laser power of 195 W, components made with energy density (as defined by Eq. (1.1))  $< 100 \text{ J/mm}^3$  have Zone III (under-melting) defects while energy density  $> 150 \text{ J/mm}^3$  leads to Zone II (over-melting) defects. The IN 625 coupons of varying quality were immersed in a SONIX acoustic microscope and scanned using a focused 20 MHz transducer. A typical signal from a 5 mm x 10 mm x 10 mm coupon attached to a base plate is shown in Fig. 5.4a. The base/build interface and the signal from the top of the stack are clearly distinguishable. The latter signal is gated, and an image is formed by scanning across the

other two axes at a resolution of 100  $\mu\text{m}$ . A schematic of the acoustic microscopy setup is shown in Fig. 5.4b where the transducer is focused at the bottom of the coupon.

The acoustic microscopy images along with the corresponding optical microscopy images (from Dilip *et al.* [72]) are shown in Fig. 5.5. Based on these results, an energy density of 125  $\text{J}/\text{mm}^3$  appears to be ideal for manufacturing fully dense components. One of the objectives of this work is to determine if ultrasonic NDE can detect well bonded regions hidden behind poor-quality zones. For this purpose, the experiment was designed to have 100  $\text{J}/\text{mm}^3$  for the first 60 layers, followed by 66  $\text{J}/\text{mm}^3$  for 10 layers and 125  $\text{J}/\text{mm}^3$  for 0 layers. The scan speed (1 m/s), hatch spacing (60  $\mu\text{m}$ ) and layer thickness (50  $\mu\text{m}$ ) were kept constant while the laser power was varied from 200-375 W to change the energy density.

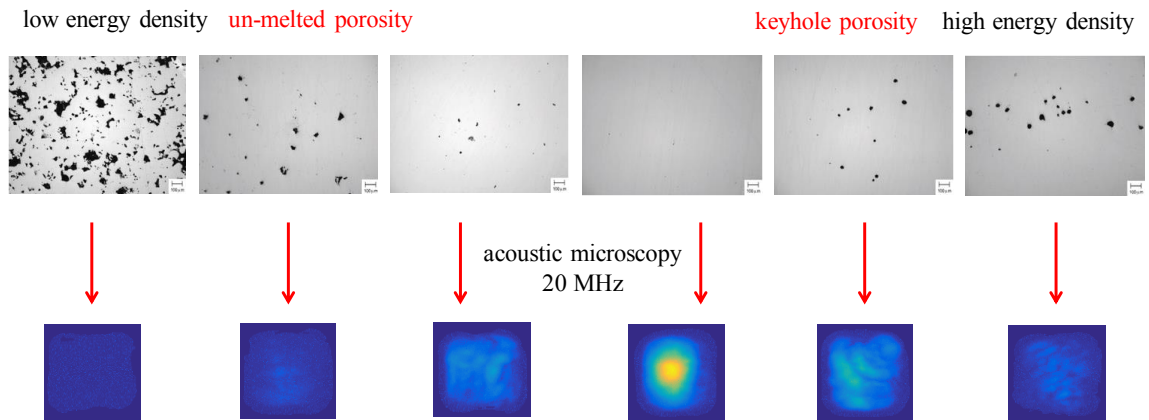


Figure 5.5 Optical microscopy images from Dilip *et al.* [72] and corresponding acoustic microscopy images from a focused transducer. The coupons were approximately 5 mm x 5 mm x 5 mm cubes cut out for performing optical microscopy

### 5.3 In-situ Bond Quality Evolution

The Inconel 625 sample with 3 distinct regions was built on the Advratech test bed while ultrasonic in-situ continuous monitoring was performed. A JSR ultrasonics remote pulser-receiver board has a pulse repetition frequency (PRF) up to 20 kHz along with an 8-bit, 1.5 GHz A18xGTE data acquisition card. For this study a PRF of 5 kHz with a sampling rate of 750 MHz was used, which gives  $< 2$  ns resolution. Several gigabytes of signal raw data were stored in a computer. Though it was possible to perform the data analysis in real time, in this study it was performed post manufacturing. The 5.5 mm x 20 mm x 20 mm coupon built on a 10 mm IN 625 base plate was EDM wire cut into 4 parts such that the base and AM component are attached to each other.

These components were then imaged using a stereo microscope. Fig. 5.6 shows the three distinct regions in the component. The first 60 layers with energy density of  $100 \text{ J/mm}^3$  show several small porosities. The next 10 layers show large unmelted regions as expected. The last 40 layers are built using an optimal energy density and the component appears to be close to 100 % dense. The red square regions indicate locations that were chosen for closer examination in an optical microscope. While sectioning, grinding, and polishing IN 625 is straightforward, revealing the microstructure requires longer etch time due to the corrosion resistance of the alloy. A combination of 15 ml HCl, 10 ml acetic acid and 10 ml  $\text{HNO}_3$  is used by swabbing up to several minutes.

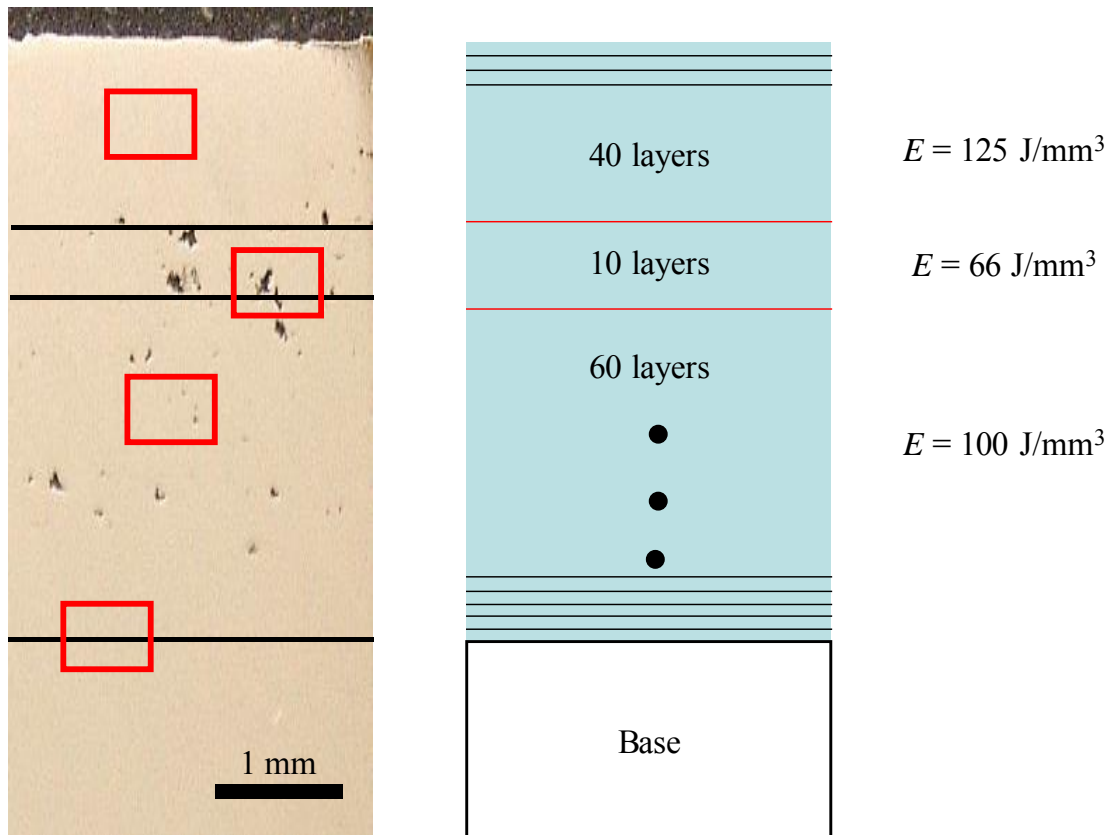


Figure 5.6 Schematic of Inconel 625 L-PBF fusion component with varying quality on the right and an optical macrograph on the left. The red squares indicate regions used for microscopy

The etched microstructure of the four regions in Fig. 5.6, from bottom to top are shown in Fig. 5.7a to 5.7d respectively. Fig. 5.7a shows the base/build interface microstructure. The base has a wrought structure with carbide phase particles. The etching time was not sufficient to further expose the twin and triple point grain boundaries that are sparsely observed. In the AM structure, the overlapping laser tracks are clearly visible. The melt pool depth seems to be  $\sim 100 \mu\text{m}$  which is two layers thick. The melt pool width is also around twice the hatch spacing. The microstructural features within the AM component are not easy to recognize. Elongated grain growth along the build direction can be observed. Fig. 5.7b and 5.7c are regions with defects. The scan lines are visible,

revealing the melted and re-melted boundaries during L-PBF processing. Fig. 5.7d is from the top 40 layers with well bonded layers. Due to the higher energy density, the melt pool depth is larger. Even though the density of the component is high, there are small micro porosity defects even at an energy density of  $125 \text{ J/mm}^3$ . Fine dendritic structure within the grains was observed from all the locations inside the AM component. The Vickers microhardness was measured at several points on the base and the alloy. The base plate has an average hardness of 243 HV with an error of  $\sim 5 \text{ HV}$ . The AM component has an average hardness of 333 HV with an error of  $\sim 8 \text{ HV}$ . The L-PBF components have a much higher hardness compared to the base material. This is due to the high solidification rates leading to fine grained microstructure.

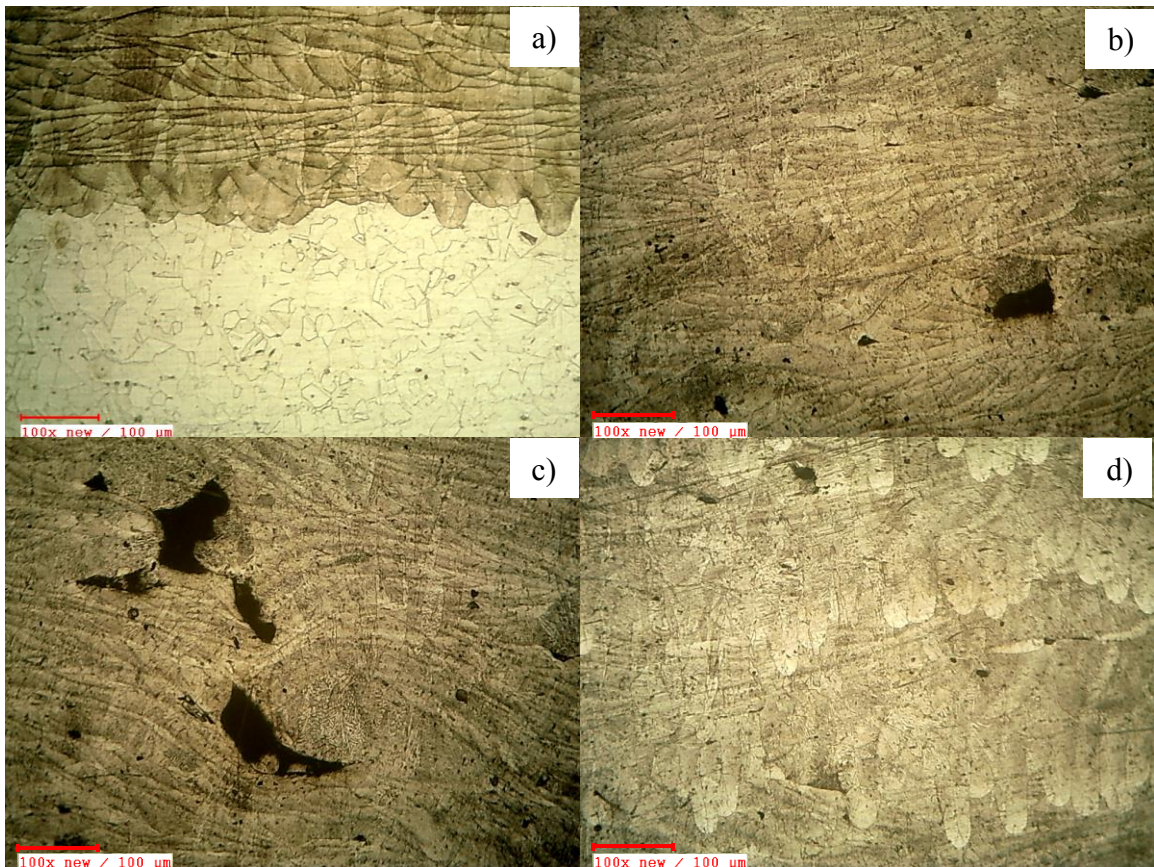


Figure 5.7 Optical micrographs of etched IN 625 L-PBF components at, a) base/build interface, b) within first 60 layers, c) between 60-70 layers, d) between 80-100 layers



Based on optical microscopy examination, it is evident that the quality of the component is as expected based on the energy density. Fig. 5.8 shows the ultrasonic signals captured in-situ, as more layers are built, the signal from the top of the stack shifts in time. We found that calculating the ultrasonic velocity was challenging after layer 60 due to interference and loss of signal amplitude within the AM specimen. A moving gate that was manually selected for each layer, was used to calculate the phase velocity and attenuation. If the component does not have as many defects, then the manual gating is not necessary. The main result from the inversion model is the average quality parameter of the AM stack, from which the individual layer quality can be estimated. Fig. 5.9 shows the average  $\eta$  with increasing layer number.

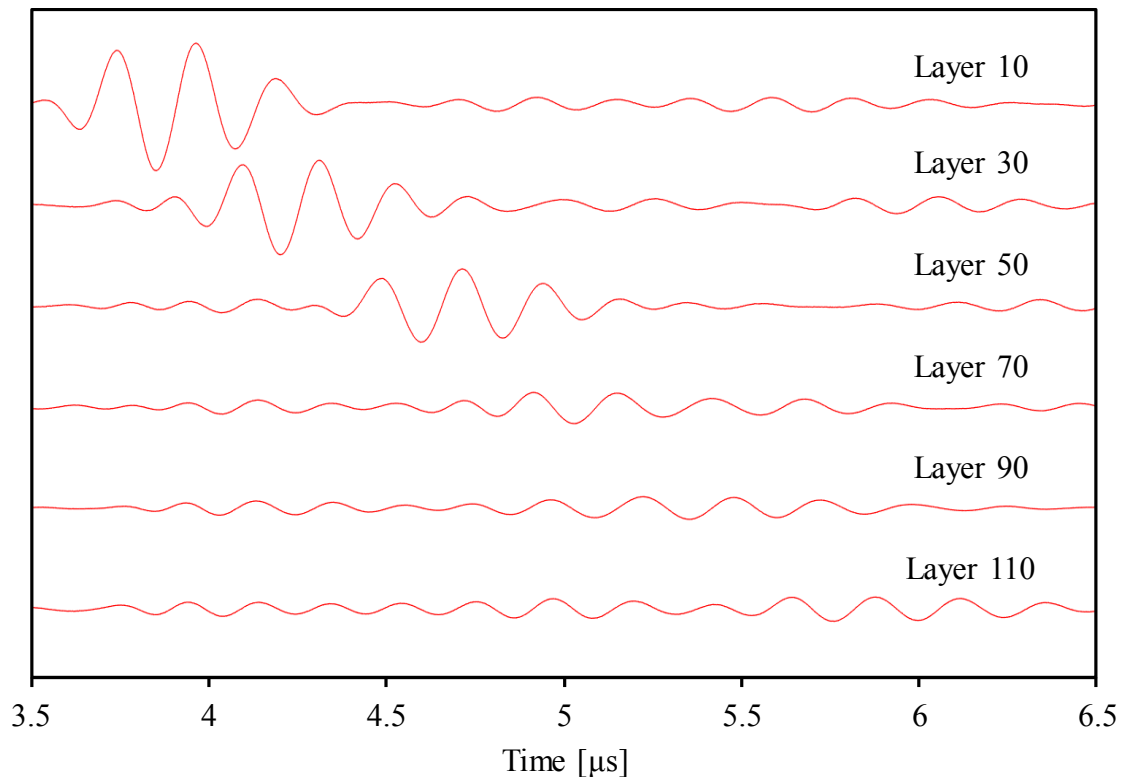


Figure 5.8 In-situ ultrasonic NDE signals after building several layers of L-PBF component

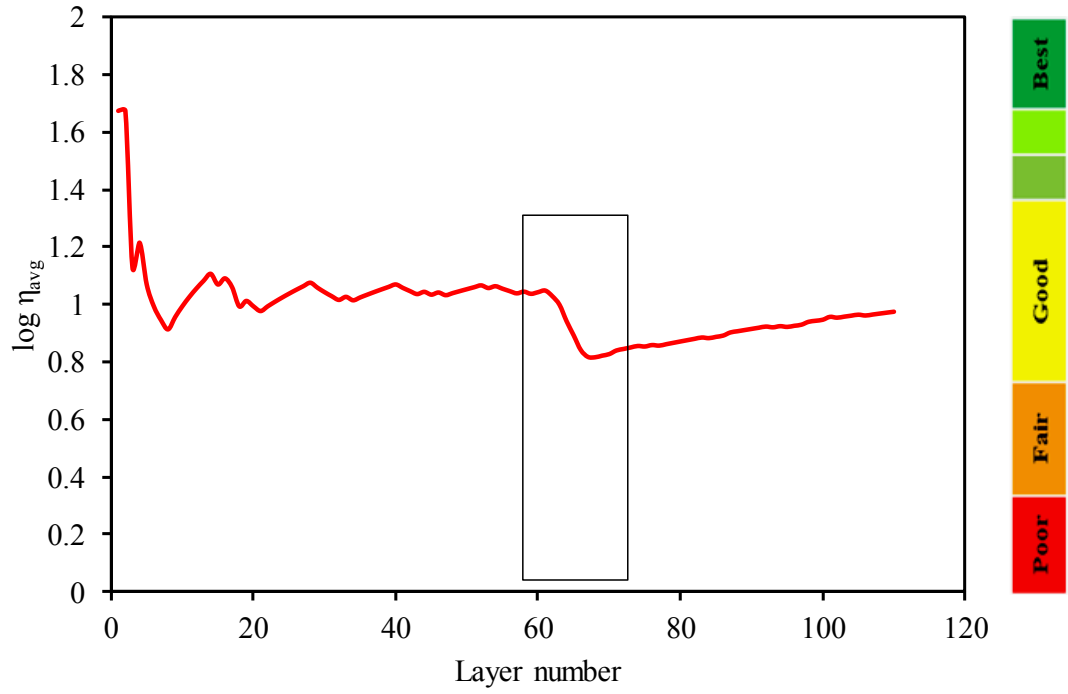


Figure 5.9 Change in average interfacial quality parameter ( $\eta_{avg}$ ) with layer build-up

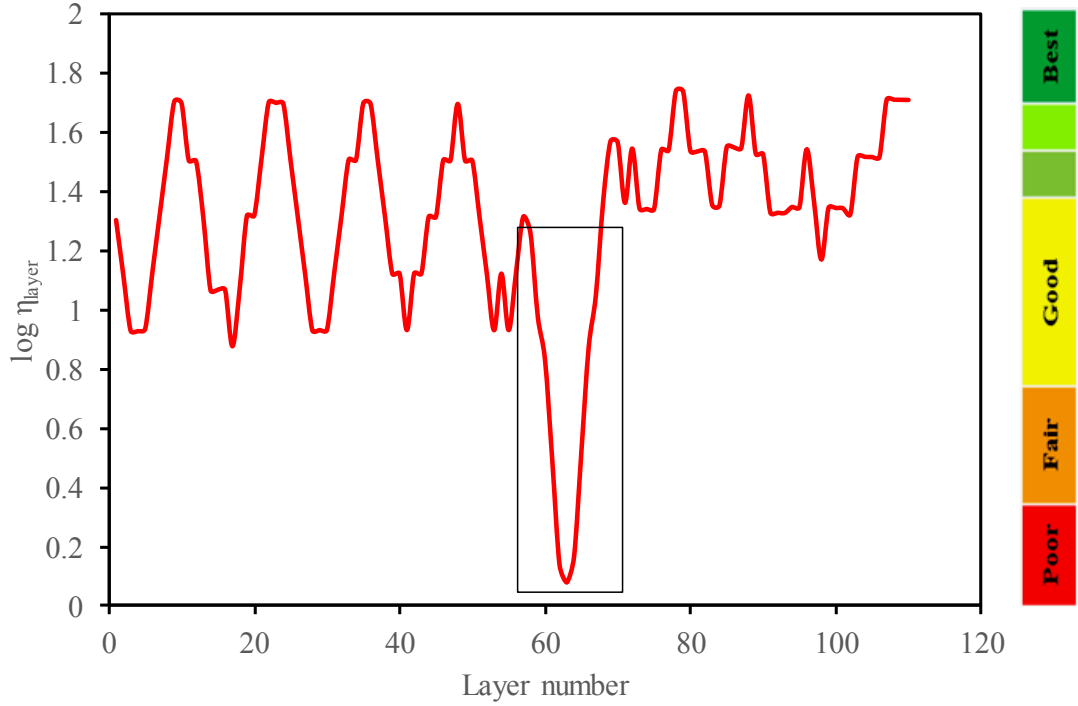


Figure 5.10 Change in layer-by-layer interfacial quality parameter with layer build-up

There is a reduction in the average quality in the first 20 layers and then between layer 60-70 after which there is a recovery. The reduction in the first 20 layers is due to interference at the base/build interface and the reduction between layer 60-70 is due to the interference of the echo from defective region with that from the top of the AM stack. If large enough number of layers are built on top, then the effect of the defective zone is eventually masked. But because of the availability of layer-by-layer information, we can estimate the location of the defective zone. Locating a defective zone is not tough using ultrasonic NDE, the challenge is to locate good quality bond hidden behind a defective zone. Fig. 5.10 shows a 5-layer moving average of the quality of each layer estimated according to Eq. (5.2). A cyclic pattern is observed due to the calculation of stiffness layer-by-layer. After each layer, any change in the ultrasonic velocity or attenuation is attributed to the newly bonded layer. The change in ultrasonic velocity could be due to wave interference and have nothing to do with the quality of the newly bonded layer. This effect is mitigated by considering the calculated stiffness of previous layers, but it cannot be fully avoided. Hence an average of several layers gives a much better representation of the quality of the component than characterizing each layer individually. The interference effect at the base/build interface is well accounted for. Similarly, a reduction in the quality between layers 60-70 accounts for the phase delay due to the defective region, thus the quality parameter that is calculated later can be measured. The average quality of the first 60 layers is lower than the average quality of the last 40 layers with the 10 layers in between having the lowest quality. These results indicate the potential of ultrasonic NDE for in-situ quality evaluation.

The results of this work allow us to propose a cost-effective methodology to develop and improve process parameters for new and existing materials. For example, in a single build with 1024 layers, considering 32 layers as one block (thickness is larger than wavelength of 5 MHz transducer), 8 different process parameters with 4 values each can be studied. Repeating a similar experiment by building coupons or tensile bars is very expensive. Ultrasonic NDE sensors are cheap and widely available. The data acquisition systems used in this study and Rieder *et al.* [90,91] are expensive and are meant for continuous monitoring with a high repetition rate. For layer-by-layer bond quality evaluation, data acquisition rate of 200 Hz along with a sampling frequency of 250 MHz is adequate. Typical oscilloscopes along with a pulser-receiver can be used to drive an ultrasonic transducer leading to a cost-effective in-situ NDE setup that saves machine time while developing process-structure-property correlations.

#### 5.4 Conclusion

Developing process parameters for new materials in L-PBF is an expensive and time-consuming process. Ultrasonic NDE is known to be sensitive to part quality, essentially measuring the change in elastic stiffness due to macro and microstructural changes. The advantages of utilizing in-situ NDE for process parameter development are obvious. However, there are several challenges to using in-situ ultrasonic NDE, the foremost being the interpretation of results due to interference effects. A model-based inversion routine coupled with a typical ultrasonic NDE system, leads to a cost-effective process parameter development setup. Developing process parameters for a cube or cylinder is not necessary if the material in question already has an optimal parameter range.

But, the optimal parameter set is not applicable to all kinds of geometries. These effects can be studied, and better process conditions can be developed for a wide range of geometries. Microstructural control can also be achieved through careful modification of build conditions. Process conditions that are difficult to study, like scan strategy and effect of chamber pressure can also be evaluated. In-situ ultrasonic NDE can benefit from and act as an add on to other in-situ NDE methods like laser profilometry, IR imaging, melt pool spectrometry, etc. Modeling ultrasonic wave propagation has helped understand the various features observed from in-situ NDE of L-PBF components, thus making it viable for in-situ monitoring. The results of this work make a strong case for the addition of an in-situ ultrasonic NDE tool to any materials R&D platform focused on developing process-structure-property correlations in L-PBF systems.

## CHAPTER 6

### CONCLUSIONS AND FUTURE WORK

#### 6.1 Conclusions

The research goal of this study was to establish process-structure-property correlations in metal additive manufacturing (AM) using ultrasonic nondestructive evaluation (NDE). Post-process or offline ultrasonic NDE was shown to be sensitive to changes in AM part quality. In-situ monitoring during part fabrication provides a unique opportunity to measure component quality as compared to traditional manufacturing processes. Due to small layer thickness and possibility of defect formation in each layer, interference effects contribute to the ultrasonic response. Hence it was important to model wave propagation behavior in AM components. A finite interfacial spring stiffness model was developed which accurately simulates experimentally observed phenomena. An in-situ monitoring ultrasonic NDE sensor setup was designed and installed on an Ultrasonic Additive Manufacturing (UAM) system. A model-based inversion of layer quality was proposed and demonstrated as an effective defect characterization and process optimization tool. A similar setup was installed on an open architecture Laser Powder Bed Fusion (LPBF) system. In-situ ultrasonic NDE is not suitable for real-time monitoring of complex-shaped AM components, but it provides valuable micro- and macro structural information during monitoring of regular geometries. The results achieved in this work make a strong case for the addition of in-situ ultrasonic NDE as an optimization and defect

characterization tool that can be used in conjunction with process models and destructive tests to improve existing metal AM processes. First, several NDE techniques were experimented with for their potential application to UAM components. linear ultrasonic testing, electromagnetic acoustic testing, phased array ultrasonic testing, nonlinear ultrasonic testing, and alternating current potential drop (ACPD) techniques were used on UAM components. Electromagnetic acoustic transducers (EMAT) and ACPD are an interesting alternative to measure UAM components from above, but that requires stopping of the manufacturing process and is not practical. Nonlinear ultrasonic testing alone is not sufficient and should be coupled with a linear ultrasonic system. Phased array ultrasonic imaging can be utilized to image UAM components but requires further modeling efforts to interpret the results due to interference effects. Hence, conventional linear ultrasonic NDE was chosen as a cost-effective in-situ monitoring method.

#### 6.1.1 Designing an in-situ nondestructive evaluation system for ultrasonic additive manufacturing

Two possible approaches of ultrasonic in-situ monitoring were proposed and tested, one from above the UAM stack and the other from below the base plate. Monitoring from above is not feasible since it involves stopping the manufacturing process. Monitoring from below, is a practical approach that can be used for continuous evaluation. The primary challenge lies in ensuring that the addition of the in-situ monitoring system does not alter the quality of UAM components. Supports are required to raise the base plate to accommodate the in-situ monitoring system. Supports along the bonding and vibration directions were tested and it was found that raising the base plate alters the quality of UAM

components as compared to the reference. Thus, a new set up was implemented wherein the ultrasonic NDE sensor is entirely embedded in a large solid block of aluminum. Through mechanical testing, it was shown that the quality of UAM components built on this set-up was comparable to that of base line components built with no transducer beneath them. The results from continuous monitoring indicated a stark contrast in TOF measurements during the moment of bonding. This phenomenon is due to the weld head passing over the top of the UAM stack with a large normal force. TOF change can thus be utilized as an indication of bonding and helps demarcate the interval between layers. The in-situ monitoring system can be used to capture the average ultrasonic response after each new UAM layer is bonded.

#### 6.1.2 In-situ interfacial quality assessment of ultrasonic additive manufacturing components using ultrasonic NDE

To understand the interaction of ultrasonic waves with UAM component and layer build up, a wave propagation model was developed with each UAM interface being modeled as a massless interfacial spring with finite stiffness. The model was validated using Finite Element simulations. It was found experimentally that one interfacial stiffness parameter was not sufficient to accurately model the observed phenomenon and hence two independent parameters ( $\eta_1$  and  $\eta$ ) were utilized. Switching to a two-parameter model, experimentally observed artifacts caused by interference between pulses could be accurately simulated. A two-parameter iterative inversion algorithm was developed which centers on calculating the base/build interfacial stiffness coefficient ( $\eta_1$ ) if the average stack interfacial stiffness coefficient ( $\eta$ ) is known. Sensitivity analysis on the inversion scheme



indicates that the proposed ultrasonic NDE technique is most sensitive between average and very good quality builds with the sensitivity parameter dropping off at both extremes which indicates that the technique is robust where necessary.

### 6.1.3 Monitoring and repair of defects in Ultrasonic Additive Manufacturing

Defects in UAM are classified into Type-1 (inter-layer) and Type-2 (inter-track). Type-1 defects are further divided into Type-1a and Type-1b defects. Type-1a defects occur at the base/build interface while Type-1b defects are inter-layer defects that occur at other locations within the UAM stack. Type-2 defects also occur within the stack but between two adjacent UAM tracks. An in-situ continuous online monitoring ultrasonic NDE setup was installed on a SoniClayer R7200 UAM system. A two-parameter wave propagation model previously developed was used to study the interaction of ultrasonic waves with UAM components. Post-process ultrasonic NDE was also used for physical visualization of delamination. The mechanism of formation and evolution of Type-1a and Type-1b defects was proposed based on NDE results. Type-1a defects are caused by cyclic loading of the base/build interface while Type-1b defects are caused by insufficient power transfer. The defects caused by lower power are a systemic problem in UAM components and can be remedied by amplitude compensation whereas Type-1a and Type-2 defects need to be addressed independently. Based on our understanding of the UAM defect evolution, Friction Stir Processing (FSP) was proposed as a novel in-situ repair and refinement tool for UAM components. While inter track defects are repaired from the top of UAM stack, base/build delamination is repaired from below the base. To illustrate the working of FSP, test components with defects were built. Friction Stir Processing repaired the defective

zones in both components. There are several advantages of using FSP as a complimentary repair mechanism specifically to heal existing inter-track defects. The results of this work pave the way for the development of a solid-state additive manufacturing process with UAM as the primary bonding mechanism integrated with FSP as a repair and refinement tool.

#### 6.1.4 Ultrasonic Nondestructive Evaluation as a Process Parameter Development Tool for Laser Powder Bed Fusion Additive Manufacturing

The L-PBF process involves a wide range of processing parameters and build conditions for making the AM component. Post-process annealing, heat treatment, HIPing and milling are often required to achieve necessary dimensional tolerance and structural performance. While the post-process treatments are a good way to deal with existing problems with L-PBF components, the best solution is to have a better-quality product coming out of the L-PBF system. There is scope for improving the build conditions to optimize the structural performance of AM components. Ultrasonic NDE provides macro- and microstructural information which is difficult to gather through other in-situ monitoring techniques. The advantages of utilizing in-situ NDE for process parameter development are obvious. A model-based inversion routine coupled with a typical ultrasonic NDE system, leads to a cost-effective process parameter development setup. Geometry dependent process parameters can be studied. Microstructural control can also be achieved through careful modification of build conditions. Process conditions that are difficult to study, like scan strategy and effect of chamber pressure can also be evaluated. Ultrasonic NDE is well suited to inform Finite Element simulation models. The results of

this work make a strong case for the addition of an in-situ ultrasonic NDE tool to any materials R&D platform focused on developing process-structure-property correlations in L-PBF systems.

## 6.2 Future Work

Several directions of future work were found while conducting the research presented in this thesis.

- 1) A Phased array ultrasonic transducer can be used to image metal AM components in-situ. Coupled with forward and inversion models, it is possible to extract 3D material quality information.
- 2) Comparing ultrasonic NDE data to other kinds of in-situ sensor data can provide valuable insights into the process-structure-property correlations for metal AM.
- 3) In this work, we investigated only longitudinal ultrasonic waves. Shear mode of ultrasonic NDE can be used to gain complimentary information.
- 4) While linear ultrasonic NDE is sensitive in the average to good quality range, nonlinear ultrasonic NDE methods such as wave-mixing and vibro-modulation are sensitive in the very good to best quality range that is practically undetectable through linear techniques.
- 5) Recent research has shown that combining wave-mixing nonlinear methods with phased array ultrasonic transducers (PAUT), it is possible to have both linear and nonlinear modes in a single PAUT [125-127].

- 6) By comparing in-situ sensor data with post-process NDE and destructive tests it is possible to design more efficient routines for process parameter development and metal AM component certification.

## REFERENCES

- [1] Janaki Ram, G. D., Robinson, C., Yang, Y., and Stucker, B. E. (2007). Use of ultrasonic consolidation for fabrication of multi-material structures. *Rapid Prototyping Journal* **13**, 226-235.
- [2] Friel, R. J., and Harris, R. A. (2013). Ultrasonic additive manufacturing—a hybrid production process for novel functional products. *Procedia CIRP* **6**, 35-40.
- [3] Kong, C. Y., and Soar, R. C. (2005). Fabrication of metal–matrix composites and adaptive composites using ultrasonic consolidation process. *Materials Science and Engineering: A* **412**, 12-18.
- [4] Yang, Y., Ram, G. J., and Stucker, B. E. (2009). Bond formation and fiber embedment during ultrasonic consolidation. *Journal of Materials Processing Technology* **209**, 4915-4924.
- [5] Obielodan, J. O., Ceylan, A., Murr, L. E., and Stucker, B. E. (2010). Multi-material bonding in ultrasonic consolidation. *Rapid Prototyping Journal* **16**, 180-188.
- [6] Sriraman, M. R., Babu, S. S., and Short, M. (2010). Bonding characteristics during very high power ultrasonic additive manufacturing of copper. *Scripta Materialia* **62**, 560-563.
- [7] Friel, R. J., Johnson, K. E., Dickens, P. M., and Harris, R. A. (2010). The effect of interface topography for Ultrasonic Consolidation of aluminium. *Materials Science and Engineering: A* **527**, 4474-4483.
- [8] Sriraman, M. R., Gonser, M., Fujii, H. T., Babu, S. S., and Bloss, M. (2011). Thermal transients during processing of materials by very high power ultrasonic additive manufacturing. *Journal of Materials Processing Technology* **211**, 1650-1657.
- [9] Schick, D., Suresh Babu, S., Foster, D. R., Dapino, M., Short, M., and Lippold, J. C. (2011). Transient thermal response in ultrasonic additive manufacturing of aluminum 3003. *Rapid Prototyping Journal* **17**, 369-379.
- [10] Zhang, C. S., and Li, L. (2009). A coupled thermal-mechanical analysis of ultrasonic bonding mechanism. *Metallurgical and Materials Transactions B* **40**, 196-207.

- [11] Robinson, C. J., Janaki Ram G. D., and Stucker, B. E. (2011) Role of substrate stiffness in ultrasonic consolidation, *International Journal of Rapid Manufacturing* **2**, 162-177.
- [12] Kong, C. Y., Soar, R. C., and Dickens, P. M. (2003). Characterization of aluminum alloy 6061 for the ultrasonic consolidation process. *Materials Science and Engineering: A* **363**, 99-106.
- [13] Kelly, G. S., Advani, S. G., Gillespie Jr, J. W., and Bogetti, T. A. (2013). A model to characterize acoustic softening during ultrasonic consolidation. *Journal of Materials Processing Technology* **213**, 1835-1845.
- [14] Fujii, H. T., Sriraman, M. R., and Babu, S. S. (2011). Quantitative evaluation of bulk and interface microstructures in Al-3003 alloy builds made by very high power ultrasonic additive manufacturing. *Metallurgical and Materials Transactions A* **42**, 4045-4055.
- [15] Ram, G., Yang, Y., George, J., Robinson, C., and Stucker, B. (2006). Improving linear weld density in ultrasonically consolidated parts. In *Proceedings of the 17th Solid Freeform Fabrication Symposium*, 692-708.
- [16] Dehoff, R. R., and Babu, S. S. (2010). Characterization of interfacial microstructures in 3003 aluminum alloy blocks fabricated by ultrasonic additive manufacturing. *Acta Materialia* **58**, 4305-4315.
- [17] Shimizu, S., Fujii, H. T., Sato, Y. S., Kokawa, H., Sriraman, M. R., and Babu, S. S. (2014). Mechanism of weld formation during very-high-power ultrasonic additive manufacturing of Al alloy 6061. *Acta Materialia* **74**, 234-243.
- [18] Kong, C. Y., Soar, R. C., and Dickens, P. M. (2004). Optimum process parameters for ultrasonic consolidation of 3003 aluminium. *Journal of Materials Processing Technology* **146**, 181-187.
- [19] Obielodan, J. O., and Stucker, B. E. (2009). Effects of post processing heat treatments on the bond quality and mechanical strength of Ti/Al3003 dual materials fabricated using ultrasonic consolidation. In *Proceedings of the 20th Solid Freeform Fabrication Symposium*, 406-427.
- [20] Zhang, C. S., Deceuster, A., and Li, L. (2009). A method for bond strength evaluation for laminated structures with application to ultrasonic consolidation. *Journal of Materials Engineering and Performance* **18**, 1124-1132.
- [21] Koellhoffer, S., Gillespie Jr, J. W., Advani, S. G., and Bogetti, T. A. (2011). Role of friction on the thermal development in ultrasonically consolidated aluminum foils and composites. *Journal of Materials Processing Technology* **211**, 1864-1877.

- [22] Sriraman, M. R., Gonser, M., Fujii, H. T., Babu, S. S., and Bloss, M. (2011). Thermal transients during processing of materials by very high power ultrasonic additive manufacturing. *Journal of Materials Processing Technology* **211**, 1650-1657.
- [23] Mariani, E., and Ghassemieh, E. (2010). Microstructure evolution of 6061 O Al alloy during ultrasonic consolidation: an insight from electron backscatter diffraction. *Acta Materialia* **58**, 2492-2503.
- [24] Kong, C. Y., Soar, R. C., and Dickens, P. M. (2005). A model for weld strength in ultrasonically consolidated components. *Proceedings of the Institution of Mechanical Engineers, Part C: Journal of Mechanical Engineering Science* **219**, 83-91.
- [25] Zhang, C., Zhu, X., and Li, L. (2006). A study of friction behavior in ultrasonic welding (consolidation) of aluminum. In *Proceedings of the AWS Conference*, 151-156.
- [26] Foster, D. R., Dapino, M. J., and Babu, S. S. (2013). Elastic constants of ultrasonic additive manufactured Al 3003-H18. *Ultrasonics* **53**, 211-218.
- [27] Hopkins, C. D., Wolcott, P. J., Dapino, M. J., Truog, A. G., Babu, S. S., and Fernandez, S. A. (2012). Optimizing ultrasonic additive manufactured Al 3003 properties with statistical modeling. *Journal of Engineering Materials and Technology* **134**, 011004.
- [28] Foster, D. R., Taber, G. A., Babu, S. S., and Daehn, G. S. (2014). In situ velocity measurements of very high power ultrasonic additive manufacturing using a photonic Doppler velocimeter. *Science and Technology of Welding and Joining* **19**, 157-163.
- [29] White, D. (2003). *U.S. Patent No. 6,519,500*. Washington, DC: U.S. Patent and Trademark Office.
- [30] Kong, C. Y., and Soar, R. (2005). Method for embedding optical fibers in an aluminum matrix by ultrasonic consolidation. *Applied Optics* **44**, 6325-6333.
- [31] Kulakov, M., and Rack, H. J. (2009). Control of 3003-H18 aluminum ultrasonic consolidation. *Journal of Engineering Materials and Technology* **131**, 021006.
- [32] Kong, C. Y., Soar, R. C., and Dickens, P. M. (2004). Ultrasonic consolidation for embedding SMA fibres within aluminium matrices. *Composite Structures* **66**, 421-427.
- [33] Siddiq, A., and Ghassemieh, E. (2009). Theoretical and FE analysis of ultrasonic welding of aluminum alloy 3003. *Journal of Manufacturing Science and Engineering* **131**, 041007.
- [34] Li, D., and Soar, R. C. (2009). Characterization of process for embedding SiC fibers in Al 6061 O matrix through ultrasonic consolidation. *Journal of Engineering Materials and Technology* **131**, 021016.

- [35] Li, D., and Soar, R. (2007). Optimum process parameters and influencing factors for embedding SiC fibres in Al 6061 O matrix through ultrasonic consolidation. *Materials Science and Technology-Association for Iron and Steel Technology* **5**, 3048- 3064.
- [36] Kendall, K. (1971). An ultrasonic study of the area of contact between stationary and sliding surfaces. *Proc. R. Soc. Lond. A* **323**, 321-340.
- [37] Haines, N. F., and Langston, D. B. (1980). The reflection of ultrasonic pulses from surfaces. *Journal of the Acoustical Society of America* **67**, 1443-1454.
- [38] Baik, J. M., and Thompson, R. B. (1984). Ultrasonic scattering from imperfect interfaces: a quasi-static model. *Journal of Nondestructive Evaluation* **4**, 177-196.
- [39] Nagy, P. B., and Adler, L. (1988). Ultrasonic NDE of solid-state bonds: inertia and friction welds. *Journal of Nondestructive Evaluation* **7**, 199-215.
- [40] Nagy, P. B. (1992). Ultrasonic classification of imperfect interfaces. *Journal of Nondestructive Evaluation* **11**, 127-139.
- [41] Pilarski, A., and Rose, J. L. (1988). A transverse-wave ultrasonic oblique-incidence technique for interfacial weakness detection in adhesive bonds. *Journal of Applied Physics* **63**, 300-307.
- [42] Adams, R. D., and Drinkwater, B. W. (1997). Nondestructive testing of adhesively-bonded joints. *NDT & E International* **30**, 93-98.
- [43] Brotherhood, C. J., Drinkwater, B. W., and Dixon, S. (2003). The detectability of kissing bonds in adhesive joints using ultrasonic techniques. *Ultrasonics* **41**, 521-529.
- [44] Lavrentyev, A. I., and Beals, J. T. (2000). Ultrasonic measurement of the diffusion bond strength. *Ultrasonics* **38**, 513-516.
- [45] Cheng, A., and Deutsch, W. (1998). Characterization of diffusion bonds of titanium plates using transmitted ultrasonic signals. *NDT & E International* **31**, 175-182.
- [46] Escobar-Ruiz, E., Ruiz, A., Hassan, W., Wright, D. C., Collison, I. J., Cawley, P., and Nagy, P. B. (2014). Non-linear ultrasonic NDE of titanium diffusion bonds. *Journal of Nondestructive Evaluation* **33**, 187-195.
- [47] Milne, K., Cawley, P., Nagy, P. B., Wright, D. C., and Dunhill, A. (2011). Ultrasonic non-destructive evaluation of titanium diffusion bonds. *Journal of Nondestructive Evaluation* **30**, 225-236.
- [48] Hirao, M., and Ogi, H. (2013). *EMATs for science and industry: non-contacting ultrasonic measurements*. Springer Science & Business Media.



- [49] Hirao, M., and Ogi, H. (1999). An SH-wave EMAT technique for gas pipeline inspection. *NDT & E International* **32**, 127-132.
- [50] Hirao, M., Ogi, H., and Yasui, H. (2001). Contactless measurement of bolt axial stress using a shear-wave electromagnetic acoustic transducer. *NDT & E International* **34**, 179-183.
- [51] Gao, H., and Lopez, B. (2010). Development of single-channel and phased array electromagnetic acoustic transducers for austenitic weld testing. *Materials Evaluation* **68**, 821-827.
- [52] Ribichini, R. (2011). Modelling of electromagnetic acoustic transducers. PhD dissertation, Imperial College London.
- [53] Drinkwater, B. W., and Wilcox, P. D. (2006). Ultrasonic arrays for non-destructive evaluation: A review. *NDT & E International* **39**, 525-541.
- [54] Schimmer Jr, L. W. (2008). Fundamentals of ultrasonic phased arrays. *Modern Physics Letters B* **22**, 917-921.
- [55] Lane, C. (2013). The development of a 2D ultrasonic array inspection for single crystal turbine blades. *Springer Science & Business Media*.
- [56] Donskoy, D. M., and Sutin, A. M. (1998). Vibro-acoustic modulation nondestructive evaluation technique. *Journal of Intelligent Material Systems and Structures* **9**, 765-771.
- [57] Zagrai, A., Donskoy, D., and Lottiaux, J. L. (2004). N-Scan®: New Vibro-Modulation System for Crack Detection, Monitoring and Characterization. In *AIP Conference Proceedings* **700**, 1414-1421.
- [58] Zagrai, A., Donskoy, D., Chudnovsky, A., and Golovin, E. (2008). Micro-and macroscale damage detection using the nonlinear acoustic vibro-modulation technique. *Research in Nondestructive Evaluation* **19**, 104-128.
- [59] Duffour, P., Morbidini, M., and Cawley, P. (2006). A study of the vibro-acoustic modulation technique for the detection of cracks in metals. *Journal of the Acoustical Society of America* **119**, 1463-1475.
- [60] Nagy, P. B. (1998). Fatigue damage assessment by nonlinear ultrasonic materials characterization. *Ultrasonics* **36**, 375-381.
- [61] Zhang, Z., Nagy, P. B., & Hassan, W., Analytical and numerical modeling of non-collinear shear wave mixing at an imperfect interface. *Ultrasonics*, **65**, 165-176 (2016).

- [62] Croxford, A. J., Wilcox, P. D., Drinkwater, B. W., and Nagy, P. B. (2009). The use of non-collinear mixing for nonlinear ultrasonic detection of plasticity and fatigue. *Journal of the Acoustical Society of America* **126**, 117-122.
- [63] Demčenko, A., Akkerman, R., Nagy, P. B., and Loendersloot, R. (2012). Non-collinear wave mixing for non-linear ultrasonic detection of physical ageing in PVC. *NDT & E International* **49**, 34-39.
- [64] Liu, M., Tang, G., Jacobs, L. J., and Qu, J. (2012). Measuring acoustic nonlinearity parameter using collinear wave mixing. *Journal of Applied Physics* **112**, 024908.
- [65] Sposito, G., Cawley, P., and Nagy, P. B. (2010). An approximate model for three-dimensional alternating current potential drop analyses using a commercial finite element code. *NDT & E International* **43**, 134-140.
- [66] Sposito, G. (2009). Advances in potential drop techniques for non-destructive testing. PhD dissertation, Imperial College London.
- [67] Prajapati, S., Nagy, P. B., and Cawley, P. (2012). Potential drop detection of creep damage in the vicinity of welds. *NDT & E International* **47**, 56-65.
- [68] ASTM Standard terminology for additive manufacturing technologies, (2012). *ASTM Standard F2792-12a*, ASTM International, West Conshohocken, PA.
- [69] Thijs, L., Verhaeghe, F., Craeghs, T., Van Humbeeck, J., and Kruth, J. P. (2010). A study of the microstructural evolution during selective laser melting of Ti-6Al-4V. *Acta Materialia* **58**, 3303-3312.
- [70] Gong, H., Rafi, K., Gu, H., Starr, T., and Stucker, B. (2014). Analysis of defect generation in Ti-6Al-4V parts made using powder bed fusion additive manufacturing processes. *Additive Manufacturing* **1**, 87-98.
- [71] Gong, H., Rafi, K., Gu, H., Ram, G. J., Starr, T., and Stucker, B. (2015). Influence of defects on mechanical properties of Ti-6Al-4 V components produced by selective laser melting and electron beam melting. *Materials & Design* **86**, 545-554.
- [72] Dilip, J. J. S., Anam, M. A., Pal, D., and Stucker, B. (2016). A short study on the fabrication of single track deposits in SLM and characterization. In *Proceedings of 27<sup>th</sup> Solid Freeform Fabrication Symposium*, 1644-1659.
- [73]. Arısoy, Y. ., Criales, . E., Ö el, T., ane, B., o ylan, S., and Donmez, A. (2017). Influence of scan strategy and process parameters on microstructure and its optimization in additively manufactured nickel alloy 625 via laser powder bed fusion. *International Journal of Advanced Manufacturing Technology* **90**, 1393-1417.

- [74] Gu, D. D., Meiners, W., Wissenbach, K., and Poprawe, R. (2012). Laser additive manufacturing of metallic components: materials, processes, and mechanisms. *International Materials Reviews* **57**, 133-164.
- [75] Kamath, C., El-dasher, B., Gallegos, G. F., King, W. E., and Sisto, A. (2014). Density of additively-manufactured, 316L SS parts using laser powder-bed fusion at powers up to 400 W. *The International Journal of Advanced Manufacturing Technology* **74**, 65-78.
- [76] Xu, W., Brandt, M., Sun, S., Elambasseril, J., Liu, Q., Latham, K., and Qian, M. (2015). Additive manufacturing of strong and ductile Ti–6Al–4V by selective laser melting via in situ martensite decomposition. *Acta Materialia* **85**, 74-84.
- [77] Fox, J. C., Moylan, S. P., and Lane, B. M. (2016). Effect of process parameters on the surface roughness of overhanging structures in laser powder bed fusion additive manufacturing. *Procedia CIRP* **45**, 131-134.
- [78] Mercelis, P., and Kruth, J. P. (2006). Residual stresses in selective laser sintering and selective laser melting. *Rapid Prototyping Journal* **12**, 254-265.
- [79]. Khairallah, S. A., Anderson, A. T., Rubenchik, A., and King, W. E. (2016). Laser powder-bed fusion additive manufacturing: Physics of complex melt flow and formation mechanisms of pores, spatter, and denudation zones. *Acta Materialia* **108**, 36-45.
- [80] Matthews, M. J., Guss, G., Khairallah, S. A., Rubenchik, A. M., Depond, P. J., and King, W. E. (2016). Denudation of metal powder layers in laser powder bed fusion processes. *Acta Materialia* **114**, 33-42.
- [81] Criales, E., Arisoy, Y., and Özel, T. (2016). Sensitivity analysis of material and process parameters in finite element modeling of selective laser melting of Inconel 625. *International Journal of Advanced Manufacturing Technology* **86**, 2653-2666.
- [82] Lopez, F., Witherell, P., and Lane, B. (2016). Identifying uncertainty in laser powder bed fusion additive manufacturing models. *Journal of Mechanical Design* **138**, 114502.
- [83] Acharya, R., Sharon, J. A., and Staroselsky, A. (2017). Prediction of microstructure in laser powder bed fusion process. *Acta Materialia* **124**, 360-371.
- [84] Everton, S. K., Hirsch, M., Stravroulakis, P., Leach, R. K., and Clare, A. T. (2016). Review of in-situ process monitoring and in-situ metrology for metal additive manufacturing. *Materials & Design* **95**, 431-445.
- [85] Repossini, G., Laguzza, V., Grasso, M., and Colosimo, B. M. (2017). On the use of spatter signature for in-situ monitoring of Laser Powder Bed Fusion. *Additive Manufacturing* **16**, 35-48.

- [86] Zhao, C., Fezzaa, K., Cunningham, R. W., Wen, H., Carlo, F., Chen, L., and Sun, T. (2017). Real-time monitoring of laser powder bed fusion process using high-speed X-ray imaging and diffraction. *Scientific Reports* **7-3602**, 1-9.
- [87] Land II, W. S., Zhang, B., Ziegert, J., and Davies, A. (2015). In-situ metrology system for laser powder bed fusion additive process. *Procedia Manufacturing* **1**, 393-403.
- [88] Dunbar, A. J., Denlinger, E. R., Heigel, J., Michaleris, P., Guerrier, P., Martukanitz, R., and Simpson, T. W. (2016). Development of experimental method for in situ distortion and temperature measurements during the laser powder bed fusion additive manufacturing process. *Additive Manufacturing* **12**, 25-30.
- [89] Todorov, E., Boulware, P., and Gaah, K. (2018). Demonstration of array eddy current technology for real-time monitoring of laser powder bed fusion additive manufacturing process. In *Proceedings of Nondestructive Characterization and Monitoring of Advanced Materials, Aerospace, Civil Infrastructure, and Transportation XII* **1059913**, 1-9.
- [90] Rieder, H., Spies, M., Bamberg, J., and Henkel, B. (2016). On-and Offline Ultrasonic Inspection of Additively Manufactured Components. In *Proceedings of 19th World Conference on Non-Destructive Testing (WCNDT), Munich, Germany*, 13-17.
- [91] Rieder, H., Dillhöfer, A., Spies, M., Bamberg, J., and Hess, T. (2015). Ultrasonic online monitoring of additive manufacturing processes based on selective laser melting. In *AIP Conference Proceedings* **1650**, 184-191.
- [92] Everton, S., Dickens, P., Tuck, C., and Dutton, B. (2018). Using Laser Ultrasound to Detect Subsurface Defects in Metal Laser Powder Bed Fusion Components. *JOM* **70**, 378-383.
- [93] Sridharan, N., Wolcott, P., Dapino, M., and Babu, S. S. (2016). Microstructure and texture evolution in aluminum and commercially pure titanium dissimilar welds fabricated using ultrasonic additive manufacturing. *Scripta Materialia* **117**, 1-5.
- [94] Gussev, M. N., Sridharan, N., Thompson, Z., Terrani, K. A., and Babu, S. S. (2018). Influence of hot isostatic pressing on the performance of aluminum alloy fabricated by ultrasonic additive manufacturing. *Scripta Materialia* **145**, 33-36.
- [95] Gussev, M. N., Sridharan, N., Norfolk, M., Terrani, K. A., and Babu, S. S. (2017). Effect of post weld heat treatment on the 6061 aluminum alloy produced by ultrasonic additive manufacturing. *Materials Science and Engineering: A* **684**, 606-616.
- [96] Nadimpalli, V. K., Na, J. K., Bruner, D. T., King, B. A., Yang, L., and Stucker, B. E. (2016). In-Situ Non-Destructive Evaluation of Ultrasonic Additive Manufactured Components. In *Proceedings of 27<sup>th</sup> Solid Freeform Fabrication Symposium*, 1557-1567.

- [97] Nagy, P. B., and Adler, L. (1987). Surface roughness induced attenuation of reflected and transmitted ultrasonic waves. *Journal of the Acoustical Society of America* **82**, 193-197.
- [98] Wolcott, P. J., Hehr, A., and Dapino, M. J. (2014). Optimized welding parameters for Al 6061 ultrasonic additive manufactured structures. *Journal of Materials Research* **29**, 2055-2065.
- [99] Purtonen, T., Kalliosaari, A., and Salminen, A. (2014). Monitoring and adaptive control of laser processes. *Physics Procedia* **56**, 1218-1231.
- [100] Seifi, M., Salem, A., Beuth, J., Harrysson, O., and Lewandowski, J. J. (2016). Overview of materials qualification needs for metal additive manufacturing. *JOM* **68**, 747-764.
- [101] Slotwinski, J. A., Garboczi, E. J., and Hebenstreit, K. M. (2014). Porosity measurements and analysis for metal additive manufacturing process control. *Journal of Research of the National Institute of Standards and Technology* **119**, 494-528.
- [102]. Rieder, H., Spies, M., Bamberg, J., Henkel, B., and Müller, S. (2016). On and offline ultrasonic characterization of components built by SLM additive manufacturing. *42<sup>nd</sup> Annual Review of Progress in Quantitative Nondestructive Evaluation* **1706**, 130002.
- [103] Hehr, A., Wolcott, P. J., Wolcott, P. J., Dapino, M. J., and Dapino, M. J. (2016). Effect of weld power and build compliance on ultrasonic consolidation. *Rapid Prototyping Journal* **22**, 377-386.
- [104] Kino, G. S. (1988). *Acoustic Waves: Devices, Imaging, and Analog Signal Processing*. New Jersey: Prentice Hall.
- [105] Pierce, A. D. (1981). *Acoustics: an introduction to its physical principles and applications*. New York: McGraw-Hill.
- [106] Allard, J., and Atalla, N. (2009). *Propagation of sound in porous media: modelling sound absorbing materials*. John Wiley & Sons.
- [107] Rokhlin, S. I., Chimenti, D. E., and Nagy, P. B. (2011). *Physical Ultrasonics of Composites*. Oxford: Oxford University Press.
- [108] Ishii, Y., and Biwa, S. (2012). Ultrasonic evaluation of interlayer interfacial stiffness of multilayered structures. *Journal of Applied Physics* **111**, 084907.
- [109] Li, J., Monaghan, T., Nguyen, T. T., Kay, R. W., Friel, R. J., and Harris, R. A. (2017). Multifunctional metal matrix composites with embedded printed electrical materials

fabricated by ultrasonic additive manufacturing. *Composites Part B: Engineering* **113**, 342-354.

[110] Bournias-Varotsis, A., Wang, S., Hutt, D., and Engstrøm, D. S. (2018). The effect of ultrasonic additive manufacturing on integrated printed electronic conductors. *Electronic Materials Letters* **14**, 1-13.

[111] Hehr, A., Norfolk, M., Wenning, J., Sheridan, J., Leser, P., and Newman, J. A. (2018). Integrating fiber optic strain sensors into metal using ultrasonic additive manufacturing. *JOM* **70**, 315-320.

[112] Burns, J. R., Petrovic, B., Chandler, D., and Terrani, K. A. (2018). Reactor physics phenomena in additively manufactured control elements for the high flux isotope reactor. *Annals of Nuclear Energy* **115**, 403-414.

[113] Sridharan, N., Gussev, M. N., Parish, C. M., Isheim, D., Seidman, D. N., Terrani, K. A., and Babu, S. S. (2018). Evaluation of microstructure stability at the interfaces of Al-6061 welds fabricated using ultrasonic additive manufacturing. *Materials Characterization* **139**, 249-258.

[114] Levy, A., Miriyev, A., Sridharan, N., Han, T., Tuval, E., Babu, S. S., and Frage, N. (2018). Ultrasonic additive manufacturing of steel: Method, post-processing treatments and properties. *Journal of Materials Processing Technology* **256**, 183-189.

[115] Obielodan, J., Janaki Ram, G. D., Stucker, B. E., and Taggart, D. (2010) Minimizing defects between adjacent foils in ultrasonically consolidated parts, *Journal of Engineering Materials and Technology* **132**, 1-8.

[116] Gibert, J. M., Fadel, G., and Daqaq, M. F. (2013). On the stick-slip dynamics in ultrasonic additive manufacturing. *Journal of Sound and Vibration* **332**, 4680-4695.

[117] Nadimpalli, V. K., Yang, L., and Nagy, P. B. (2018). In-situ interfacial quality assessment of Ultrasonic Additive Manufacturing components using ultrasonic NDE. *NDT & E International* **93**, 117-130.

[118] Nadimpalli, V. K., and Nagy, P. B., (2018). Designing an in-situ ultrasonic nondestructive evaluation system for ultrasonic additive manufacturing. In *Proceedings of Annual Review of Progress in Qualitative Nondestructive Evaluation* **1949**, 020005, 1-10.

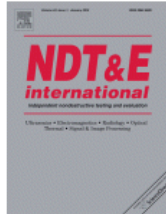
[119] Dilip, J. J. S., Janaki Ram, G. D., and Stucker, B. E. (2012). Additive manufacturing with friction welding and friction deposition processes. *International Journal of Rapid Manufacturing* **3**, 56-69.

- [120] Kalvala, P. R., Akram, J., and Misra, M. (2016). Friction assisted solid state lap seam welding and additive manufacturing method. *Defence Technology* **12**, 16-24.
- [121] Sharma, A., Bandari, V., Ito, K., Kohama, K., Ramji, M., and BV, H. S. (2017). A new process for design and manufacture of tailor-made functionally graded composites through friction stir additive manufacturing. *Journal of Manufacturing Processes* **26**, 122-130.
- [122] Palanivel, S., Nelaturu, P., Glass, B., and Mishra, R. S. (2015). Friction stir additive manufacturing for high structural performance through microstructural control in an Mg based WE43 alloy. *Materials & Design* **65**, 934-952.
- [123] Mishra, R. S., and Ma, Z. Y. (2005). Friction stir welding and processing. *Materials Science and Engineering: R: Reports* **50**, 1-78.
- [124] King, W. E., Barth, H. D., Castillo, V. M., Gallegos, G. F., Gibbs, J. W., Hahn, D. E., and Rubenchik, A. M. (2014). Observation of keyhole-mode laser melting in laser powder-bed fusion additive manufacturing. *Journal of Materials Processing Technology* **214**, 2915-2925.
- [125] Potter, J. N., Croxford, A. J., and Wilcox, P. D. (2014). Nonlinear ultrasonic phased array imaging. *Physical Review Letters* **113**, 144301.
- [126] Cheng, J., Potter, J. N., Croxford, A. J., and Drinkwater, B. W. (2017). Monitoring fatigue crack growth using nonlinear ultrasonic phased array imaging. *Smart Materials and Structures* **26**, 055006.
- [127] Hauptert, S., Renaud, G., and Schumm, A. (2017). Ultrasonic imaging of nonlinear scatterers buried in a medium. *NDT & E International* **87**, 1-6.

APPENDIX  
PERMISSIONS

This appendix includes all required permissions for publication of the papers presented as chapters in this dissertation.





**Title:** In-situ interfacial quality assessment of Ultrasonic Additive Manufacturing components using ultrasonic NDE  
**Author:** Venkata Karthik Nadimpalli, Li Yang, Peter B. Nagy  
**Publication:** NDT & E International  
**Publisher:** Elsevier  
**Date:** January 2018  
© 2017 Elsevier Ltd. All rights reserved.

**LOGIN**  
If you're a [copyright.com](#) user, you can login to RightsLink using your [copyright.com](#) credentials.  
Already a [RightsLink](#) user or want to [learn more?](#)

### Quick Price Estimate

I would like to... ?

reuse in a thesis/dissertation

I would like to use... ?

full article

My format is... ?

both print and electronic

I am the author of this Elsevier article... ?

Yes

I will be translating... ?

No

My currency is...

USD - \$

Quick Price

Click Quick Price

QUICK PRICE

CONTINUE

**This service provides permission for reuse only.** If you do not have a copy of the content, you may be able to purchase a copy using RightsLink as an additional transaction. Simply select 'I would like to....' 'Purchase this content'.

Unclear about [who you are?](#)



**Title:** In-situ interfacial quality assessment of Ultrasonic Additive Manufacturing components using ultrasonic NDE  
**Author:** Venkata Karthik Nadimpalli, Li Yang, Peter B. Nagy  
**Publication:** NDT & E International  
**Publisher:** Elsevier  
**Date:** January 2018  
© 2017 Elsevier Ltd. All rights reserved.

**LOGIN**  
If you're a [copyright.com](#) user, you can login to RightsLink using your [copyright.com](#) credentials.  
Already a [RightsLink](#) user or want to [learn more?](#)

Please note that, as the author of this Elsevier article, you retain the right to include it in a thesis or dissertation, provided it is not published commercially. Permission is not required, but please ensure that you reference the journal as the original source. For more information on this and on your other retained rights, please visit: <https://www.elsevier.com/about/our-business/policies/copyright#Author-rights>

BACK

CLOSE WINDOW

Reference has been cited in the dissertation [117]



**MONOGRAPHIC SERIES**

**ISSN:** 0094-243X  
**Publication year(s):** 1970 - present  
**Author/Editor:** AMERICAN INSTITUTE OF PHYSICS  
**Publisher:** SPRINGER-VERLAG  
**Rightsholder:** AMERICAN INSTITUTE OF PHYSICS

**Language:** English  
**Country of publication:** United States of America

**Academic**

Photocopy or share content electronically

**LICENSE COVERAGE**

**Annual Copyright License for Academic Institutions**

This permission type is covered. The Annual Copyright License authorizes the licensee's faculty, staff, students, and other authorized users to distribute print and electronic copies of copyrighted content within your institution through:

- Print or electronic coursepacks
- Classroom handouts
- Electronic reserves
- Institution Intranets
- Course/Learning Management systems (CMS/LMS)
- CD-ROM/DVD
- Other internal academic uses

The description above is provided for summary purposes only. Please refer to your institution's Annual Copyright License for the complete terms and conditions and scope of coverage of the license.

Covered by CCC Annual License - Academic

Reference has been cited in the dissertation [118]

## Re: Permission to include papers in dissertation

Peter B. Nagy

Thu 5/3/2018 8:58 AM

To: Nadimpalli, Venkata Karthik <karthik.nadimpalli@louisville.edu>;

Hi Karthik,

I grant permission for you to include the papers listed below in your dissertation.

Regards,

Peter B. Nagy  
Professor, Dept. of Aerospace Engineering  
University of Cincinnati  
731 Rhodes Hall, ML0070  
Cincinnati, Ohio 45221-0070  
t.: (513) 556-3353  
e-mail: [peter.nagy@uc.edu](mailto:peter.nagy@uc.edu)

On 5/1/2018 4:00 PM, Nadimpalli, Venkata Karthik wrote:

Dear Dr. Nagy,

I am preparing a multi-paper dissertation which will include the papers listed below. I am requesting your permission to include the material just as it appears in the papers.

1. Nadimpalli, V. K., and Nagy, P. B., (2018). Designing an in-situ ultrasonic nondestructive evaluation system for ultrasonic additive manufacturing. In *Proceedings of Annual Review of Progress in Qualitative Nondestructive Evaluation* **1949**, 020005, 1-10.
2. Nadimpalli, V. K., Yang, L., & Nagy, P. B. (2018). In-situ interfacial quality assessment of Ultrasonic Additive Manufacturing components using ultrasonic NDE. *NDT & E International* **93**, 117-130.
3. Nadimpalli, V. K., Karthik, G. M., Ram, G. J., and Nagy, P. B. (2018). Monitoring and repair of defects in ultrasonic additive manufacturing. To be submitted to *Journal of Materials Processing Technology*.
4. Nadimpalli, V. K., Middendorf, J., Gong, H., Yang, L., and Nagy, P. B. (2018). Ultrasonic nondestructive evaluation as a process parameter development tool for laser powder bed fusion additive manufacturing. To be submitted to *Additive Manufacturing*.

Please indicate your approval by replying to this mail, Thank you!

Best Regards,

Venkata Karthik Nadimpalli

## RE: Permission to include papers in dissertation

Yang,Li

Tue 5/1/2018 7:43 PM

To: Nadimpalli,Venkata Karthik <karthik.nadimpalli@louisville.edu>;

Hi Karthik,

I approve that that these materials can be included in your dissertation as they appear in the papers since your dissertation is structured in such way.

Thanks,  
Li

Li Yang  
University of Louisville  
502-852-2197

---

**From:** Nadimpalli,Venkata Karthik  
**Sent:** Tuesday, May 1, 2018 4:06:25 PM  
**To:** Yang,Li  
**Subject:** Permission to include papers in dissertation

Dear Dr. Yang,

I am preparing a multi-paper dissertation which will include the papers listed below. I am requesting your permission to include the material just as it appears in the papers.

1. Nadimpalli, V. K., Yang, L., & Nagy, P. B. (2018). In-situ interfacial quality assessment of Ultrasonic Additive Manufacturing components using ultrasonic NDE. *NDT & E International* **93**, 117-130.
2. Nadimpalli, V. K., Middendorf, J., Gong, H., Yang, L., and Nagy, P. B. (2018). Ultrasonic nondestructive evaluation as a process parameter development tool for laser powder bed fusion additive manufacturing. To be submitted to *Additive Manufacturing*.

Please indicate your approval by replying to this mail, Thank you!

Best Regards,

Venkata Karthik Nadimpalli

---

## Permission to include paper in dissertation

---

**Durga Janaki Ram Gabbita** <jram@iitm.ac.in>  
To: Karthik Nadimpalli <knadimpalli18@gmail.com>

Wed, May 2, 2018 at 12:02 AM

Dear Karthik,

Please feel free to include the paper in your dissertation.

With kind regards,

Janaki Ram

Dr. G.D. Janaki Ram  
Associate Professor  
Metallurgical and Materials Engineering  
IIT Madras, Chennai - 600 036, India  
Phone: +91-44-22574780  
Email: [jram@iitm.ac.in](mailto:jram@iitm.ac.in)

---

**From:** Karthik Nadimpalli <knadimpalli18@gmail.com>  
**Sent:** Wednesday, May 2, 2018 1:38  
**To:** Durga Janaki Ram Gabbita  
**Subject:** Permission to include paper in dissertation

Dear Dr. Janakiram,

I am preparing a multi-paper dissertation which will include the paper listed below. I am requesting your permission to include the material just as it appears in the paper.

1. Nadimpalli, V. K., Karthik, G. M., Ram, G. J., and Nagy, P. B. (2018). Monitoring and repair of defects in ultrasonic additive manufacturing. To be submitted to *Journal of Materials Processing Technology*.

Please indicate your approval by replying to this mail, Thank you!

Best Regards,

Venkata Karthik Nadimpalli

---

## Permission to include paper in dissertation

---

manogna karthik Gangaraju <manognakarthik@gmail.com> Wed, May 2, 2018 at 2:00 AM  
To: Karthik Nadimpalli <knadimpalli18@gmail.com>

Yes, I approve. I have no objections.

On Wed 2 May, 2018, 1:40 AM Karthik Nadimpalli, <knadimpalli18@gmail.com> wrote:

Dear Dr. Manogna Karthik,

I am preparing a multi-paper dissertation which will include the paper listed below. I am requesting your permission to include the material just as it appears in the paper.

1. Nadimpalli, V. K., Karthik, G. M., Ram, G. J., and Nagy, P. B. (2018). Monitoring and repair of defects in ultrasonic additive manufacturing. To be submitted to *Journal of Materials Processing Technology*.

Please indicate your approval by replying to this mail, Thank you!

Best Regards,

Venkata Karthik Nadimpalli

---

## Permission to include paper in dissertation

---

**Haijun Gong** <haijun1981@gmail.com>  
To: Karthik Nadimpalli <knadimpalli18@gmail.com>

Tue, May 1, 2018 at 4:29 PM

Karthik,

I, hereby, authorize you to include this paper in your dissertation.

Good luck with your dissertation defense!

Haijun Gong

On Tue, May 1, 2018 at 4:12 PM, Karthik Nadimpalli <knadimpalli18@gmail.com> wrote:

Dear Dr. Haijun Gong,

I am preparing a multi-paper dissertation which will include the paper listed below. I am requesting your permission to include the material just as it appears in the paper.

1. Nadimpalli, V. K., Middendorf, J., Gong, H., Yang, L., and Nagy, P. B. (2018). Ultrasonic nondestructive evaluation as a process parameter development tool for laser powder bed fusion additive manufacturing. To be submitted to *Additive Manufacturing*.

Please indicate your approval by replying to this mail, Thank you!

Best Regards,

Venkata Karthik Nadimpalli

## Re: Permission to include paper in dissertation

John Middendorf <JMiddendorf@utcd Dayton.com>

Wed 5/2/2018 10:36 PM

To: Nadimpalli, Venkata Karthik <karthik.nadimpalli@louisville.edu>;

Karthik,

My sincere apologies on the delayed reply. Yes, include this content in your dissertation.

John

Get [Outlook for Android](#)

From: Nadimpalli, Venkata Karthik  
Sent: Tuesday, May 1, 4:11 PM  
Subject: Permission to include paper in dissertation  
To: John Middendorf

Dear Dr. John Middendorf,

I am preparing a multi-paper dissertation which will include the paper listed below. I am requesting your permission to include the material just as it appears in the paper.

Nadimpalli, V. K., Middendorf, J., Gong, H., Yang, L., and Nagy, P. B. (2018). Ultrasonic nondestructive evaluation as a process parameter development tool for laser powder bed fusion additive manufacturing. To be submitted to *Additive Manufacturing*.

Please indicate your approval by replying to this mail, Thank you!

Best Regards,

Venkata Karthik Nadimpalli



## CURRICULUM VITA

### PERSONAL INFORMATION

Name Venkata Karthik Nadimpalli  
Mail [karthik.nadimpalli@louisville.edu](mailto:karthik.nadimpalli@louisville.edu)  
Phone +1-352-214-5569  
Place of birth Göttingen, Germany  
Nationality Indian

### EDUCATION

University of Cincinnati, Cincinnati, OH, USA – 2014 – 2018  
Visiting Scientist, Department of Aerospace Engineering & Engineering Mechanics

University of Louisville, Louisville, KY, USA – 2011- 2018  
Doctor of Philosophy (Ph.D.) and Master of Science (M.S.) in Industrial Engineering  
Thesis: ‘Ultrasonic Nondestructive Evaluation of e tal Additive a nufacturing’

Indian Institute of Technology Madras, Chennai, TN, India – 2007- 2011  
Bachelor of Technology (B. Tech) in Metallurgical and Materials Engineering  
Thesis: ‘Percolation studies of grain boundary networks in Inconel 718’

### PUBLICATIONS

**Nadimpalli, V. K.**, Yang, L., and Nagy, P. B. (2018). In-situ interfacial quality assessment of ultrasonic additive manufacturing components using ultrasonic NDE. *NDT & E International* **93**, 117-130.

**Nadimpalli, V. K.**, Karthik, G. M., Ram, G. J., and Nagy, P. B. (2018). Monitoring and repair of defects in ultrasonic additive manufacturing. To be submitted to *Journal of Materials Processing Technology*.

**Nadimpalli, V. K.**, Middendorf, J., Gong, H., Yang, L., and Nagy, P. B. (2018). Ultrasonic nondestructive evaluation as a process parameter development tool for laser powder bed fusion additive manufacturing. To be submitted to *Additive Manufacturing*.

- Nadimpalli, V. K.**, and Nagy, P. B., (2018). Designing an in-situ ultrasonic nondestructive evaluation system for ultrasonic additive manufacturing. In *Proceedings of Annual Review of Progress in Qualitative Nondestructive Evaluation* **1949**, 020005, 1-10.
- Nadimpalli, V. K.**, Na, J. K., Bruner, D. T., King, B. A., Yang, L., and Stucker, B. E. (2016). In-situ nondestructive evaluation of ultrasonic additive manufactured components. In *Proceedings of the Solid Freeform Fabrication Symposium* **27**, 1557-1567.
- Karthik, N. V.**, Gu, H., Pal, D., Starr, T., and Stucker, B. E. (2013). High frequency ultrasonic nondestructive evaluation of additively manufactured components. In *Proceedings of the Solid Freeform Fabrication Symposium* **24**, 311-325.
- Rafi, H. K., **Karthik, N. V.**, Gong, H., Starr, T. L., & Stucker, B. E. (2013). Microstructures and mechanical properties of Ti6Al4V parts fabricated by selective laser melting and electron beam melting. *Journal of Materials Engineering and Performance* **22**, 3872-3883.
- Gong, H., Rafi, K., **Karthik, N. V.**, Starr, T., & Stucker, B. (2013). Defect morphology in Ti6Al4V parts fabricated by selective laser melting and electron beam melting. In *Proceedings of the Solid Freeform Fabrication Symposium* **24**, 440-453.
- Rafi, H. K., **Karthik, N. V.**, Starr, T. L., & Stucker, B. E. (2012). Mechanical property evaluation of Ti-6Al-4V parts made using Electron Beam Melting. In *Proceedings of the Solid Freeform Fabrication Symposium* **23**, 526-535.
- Schwabe, M., Rotzoll, R., Küchemann, S., **Nadimpalli, K.**, Vana, P., & Samwer, K. (2010). Relaxation Processes of Poly (tert-butyl acrylate) Chemically Confined via Hydrogen Bonds. *Macromolecular Chemistry and Physics* **211**, 1673-1677.